Henrik Hemmen

Experimental studies of nanostructured clay gels

Master's thesis

Trondheim, May 2008

Norwegian University of Science and Technology
Faculty of Natural Sciences and Technology
Department of Physics

Academic supervisor: Professor Jon Otto Fossum

NTNU
Norwegian University of
Science and Technology

Abstract

Part I

Experimental determination of the roughness of fractures in gels is reported on. The studied gel is prepared by dispersing the synthetic clay Laponite in de-ionized water. A novel way of finding the roughness exponent through the use of Magnetic Resonance Imaging is developed. By recording the ^{1}H signal from slices of the clay gel, an extraction of the clay–air interface is possible. From the one-dimensional height profiles obtained in this manner, the roughness exponent is calculated using standard methods found in the literature.

We create fracture surfaces by a controlled removal of filter paper attached to the surface of the gel. By studying fracture surfaces created with Mode-I fracturing, the roughness exponent is found to be $0.56\ (+0.05, -0.07)$, and no dependency between fracturing speed and roughness is discovered. On the other hand, using a combination of Mode-I and Mode-II fracturing, a velocity-dependent roughness in the direction perpendicular to the fracturing is revealed. A connection with the shear thinning behaviour of Laponite gels is proposed, to account for this behaviour. Finally, an attempt to test the experimental method is made. By measuring upon a sample with predetermined roughness, we seek independent confirmations of the accuracy of our method. Due to a bad choice of test sample, this test has not yet been conclusive.

Part II

A wide angle synchrotron X-ray scattering study of the synthetic clay sodium fluorohectorite (NaFh) dispersed in saline water is presented. With the sample contained in a 2 mm diameter glass capillary, we observe three distinct phases – sediment, nematic, isotropic – in agreement with previous studies of the same system. The orientational order in the nematic phase, calculated from the anisotropic X-ray scattering, is found to be remarkably uniform. An arithmetic mean of the calculations results in 0.66 ± 0.03 as the value of the nematic order parameter.

In addition to the three phases already mentioned, a transition layer in the interface between the nematic phase and the sediment is discovered. In this layer, the mean preferred orientation of the NaFh particle directors is close to the vertical, indicating a true uniaxial nematic phase where the clay platelets are lying face-down. Although previously observed, both by visual observations of birefringence and in diffusion MRI studies, this is the first time this phenomenon has been properly treated for NaFh solutions. A radial transition from horizontal to vertical to horizontal is proposed, to account for the mean orientation of the particle directors $26°$ off the vertical.

Contents

Preface

This thesis is the final work of the Master's degree in Physics at the Norwegian University of Science and Technology (NTNU). During the last two years, working on the thesis has taken me to several places around the world. While most of the time has been spent at the Complex Systems and Soft Materials Group (Complex) at NTNU, almost six months were spent at the Federal University of Pernambuco (UFPE) in Recife, Brazil. All the MRI work and large part of the writing was done there. I stayed nearly a week in Grenoble, France, in March 2007, where a synchrotron experiment was carried out at the European Synchrotron Radiation Facility (ESRF), and in February 2008, I spent one week at the University of Rennes 1, France, learning a new way to analyze Wide Angle X-ray Scattering (WAXS) data.

While working on my Master's thesis, I have had the privilege to learn about and (more importantly) use, tools as diverse as NMR, MRI, AFM, Synchrotron X-ray and Complex' own in-house SAXS/WAXS-machine. The learning curve has been steep, but the educational and personal outcome has been correspondingly great.

The motivation for the thesis was to study nano-layered clay gels using several experimental techniques. At the Laboratory for Soft and Complex Matter Studies, my supervisor, Professor Jon Otto Fossum, has been studying clays and clay suspensions for years. In addition to the goal of understanding these systems per se, clays can act as model systems for the understanding of basic physical properties and processes in soft and complex matter, from the nano scale to the human and geological scale. When trying to extract universality from complex systems, one of the main obstacles is finding the right level of description. This is illustrated by the figure on the cover: The fracture surface on top of a clay and water gel is indeed complex, but by removing redundant information, we can describe the surface's roughness by a single variable, ζ.

Characterizing roughness is the focus of the first part of this thesis, where a series of MRI experiments performed in Recife are presented. This work was done in collaboration with Professor Mario Engelsberg and his PhD-student Eduardo Azevedo. Professor Engelsberg and Professor Fossum have been collaborating for

some years now, and my going to Brazil was a natural part of this collaboration.

In Part II, an experiment done at the ESRF is presented. Synchrotron sources are used as an integral part of Complex, particularly the ESRF (France), LNLS (Brazil) and PAL (Korea). In this experiment we investigated the orientational ordering of synthetic clay particles dispersed in saline water. Although the experiment was already applied for at ESRF before I started my Master's degree, I prepared the samples, transported them to Grenoble, took part in the experiment, and did the analysis, so I can honestly say I feel the experiment is mine.

The results of the ESRF experiment, combined with results obtained using other experimental techniques, have already been compiled into a paper intended for submission to Langmuir. Although not yet completely finished, the draft of this article is included in the appendices. There, one can also find the MATLAB script used to extract the surface profile shown on the cover, as well as analyzed results from an experiment similar to the one presented in Part II.

Henrik Hemmen Trondheim, May 15, 2008

Acknowledgements

I would first and foremost like to thank my supervisor Professor Jon Otto Fossum, for giving me the opportunity to explore two worlds, both the exotic and strange nanoworld, and the equally exotic, but perhaps not quite so strange, earth. His academical advice and support, as well as the practical help and company in Brazil, has been invaluable. I am also greatly indebted to Professor Mario Engelsberg for welcoming me to Recife and for all his advice, assistance and comments. Without the help and care of Professor Engelsberg and his wife Theresa, I would have been lost. Thanks also to Professor Yves Méheust for inviting me to Rennes, and for his later comments on my work.

The friendship and company of Eduardo Azevedo and Rômulo Tenório deserve a thousand *obrigados*, and I am particularly grateful to Eduardo for teaching me MRI, cooperating with me, letting me share his lab, and for his lasting patience with my awkward Portuguese. I would also like to thank Lars Ramstad Alme for coping with my interference during the first year of my work, Daví de Miranda Fonsêca for sharing his data, Professor Jean Schmittbuhl for lending us his sample, Professor Ricardo Emmanuel de Souza and Knut Magnus for suggestions, Nils Ivar Ringdal and Elisabeth Lindbo Hansen for cooperation on writing the Langmuir paper and Truls Lange for help on formatting. A huge brotherly thankyou goes to Peter Hemmen for proofreading.

The technical assistance from Ole Tore Buset and the help of the engineering workshop at NTNU must be acknowledged, and finally I am grateful to my fellow students for their company and suggestions.

Part I

An MRI study of roughness in Laponite gel fractures

Chapter 1

Theory

1.1 Clays

Short introduction

Clays are fascinating materials that are readily available and present almost everywhere on earth. In fact, if you gathered all the clay on our planet and spread it evenly around the surface, you would create a layer almost a mile in thickness [1]. Even without other knowledge about clays than having played with it as a child, it is obvious that clays have some amazing properties. Wet clay is soft and easily shaped by hand, but retains the form you give it if it is left alone. If clay is heated, or *baked*, it becomes hard as rock, showing completely other properties than it did before. This hardening has been utilized for most of man's existence, when clays have been used to produce building materials and pottery. Other more modern fields where clays play an important role include paper filling, oil well drilling, and rheology modifications [2]. The huge external surface area of clays (as compared with their volume), also makes them first-class materials for catalysis, retention of toxic substances and future supports for composites [3]. In fact, some claim that "clays and clay minerals, either as such or after modification, will be recognized as the materials of the 21st century because they are abundant, inexpensive and environmentally friendly." [4].

Although clays have been studied for centuries by geologists, geo-chemists and others, the fundamental studies of complex physical phenomena in clays is a relatively new field [5]. The reason for the emerging interest in clays by physicists in particular, is the increasing availability of clean chemistry-customized, synthetic clays. This has led clays to be included in modern material science, together with other complex adaptive materials such as colloids, polymers, liquid crystals, bio materials, etc. [5].

1.1.1 The structure of clays

Clays are classified among the phyllosilicates, which again are part of the silicate mineral class. The exact definition of clays has been a subject under discussion for many years, see e.g. [6] from which we quote this definition:

> The term "clay" refers to a naturally occurring material composed primarily of fine-grained minerals, which is generally plastic at appropriate water contents and will harden with [*sic*] dried or fired. Although clay usually contains phyllosilicates, it may contain other materials that impart plasticity and harden when dried or fired. Associated phases in clay may include materials that do not impart plasticity and organic matter.

Other, simpler definitions, include “Clays are naturally occurring materials formed by the weathering and decomposition of igneous rocks” [7] and “Clays are materials based on a two-dimensional stack of inorganic layers.” [8]. In the context of this thesis, the last definition is the most relevant, and the layered structure of clay minerals will be examined further below.

Octahedral and tetrahedral sheets

The individual layers of a clay are made up of two types of elemental *sheets* which are either *tetrahedral* or *octahedral*. The sheets are two-dimensional lattices which together constitute a layer. The tetrahedral sheets are usually SiO_4^{4-} or AlO_4^{5-} tetrahedra linked together by sharing three of four vertices, illustrated in Figure 1.1. The oxygen atoms at the vertices not shared with the neigbouring tetrahedra are called apical oxygens [3], and all the apical oxygen point in the same direction. By knowing the effective ionic radii of Si, Al and O in phyllosilicates the height of the tetrahedron, h_t, and the lattice parameters, a and b, are easily calculated.

The octahedral sheet consists of octahedra sharing all their six vertices. The octahedra are laid on triangular faces, and six octahedra together make up one unit cell, illustrated in Figure 1.2. The octahedra can be divided into two sub-groups, trioctahedral and dioctahedral. In the trioctahedral type, all the central octahedral sites are filled, whereas only two of the sites are filled in the dioctahedral case [9]. The lattice formed by the octahedra is hexagonal symmetric. The height and sides of the octahedra, and the lattice parameters a and b, depend on the chemical structure, but can easily be approximated by knowing the ionic radii of the atoms.

Layers

A clay is typically characterized by how its tetrahedral and octahedral sheets combine together to make layers. We denote one tetrahedral sheet bonded to one octa-

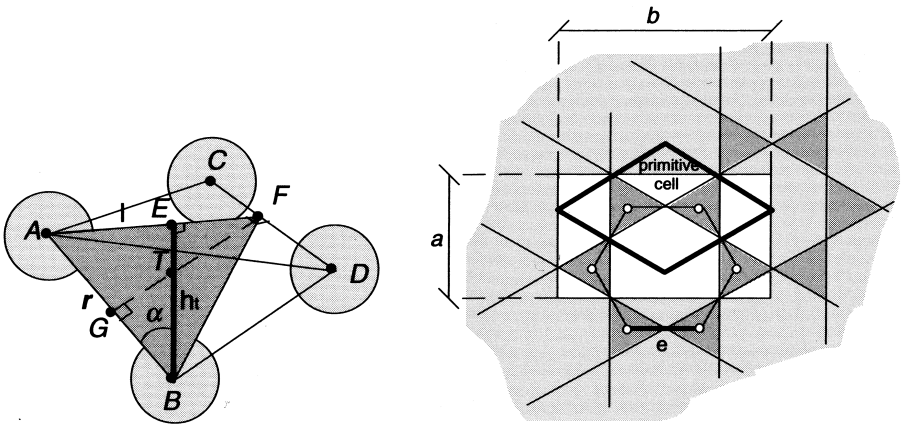

(a) (b)

FIGURE 1.1: The structure of the tetrahedral sheet. **a)** Illustration of a tetrahedron, with O at sites A to D and a cation, usually Si or Al, at site T. **b)** Illustration of the lattice. The white rectangle is the unit cell, the black diamond is the primitive unit cell, and the hexagonal Bravais lattice is shown centred on the hexagonal cavity. Adapted from [3].

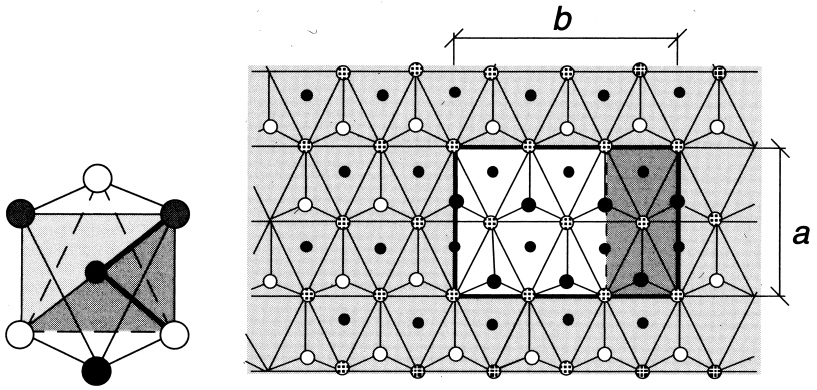

(a) (b)

FIGURE 1.2: The structure of the octahedral sheet. **a)** An individual octahedron, laid on a triangular face. **b)** Illustration of the lattice. The black rectangle is the unit cell, consisting of six octahedra. Adapted from [3].

hedral sheet as a *1:1 layer*, and when one octahedral sheet is bonded between two tetrahedral sheets we call it a *2:1 layer*. The two different layer-types are shown in Figure 1.3. In a 1:1 structure, two of the vertices of an octahedron are formed by the apical oxygens of the neighbouring tetrahedra. In a 2:1 structure, this number is four, as the octahedral sheet is sandwiched between two sheets of tetrahedra. The octahedral oxygens not shared with the tetrahedra are terminated by a proton and form hydroxyl groups. Because the lattice parameters a and b of the tetrahedral and octahedral sheets are different, this type of bonding cannot take place without deforming the structure of the individual sheets. The extent of this deformation depends on the type of octahedral sheet [3].

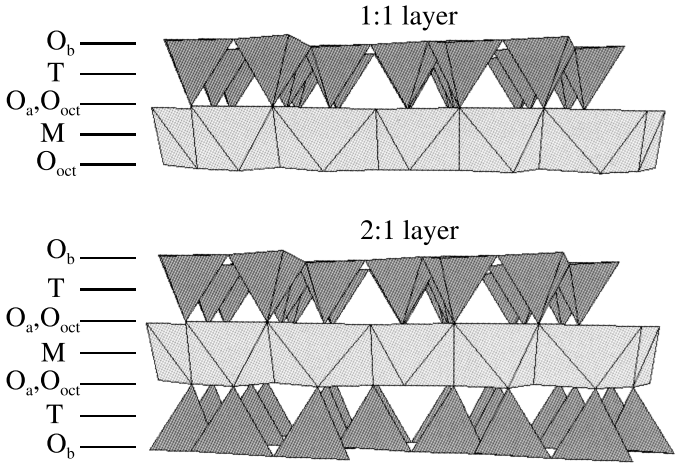

FIGURE 1.3: The figure shows a 1:1 layer (top) and a 2:1 layer (bottom). M and T are respectively the octahedral and tetrahedral cations. O_a, O_b and O_{oct} are positions known as the tetrahedral apical, tetrahedral basal, and the octahedral anionic positions. Adapted from [10].

Intercalation between layers

In 2:1 layered clays, guest substances may be in inserted into the space between the layers in such a way that the layered clay structure itself remain essentially undistorted. This is called intercalation, and clays that allow intercalation are called intercalation compounds. The intercalation property is in itself typical for the class of layered solids, but the number of substances that can be inserted in clays greatly exceed that of other intercalation compounds [9]. In some 2:1 phyllosilicates, the intercalation is occurring to ensure the electrical neutrality of the crystal structure. Non-equivalent substitutions of central atoms in the layers generate a negative surface charge on the layer surface [11]. This *layer charge* is balanced by hydrated exchangeable cations, e.g. Ca^{2+}, Na^{+} or Mg^{2+}. The cations are housed in the hexag-

onal cavities of the opposing tetrahedral sheets (Figure 1.1), and form an additional interlayer sheet [3]. An illustration of a 2:1 layered clay with intercalation compounds is shown in Figure 1.4. The negative layer charge is recognized as one of the most important characteristics of 2:1 layered clays, and controls the minerals ability to absorb polar molecules in the interlayer space, i.e. the ability to *swell*. Swelling clays are called *smectites* [2].

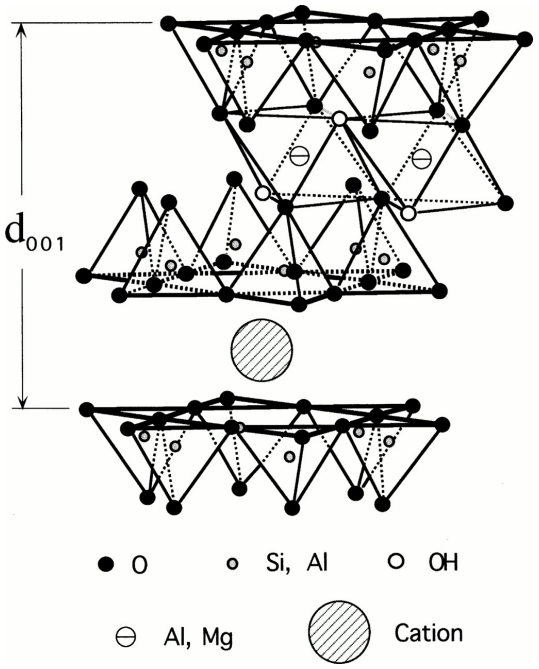

FIGURE 1.4: Typical structure of a 2:1 layered silicate clay. The length d_{001} includes the 2:1 layer and the interlayer sheet and is the smallest c-axis repeat distance. As noted in the text, the cation sits in the hexagonal cavity of the opposing tetrahedral sheets. Taken from from [9].

The last decade has seen much research on the intercalation of water in synthetic clays, see e.g. [12–14], and the preferred experimental techniques used to study this phenomenon is X-ray diffraction, neutron diffraction and NMR [15]. Whether a clay swells or not depend on the layer charge of the clay and the properties of the substance entering the interlayer space. Water enter the swelling clay in monolayers of water, and the number of layers present in a sample is dependent on both temperature and relative humidity.

Colloids

The property of swelling discussed above, in which layers of water reversibly may enter and exit the interlayer space, refers to dehydrated or only weakly hydrated

clays, i.e. dry samples. When clay particles are completely dispersed in another media, they are no longer referred to as intercalation compounds, but instead as colloid particles. A colloid is a mixture between two separate phases, a dispersed phase – in this case clay – and a continuous phase which might be water, oil, paraffin, etc. Many of the things we encounter on a daily basis are colloids – e.g. milk, butter, paint or fog – and colloid science is highly interdisciplinary, in that it interests both physicists, chemists, biologists and others. A colloid particle is defined as a particle that has some linear dimension between 1 nm and 1000 nm [16].

1.1.2 Laponite

Laponite is an entirely synthetic 2:1 layered swelling clay consisting of disk-like platelets with approximate thickness 1 nm and an average diameter close to 200 Å [17]. Laponite belongs to the smectite family of layered silicates. Smectite is the most intensely studied family of clays, due to its wide range of chemical compositions, intercalation properties, and the ability to swell and undergo pillaring [18]. The intense investigation of Laponite has resulted in commercial applications in a wide range of fields, including surface coatings and personal care products – the separation of colored stripes in toothpaste being the most famous example – as well as agricultural and oilfield applications. For the work presented in this thesis we have used *Laponite RD* purchased from Rockwood Additives Ltd, but will refer to it in the text only as Laponite.

The chemical formula of Laponite is

$$Na^{+0.7}[(Si_8Mg_{5.5}Li_{0.3})O_{20}(OH)_4]^{-0.7} \quad \text{per unit cell,} \tag{1.1}$$

and the individual Laponite disks are made up by repetition of the unit cell in the two lateral directions [19]. The bracketed term in the chemical formula has a negative charge of –0.7 e, which is the negative layer charge of the 2:1 structure. This is neutralized by ions of Na^+, that during manufacturing migrate into the interlayer region and form intercalation cations.

Laponite in water

Laponite shows a whole range of interesting properties when dissolved in water. Even at concentrations below 2 %, it undergoes a puzzling liquid–solid transition, forming a clear, transparent gel [20]. The exact mechanism for this behaviour is complex, but an illustration can be seen in Figure 1.5. As a dry, free flowing powder, Laponite particles stick together as large particle aggregates. The aggregates consist of stacks of Laponite disks, forming cylinders of disk shaped particles. When dissolved in water, H_2O molecules enter the interlayer space to hydrate the

sodium ions. This breaks the particle-stacks apart, resulting in separated Laponite disks, or separated groups of disks. Because the Laponite disks have a charge distribution, with negatively charged faces and positively charged edges, the individual particles interact, forming three-dimensional networks [21].

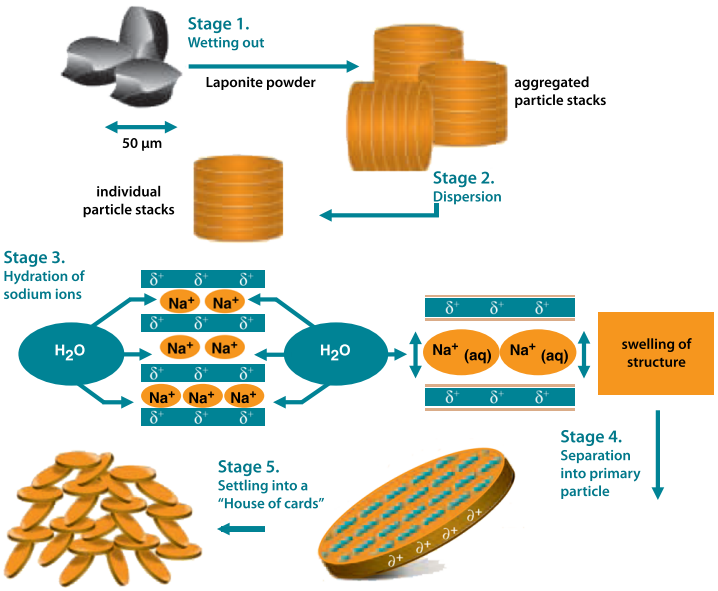

FIGURE 1.5: Schematic illustration of what happens when Laponite is dissolved in water. Adapted from from [19].

Generally, there are two different mechanisms used to explain the gelation of Laponite and clay minerals in general [22]. The first case, which is relevant to high concentrations of salt ($> 10^{-3}$ M), is the "house of cards" structure illustrated in Stage 5 of Figure 1.5. In water with high ionic strength, the salt compresses the long-range electrostatic repulsion between the platelets, allowing both face-to-face and edge-to-face associations. Together with the attractive van der Waals forces between the particles, this leads to closely linked three-dimensional networks. In addition to being illustrative, the "house of cards" structure is theoretically supported e.g. in Dijkstra et al. [23], although the structure is still debated, some say refuted [24]. When the electrolyte concentration is lower, the platelets are not allowed to associate, and the equilibrium structure is instead caused by the long-range repulsion of the interactive double-layers. It is worth noting that the two explanations are quite opposite, as the first deals with *attraction*, the second with *repulsion*. For a more thorough discussion of the above, using DLVO theory to explain the interaction between the charged colloid particles and the screening electrolytes, see e.g. Israelachvili [25].

Phase diagram of Laponite–water–salt dispersions

Even though the exact structure of the three-dimensional Laponite network in water is not yet fully understood, the Laponite–water–salt phase diagram is well known, see Figure 1.6. The viscosity of the Laponite–water solution is dependent on both the concentration of Laponite and the presence of salt, and it is possible to characterize four distinct phases, *Isotropic liquid*, *Isotropic gel*, *Nematic gel* and *Flocculation*. A short description of the phases, largely taken from Fossum [15], is given below.

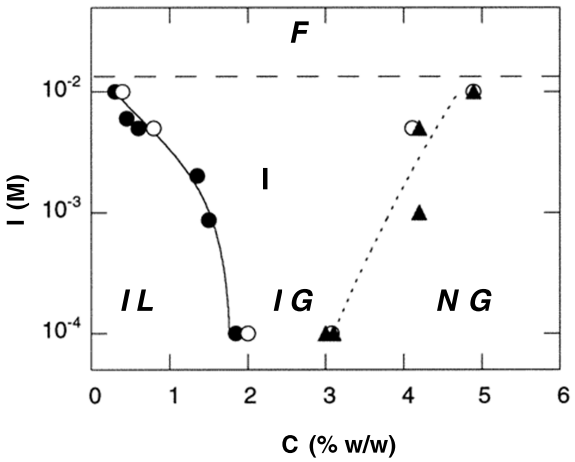

FIGURE 1.6: The phase diagram of Laponite dissolved in water. The first axis is the concentration of Laponite, the second is the NaCl consentration. F, IL, IG and NG are the phases of flocculation, isotropic liquid, isotropic gel, and nematic gel, respectively. Adapted from [17].

In the isotropic liquid phase, the colloid particles consist of several platelets of Laponite stacked together, the compactness and number of platelets depending on the concentration of salt. As the aggregates are generally to small to scatter visible light, the isotropic liquid is transparent. Approaching the transition to isotropic gel, either by adding more clay or reducing the electrolyte concentration, the viscosity of the liquid increases. An interesting property of this phase is that it may be made birefringent by applying high electric fields [26].

The isotropic gel is very fascinating both to look at and to touch, as it is highly viscous and still transparent at clay concentrations as low as 2 %. It both "looks and feels like stiff water" [15]. At higher concentrations of electrolytes, i.e. approaching the flocculation phase, the aggregates become micrometer sized, thus scattering visible light, and the gel is no longer transparent. After the first settling of the gel, an extremely slow aggregation dynamic lasting up to 1 year is observed.

The nematic gel is characterized by macroscopic nematic ordering of the

platelets. Nematic ordering means parallel orientation of the platelets, without long-range positional order, see Figure 1.7 for an illustration. The reason for this ordering is that it becomes favourable for the anisotropic clay platelets to align as the system is made denser, thus giving up orientational entropy in exchange for much greater positional entropy [27]. The nematic ordering of clay suspensions may be studied e.g. by observing the birefringence of light shone through the clay, see Ringdal [28] for a study of this kind done on NaFh.

In the flocculation phase, the salt concentration is so high that the aggregates sediment, resulting in a clay–water "phase separation".

(a) Isotropic (b) Nematic (c) Smectic

FIGURE 1.7: Schematic illustration of isotropic, nematic and smectic ordering. Adapted from [29].

1.1.3 Sodium fluorohectorite

Hectorite

The synthetic clay *sodium fluorohectorite* (NaFh) is a member of the *hectorite* family of clays. Hectorites get their name from the geographic area where they can be found in nature: Hector, California. Hectorite – like Laponite a 2:1-layered clay – is composed of a layer of octahedra, sandwiched between two layers of silicon tetrahedra. The octahedron layer consist of hydroxyls, magnesium and lithium ions, whereas the tetrahedron layers are SiO_4. The entire composition of hectorite is

$$M_x - (Mg_{3-x}Li_x)Si_4O_{10}(OH)_2 \quad \text{per half unit cell,} \tag{1.2}$$

where x is the proportion of Li-ions per half unit cell, and M refers to a generic monovalent interlayer cation [10].

Sodium fluorohectorite

What separates NaFh from regular hectorite is that the hydroxyl groups have been substituted with fluorine ions (F^-). The interlayer cation is, as the name implies,

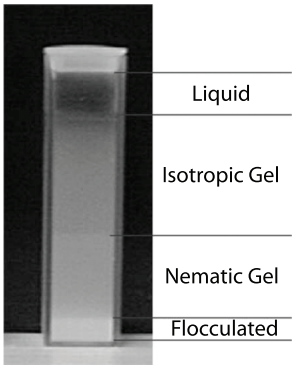

FIGURE 1.8: A sample of a NaFh–water–salt solution with four easily identifiable phases, separated by gravity. The sample consisted of 3 w/w % NaFh, 4.5×10^{-3} M NaCl, and deionized water. Adapted from [34].

sodium (Na), which results in the total chemical formula:

$$\mathrm{Na}_x - (\mathrm{Mg}_{3-x}\mathrm{Li}_x)\mathrm{Si}_4\mathrm{O}_{10}\mathrm{F}_2 \quad \text{per half unit cell.} \tag{1.3}$$

Like natural hectorite, NaFh is a swelling clay that have the ability to intercalate a variable amount of water in the interlayer space, resulting in a changed lattice constant along the stacking direction [30]. The intercalation of water molecules into the interlayer space between the clay platelets is governed by temperature and the vapor partial pressure in the surrounding pore-space atmosphere [31]. Three stable hydration states exist, consisting of zero, one or two intercalated monolayers of water between the silicate platelets, respectively denoted 0WL, 1WL or 2WL. The basal spacings of the nano-sandwiches are 1.0, 1.2 or 1.5 nm for these three intercalation states [12].

NaFh represents an extreme in particle size and layer charge within the smectite group. It has a particle size of up to 20 000 Å with a layer charge of $1.2\,\mathrm{e}^-$ per unit cell [18]. The large layer charge originates from the substitution of Li^+ for Mg^{2+} in the octahedral layer.

Sodium fluorohectorite suspensions in water

NaFh has a polydispersity in particle size that makes suspensions of it particularly interesting. In a suspension in water, gravitational forces effectively sort the particles by size, stabilizing in some cases several strata of gels, sols and/or sediments within a single sample tube [30], see Figure 1.8. Because of the large surface charge, the platelets remain stacked in water suspension, even in low saline environment, as opposed to e.g. Laponite and Montmorillonite [32, 33].

1.2 Nuclear Magnetic Resonance

Short introduction

The history of Nuclear Magnetic Resonance (NMR) can be said to begin in the 1920s, with the development of the concept of spin as a quantum mechanical entity [35]. While the quantum theory could explain a number of phenomena that had eluded classical mechanics, experimental confirmation of quantum phenomena was in high demand. The quest to accurately measure spins and the associated magnetic moment eventually led to the discovery of the magnetic resonance. The first account of this is in the 1938 publication by Rabi et al. [36], where resonance in a molecular beam of LiCl was observed. Rabi was later awarded the Nobel Prize in 1944 "for his resonance method for recording the magnetic properties of atomic nuclei," [35]. The Second World War put most of the basic scientific research on hold, but the wartime work on radar development of such important figures in NMR as Felix Block and Edward Purcell had an extremely positive impact on the speed of NMR development after the war [35]. The first observation of NMR in a bulk material was in 1945, by Purcell et al. [37], a feat which earned Purcell a shared Nobel Prize in 1952, together with Bloch, who did a similar experiment a few weeks later.

Though early NMR equipment was useful for measuring magnetic moments, no one expected the rapid exponential expansion of its uses. The commercialization of the technology by Varian, introduction of more powerful magnets (eventually superconducting), development of pulse and spin echo methods, discovery of the Overhauser effect, and the development of Fourier transform- and 2D-NMR are just some keywords that describe the development over the last fifty years. A more thorough recollection of the history can be found in Becker et al.'s introductory article to the Encyclopedia of Nuclear Magnetic Resonance [35].

The field of Nuclear Magnetic Resonance is large, and NMR finds scientific uses in fields as diverse as physics, chemistry, biology among others. Furthermore, the closely interlinked technique of Magnetic Resonance Imaging (MRI) has also become a powerful experimental technique, as well as one of the most important tools for nonevasive medical imaging. In this section we will examine the basic theory of NMR, which will serve as a basis for the section on MRI. The section is largely based on information gathered from the books by C.P. Slichter [38], Zhi-Pei Liang and Paul C. Lauterbur [39], P. C. Hemmer [40], and E. Mark Haacke et al. [41]. Many of the elements of magnetic resonance can be explained both by classical and quantum physics. Even though one might argue that the quantum viewpoint is more precise, we will use classical physics where this gives more clarity.

1.2.1 Angular momentum and magnetism

Resonance is a term that is used when something is in tune with the natural frequency of a system, and *magnetic resonance* is found in magnetic systems that possess both magnetic moments and angular momentum. In this case the natural frequency of the system is the frequency with which the magnetic moments precess in an external magnetic field. Because this frequency typically falls in the radio frequency region, the term *radio frequency spectroscopy* is often used instead of NMR spectroscopy [38].

The two elementary particles that compose atomic nuclei, protons and neutrons, both have the intrinsic quantum mechanical property of *spin*. In classical mechanics, the spin is associated with a rotation of a body around its centre of mass, though in the context of elementary particles, the spin cannot be associated with a rotation. It is instead a truly intrinsic property, along with mass, electrical charge, etc. A nucleus might consist of many particles coupled together, so that it possesses a total angular momentum $\boldsymbol{J}$. Depending on the number of spins in the nucleus, it might also possess a total magnetic momentum $\boldsymbol{\mu}$. The angular and magnetic momentum vectors are in fact parallel, so that the relationship between a non-zero angular momentum and a non-zero magnetic moment is given by

$$\boldsymbol{\mu} = \gamma \boldsymbol{J} \ , \tag{1.4}$$

where γ is a nucleus-dependent constant called the *gyromagnetic ratio*. To simplify matters, γ is assumed to be positive in the discussion below, although this is not always the case. Most elements of the periodic table contain a stable isotope with a non-zero magnetic moment, even though the natural abundance of many of these may be small [42]. Of the magnetic isotopes, ^{1}H is by far the most important for NMR studies.

The total angular momentum of a nucleus has the quantum mechanical property of being quantized. However, for stable (non-radioactive) nuclei, only the angular momentum of the nuclear ground state needs to be considered. Hence, for usual NMR experiments J can be considered as a fixed constant parameter, characteristic of the ground state of each nucleus. The magnitude J of the angular momentum can be related to the angular momentum quantum number I by

$$J = \hbar \sqrt{I(I+1)} \ , \tag{1.5}$$

and the component of the angular momentum along a given direction (ex. z) is given by

$$J_z = m\hbar \ , \quad m = (-I), (-I+1), (-I+2), \ldots (I-2), (I-1), I \ . \tag{1.6}$$

Since J includes orbital as well as spin angular momentum of all the nucleons, I can only assume integer or half-integer values, e.g. ^{1}H (I=1/2), ^{19}F (I=1/2), ^{31}P (I=1/2), ^{2}H (I=1), ^{23}Na (I=3/2), ^{12}C (I=0), ^{13}C (I=1/2), etc.

Equation (1.5) can be found by calculating the eigenvalues of $\boldsymbol{I}$, which is related to the angular momentum by

$$\boldsymbol{J} = \hbar \boldsymbol{I} \,, \tag{1.7}$$

where $\hbar$ is the well known reduced Planck constant. The operator $\boldsymbol{I}^2$ commutes with any component of $\boldsymbol{I}$, meaning that the eigenstates of $\boldsymbol{I}^2$ and one of the components of $\boldsymbol{I}$, e.g. I_z, may be measured simultaneously. If we let Ψ represent the quantum state of the nucleus, this leads to the following equations

$$\boldsymbol{I}^2 \left|\Psi\right\rangle = I(I+1) \left|\Psi\right\rangle \tag{1.8}$$

$$I_z \left|\Psi\right\rangle = m \left|\Psi\right\rangle \,, \tag{1.9}$$

where $I(I+1)$ and m are the eigenvalues of $\boldsymbol{I}^2$ and I_z respectively. By combining Equations (1.7) and (1.8) we arrive at Equation (1.5).

As noted above, $\boldsymbol{I}^2$ commutes with any element of $\boldsymbol{I}$. It does not, however, commute with more than one element at the time. This fact is rooted in Heisenberg's uncertainty principle and leads to a phenomenon called *directional quantization*. At any given time, we might only know $|\boldsymbol{I}|$ and one of the elements of $\boldsymbol{I}$, generally chosen to be I_z. This is illustrated in Figure 1.9.

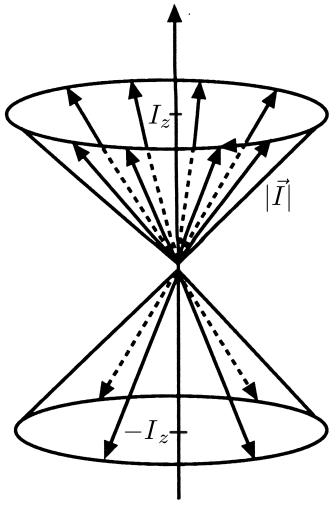

FIGURE 1.9: If we know the value of I_z, and the length of $\boldsymbol{I}$, the values of I_x and I_y are unknown, meaning that $\boldsymbol{I}$ lies on the cone shown in the figure. Adapted from [39].

If we introduce a magnetic field along the z-axis, $\boldsymbol{B} = B_0\hat{\boldsymbol{z}}$, parallel to I_z, the effect on the magnetic moment is a clockwise precessional movement around the z-axis, given by

$$\frac{\mathrm{d}\boldsymbol{\mu}}{\mathrm{d}t} = \gamma\boldsymbol{\mu} \times \boldsymbol{B} \,. \tag{1.10}$$

The precession is obvious from the cross product; $\mathrm{d}\boldsymbol{\mu}/\mathrm{d}t$ is perpendicular to both $\boldsymbol{\mu}$ and $\boldsymbol{B}$. The angular frequency of this precession is called the *Larmor frequency*, a quantity that is very important in magnetic resonance. The value of the Larmor frequency is $\omega = \gamma B_0$, a fact we will prove both quantum mechanically and classically, the latter by introducing a rotating frame of reference.

We start with the quantum mechanical approach, by introducing

$$\mathcal{H} = -\boldsymbol{\mu} \cdot \boldsymbol{B} \,, \tag{1.11}$$

the Hamiltonian of the interaction energy between $\boldsymbol{B}$ and the nucleus. By taking $\boldsymbol{B}$ along the z-axis, and substituting for $\boldsymbol{\mu}$, we find

$$\mathcal{H} = -\gamma\hbar B_0 I_z \,. \tag{1.12}$$

As we already know the eigenvalues of I_z from Equation (1.9), this allows us to calculate the allowed energies of the system:

$$E = -\gamma\hbar B_0 m_z \,. \tag{1.13}$$

For nuclei with spin $I = 1/2$, such as ^{1}H, this allows for only two energy states. The state with the lowest energy is $m_z = +1/2$, and this state is denoted $E_\uparrow$. The other state, with $m_z = -1/2$, we denote $E_\downarrow$. These states correspond respectively to μ_z being either aligned or anti-aligned with $\boldsymbol{B}$.

The difference between energy levels might be expressed by

$$\hbar\omega = \Delta E \,, \tag{1.14}$$

where ΔE is the energy difference, and ω is an angular frequency. By using the raising and lowering operators I^+ and I^-, it is easily shown that only transitions between levels adjacent in energy are allowed [40]. This is of course trivial for hydrogen since it has only two levels, but spins higher than $I = 1/2$ means more energy levels, $I = 3/2$ for instance, gives four. When only adjacent energy transitions is allowed we get ΔE from Equation (1.13),

$$\hbar\omega = \gamma\hbar B_0 \,, \tag{1.15}$$

which upon canceling $\hbar$ results in the Larmor frequency:

$$\omega = \gamma B_0 \,. \tag{1.16}$$

1.2.2 Rotating frame

When discussing nuclear magnetic resonance it is useful to introduce a new coordinate system (x', y', z') called the *rotating frame*, in addition to the familiar fixed coordinate system (x, y, z), from now on called *laboratory frame*. The relationship between the two coordinate systems is that the x' and y'-axes of the rotating frame rotates around the z-axis with an angular velocity $\boldsymbol{\omega}$. The two z-axes, z and z', will be used a bit haphazardly, but this should not lead to any confusion, as they are in fact identical. At first glance the rotating frame does not seem to simplify matters, but at soon as we introduce time dependent fields, it will.

Before we continue, a comment about the magnetic moment, $\boldsymbol{\mu}$, must be made. Given a group of nuclei, each with magnetic individual magnetic moments $\boldsymbol{\mu}_k$, their total magnetic moment, $\boldsymbol{\mu}$, is defined as

$$\boldsymbol{\mu} = \sum_k \boldsymbol{\mu}_k \,. \tag{1.17}$$

This means that even though the magnetic moment of e.g. a single proton cannot be parallel to an applied field $\boldsymbol{B}$ (Figure 1.9), the sum of all the moments in a macroscopic sample can. As long as the individual moments do not interact with each other, the equation of motion for one individual moment, Equation (1.10), also holds true for the total moment. In the following discussion, $\boldsymbol{\mu}$ will refer to the total magnetic moment.

Precession in a static field

Our first use of the rotating frame will be to consider the behaviour of the magnetic moment in a static field along the z-axis. In order to do this, we need to know the time derivative of $\boldsymbol{\mu}$ in the rotating frame. We express $\boldsymbol{\mu}$ in the rotating frame as

$$\boldsymbol{\mu}_r = \hat{\boldsymbol{x}}'\mu_{x'} + \hat{\boldsymbol{y}}'\mu_{y'} + \hat{\boldsymbol{z}}'\mu_{z'} \,. \tag{1.18}$$

The unit vectors $\hat{\boldsymbol{x}}'$, $\hat{\boldsymbol{y}}'$ and $\hat{\boldsymbol{z}}'$ of the rotating frame change with time. This is contrary to the regular unit vectors $\hat{\boldsymbol{x}}$, $\hat{\boldsymbol{y}}$ and $\hat{\boldsymbol{z}}$, which are constants. When taking the time derivative of $\boldsymbol{\mu}_r$, we must therefore also differentiate the unit vectors

$$\frac{\mathrm{d}\hat{\boldsymbol{x}}'}{\mathrm{d}t} = \boldsymbol{\omega} \times \hat{\boldsymbol{x}}' \,, \tag{1.19}$$

where we use the fact that the rotating frame rotates with angular velocity $\boldsymbol{\omega}$. The same relation holds if we substitute $\hat{\boldsymbol{y}}'$ or $\hat{\boldsymbol{z}}'$ for $\hat{\boldsymbol{x}}'$. Using Equation (1.19) the time derivative of $\boldsymbol{\mu}_r$ is therefore

$$\begin{aligned}\frac{\mathrm{d}\boldsymbol{\mu}_r}{\mathrm{d}t} &= \hat{\boldsymbol{x}}'\frac{\mathrm{d}\mu_{x'}}{\mathrm{d}t} + \mu_{x'}\frac{\mathrm{d}\hat{\boldsymbol{x}}'}{\mathrm{d}t} + \hat{\boldsymbol{y}}'\frac{\mathrm{d}\mu_{y'}}{\mathrm{d}t} + \mu_{y'}\frac{\mathrm{d}\hat{\boldsymbol{y}}'}{\mathrm{d}t} + \hat{\boldsymbol{z}}'\frac{\mathrm{d}\mu_{z'}}{\mathrm{d}t} + \mu_{z'}\frac{\mathrm{d}\hat{\boldsymbol{z}}'}{\mathrm{d}t} \\ &= \hat{\boldsymbol{x}}'\frac{\mathrm{d}\mu_{x'}}{\mathrm{d}t} + \hat{\boldsymbol{y}}'\frac{\mathrm{d}\mu_{y'}}{\mathrm{d}t} + \hat{\boldsymbol{z}}'\frac{\mathrm{d}\mu_{z'}}{\mathrm{d}t} + \boldsymbol{\omega} \times (\hat{\boldsymbol{x}}'\mu_{x'} + \hat{\boldsymbol{y}}'\mu_{y'} + \hat{\boldsymbol{z}}'\mu_{z'}) \\ &= \frac{\delta\boldsymbol{\mu}_r}{\delta t} + \boldsymbol{\omega} \times \boldsymbol{\mu}_r\,,\end{aligned} \tag{1.20}$$

where $\delta\boldsymbol{\mu}_r/\delta t$ represents the time derivative of $\boldsymbol{\mu}_r$ with respect to the rotating frame (x', y', z').

By combining Equations (1.10) and (1.20) we get the equation of motion of $\boldsymbol{\mu}$ in the rotating frame

$$\frac{\delta\boldsymbol{\mu}_r}{\delta t} = \gamma\boldsymbol{\mu}_r \times (\boldsymbol{B} + \frac{\boldsymbol{\omega}}{\gamma}) \tag{1.21a}$$

or

$$\frac{\delta\boldsymbol{\mu}_r}{\delta t} = \gamma\boldsymbol{\mu}_r \times \boldsymbol{B}_{\mathit{eff}}\,, \tag{1.21b}$$

where we have introduced the effective magnetic field, $\boldsymbol{B}_{\mathit{eff}}$, given by

$$\boldsymbol{B}_{\mathit{eff}} = \boldsymbol{B} + \frac{\boldsymbol{\omega}}{\gamma}\,. \tag{1.22}$$

The effective field consist of the laboratory field, $\boldsymbol{B}$, and a fictional field, $\boldsymbol{\omega}/\gamma$, arising from the rotational motion of the frame. Using the rotating frame and effective field, we can now easily calculate the motion of $\boldsymbol{\mu}$ in the case where the magnetic field is aligned with the z-axis. By choosing $\boldsymbol{\omega}$ so that $\boldsymbol{B}_{\mathit{eff}} = 0$, the time derivative of $\boldsymbol{\mu}_r$ with respect to the rotating frame,$\delta\boldsymbol{\mu}_r/\delta t$, vanishes. This signifies that $\boldsymbol{\mu}$ remains fixed with respect to the axes of the rotating frame. It is easily seen from Equation (1.22), that by setting $\boldsymbol{\omega} = -\gamma B_0\hat{\boldsymbol{z}}$, i.e. along the negative z-axis, we achieve our goal. With respect to the laboratory frame then, $\boldsymbol{\mu}$ is precessing clockwise around the z-axis with the Larmor frequency $\omega = \gamma B_0$.

Precession in a time dependent field

So far we have looked at the behaviour of $\boldsymbol{\mu}$ in a static magnetic field. We now introduce an alternating field, $\boldsymbol{B}_1$, in the x–y plane:

$$\boldsymbol{B}_1(t) = B_1\big(\hat{\boldsymbol{x}}\cos(\omega_z t) + \hat{\boldsymbol{y}}\sin(\omega_z t)\big)\,, \tag{1.23}$$

where ω_z is the angular frequency of the rotating field. The field is rotating in the x–y plane, i.e. $\boldsymbol{\omega}_{\text{field}} = \hat{\boldsymbol{z}}\omega_z$, and a positive ω_z means a counterclockwise rotation. We want to know what the motion of $\boldsymbol{\mu}$ will be in the combined field of $\boldsymbol{B} = \hat{\boldsymbol{z}}B_0$ and $\boldsymbol{B}_1$. This is given by the equation of motion

$$\frac{\mathrm{d}\boldsymbol{\mu}}{\mathrm{d}t} = \gamma\boldsymbol{\mu} \times \big(\boldsymbol{B} + \boldsymbol{B}_1(t)\big)\,. \tag{1.24}$$

The time dependency of $\boldsymbol{B}_1$ makes it complicated to find the solution of (1.24) directly, but again the rotating frame comes in handy. We tune the angular frequency of the rotating frame to match the angular frequency of the alternating field, ω_z. Then we take the x'-axis of the rotating frame parallel to $\boldsymbol{B}_1$, and the alternating field is reduced to $\hat{\boldsymbol{x}}'B_1$, i.e. we eliminate the time dependency in the rotating frame. By combining (1.21a) and (1.24) we get a new equation of motion

$$\frac{\delta\boldsymbol{\mu}_r}{\delta t} = \gamma\boldsymbol{\mu}_r \times \big(\hat{\boldsymbol{z}}'(B_0 + \frac{\omega_z}{\gamma}) + \hat{\boldsymbol{x}}'B_1\big) \tag{1.25a}$$

or

$$\frac{\delta\boldsymbol{\mu}_r}{\delta t} = \gamma\boldsymbol{\mu}_r \times \boldsymbol{B}_{\mathit{eff}}\,, \tag{1.25b}$$

where we again introduce an effective magnetic field, this time given by

$$\boldsymbol{B}_{\mathit{eff}} = \hat{\boldsymbol{z}}'(B_0 + \frac{\omega_z}{\gamma}) + \hat{\boldsymbol{x}}'B_1\,. \tag{1.26}$$

Now, what does all this mean? The effective magnetic field is a simple vector-addition of the magnetic field along the x'-axis, B_1, and the static field along the z'-axis, $(B_0+\omega_z/\gamma)$, see Figure 1.10(a). Since the time dependency of B_1 is gone, $\boldsymbol{\mu}_r$ acts as though it feels only the static effective field. The moment therefore precess around $\boldsymbol{B}_{\mathit{eff}}$ with angular frequency γB_{eff}, illustrated in Figure 1.10(b). As this precession is periodic, a moment initially aligned along the z-axis will periodically return to that direction. When the angular frequency of the alternating field fulfills the resonance condition, i.e. $\omega_z = -\gamma B_0$, the static field vanishes, and the effective field is simply $\hat{\boldsymbol{x}}'B_1$. This is interesting, because if $\boldsymbol{\mu}$ is initially aligned with the z-axis, it will remain perpendicular to the alternating field, after it is turned on. Since we have chosen $\boldsymbol{B}_1$ along the x'-axis, the moment precesses only in the y'–z' plane. If we are able to turn the alternating field on and off again within a very short time, this means that we can turn the direction of $\boldsymbol{\mu}$ to any direction within this plane.

As $\boldsymbol{\mu}$ precess around $\hat{\boldsymbol{x}}'B_1$ with angular frequency γB_1, the time needed to turn

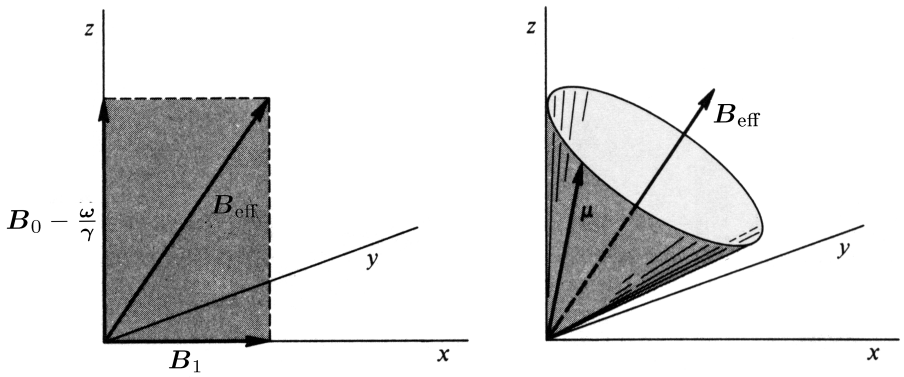

FIGURE 1.10: **a)** The effective field and its components. **b)** The magnetic moment precessing around the effective field. Adapted from [38].

the moment θ radians is given by

$$\theta = \gamma B_1 t \, . \tag{1.27}$$

The special cases of $\theta = \pi/2$ and $\theta = \pi$ are respectively called *90* or *180 degree pulses*. When a 90 degree pulse is applied, $\boldsymbol{\mu}$ precesses through 90 degrees, turning it from the z-direction to the y'-direction. After the pulse, the moment continues to point in this direction, which means that in the laboratory frame, it precesses in the x–y plane, perpendicular to $\boldsymbol{B}$. Application of a 180 degree pulse inverts $\boldsymbol{\mu}$, making it point in the negative z-direction. These kind of short applied pulses of B_1-field are also called RF pulses, since the field normally oscillates in the radio-frequency range [39].

1.2.3 Bulk magnetization

The systems and materials studied with NMR can hardly be said to consist of only single magnetic moments. Even the tiniest of samples contains a vast amount of spins. The quantity measured is therefore not the single magnetic moment, $\boldsymbol{\mu}$, but the macroscopic magnetization vector, $\boldsymbol{M}$. The magnetization is given by the density of the magnetic moments within a volume element V:

$$\boldsymbol{M} = \frac{1}{V} \sum_k \boldsymbol{\mu}_k \, , \tag{1.28}$$

where the summation extends over all moments within the volume.

Without the presence of a magnetic field, the magnetization is zero. This is

because all the individual moments point in random directions, which as a whole even out. When a field is applied though, they are in a way forced to choose side and align themselves in one of the quantum mechanically allowed directions. An illustration can be found in Figure 1.11. To reduce the extent of this discussion, we confine ourself to the case where $I = 1/2$, i.e. two directions/energy levels.

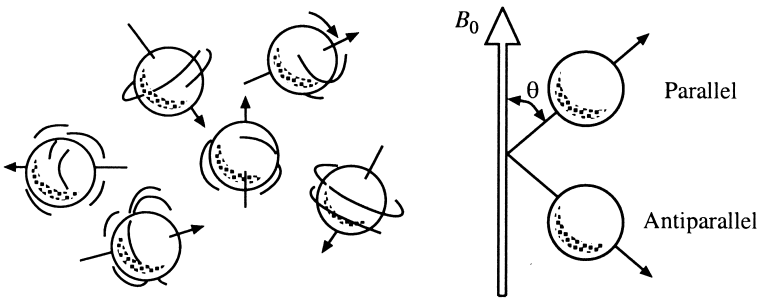

FIGURE 1.11: **a)** Without the presence of a magnetic field the magnetic moment vectors point in random directions. **b)** When a field is present, they are forced into one of two states, either parallel or antiparallel to the field. Adapted from [39].

As already noted in Section 1.2.1, the nucleus might be in either of the two energy states when we turn the magnetic field on:

$$E_{\uparrow} = -\frac{1}{2}\gamma\hbar B_0 \tag{1.29a}$$

$$E_{\downarrow} = \frac{1}{2}\gamma\hbar B_0\,. \tag{1.29b}$$

Although $E_{\uparrow}$ has the lowest energy of the two, all the moments do not immediately fall into this state. The reason for this is that at experimental conditions, the thermal energy $k_B T$ is much larger than than the energy difference between the two energy states. Consequently we are left with calculating the probability of excess spins in the favourable state. To do this, we utilize the well-known Boltzmann relationship

$$\frac{N_{\uparrow}}{N_{\downarrow}} = e^{\frac{\Delta E}{k_B T}}\,, \tag{1.30}$$

where we have introduced $N_{\uparrow}$ and $N_{\downarrow}$, the number of spins in the two energy states, and the Boltzmann constant k_B.

We can find a first-order approximation to (1.30) by utilizing the fact that

$\Delta E \ll k_B T$:

$$\frac{N_\uparrow}{N_\downarrow} = e^{\frac{\Delta E}{k_B T}} \approx 1 + \frac{\Delta E}{k_B T} \Rightarrow$$
$$N_\uparrow \approx N_\downarrow \left(1 + \frac{\Delta E}{k_B T}\right) \Rightarrow$$
$$N_\uparrow - N_\downarrow \approx N \frac{\gamma \hbar B_0}{k_B T} \,. \tag{1.31}$$

In the above equation, N is the total number of spins. We see that there exists an uneven distribution between the two energy states, albeit small. It is so small in fact, that with an applied field of 1T at room temperature, the difference is about 3 in a million (3 ppm) for protons [39]. This difference generates the magnetization vector $\boldsymbol{M}$, which can be observed in NMR spectroscopy.

When the magnetic field is pointing in the positive z direction, the magnetization is also along z because the x and y components average out in thermal equilibrium. We use this to find an expression for the magnetization

$$M_0 = \sum_{k=1}^{N} \mu_{z,k} = \gamma \hbar \sum_{k=1}^{N} m_{z,k} = \frac{1}{2}(N_\uparrow - N_\downarrow)\gamma \hbar$$
$$= \frac{\gamma^2 \hbar^2 B_0 N}{4 k_B T} \,, \tag{1.32}$$

where M_0 is the magnitude of the magnetization vector $\boldsymbol{M} = \hat{\boldsymbol{z}} M_0$. It is worth mentioning that to increase the magnetization of a given sample, the only controllable parameters are the temperature and magnetic field. In the cases where it is impractical or impossible to lower the temperature, only the magnitude of the magnetic field remains.

1.2.4 Relaxation

In Section 1.2.2 we used the rotating frame to study the movement of $\boldsymbol{\mu}$ in an alternating magnetic field. We arrived at the conclusion that a rotating field applied along the x'-axis may turn the moment from z to any angle in the y'–z' plane, leaving it to precess at that angle after the alternating field is turned off. Nothing was said at that time about the return of the system to thermal equilibrium, a topic we will study further in this section. The thermal equilibrium of the system in this context, is when the magnetization is aligned with the static magnetic field B_0. For the magnetization to return to equilibrium from a perturbed state, the spins must give up energy, i.e. there must be a heat transfer from the magnetic moments to the lattice surrounding the moments. A rather thorough derivation on this topic can

be made, using the probabilities of induced and spontaneous transitions, transition rates, available spin states, etc. For simplicity's sake, we will avoid this path.

The Bloch equations

Instead, we introduce the *Bloch equation*, first proposed by Felix Bloch:

$$\frac{\mathrm{d}\boldsymbol{M}}{\mathrm{d}t} = \gamma \boldsymbol{M} \times \boldsymbol{B} - \frac{\hat{\boldsymbol{x}} M_x + \hat{\boldsymbol{y}} M_y}{T_2} - \frac{\hat{\boldsymbol{z}} (M_z - M_0)}{T_1} . \tag{1.33}$$

This equation quantitatively describes the time-dependent behaviour of $\boldsymbol{M}$ in the presence of an applied magnetic field. T_1 and T_2 are time constants of the spin system characterizing respectively the recovery of M_z and the destruction of M_x and M_y. The process behind T_1 is called *longitudinal relaxation*, while the process behind T_2 is called *transverse relaxation*. Due to its nature, T_2 is also called the *spin-spin relaxation time*. Here, the Bloch equation is simply presented without any proof. For a more thorough derivation, and a discussion of the mechanism behind it, the reader is referred to e.g. Slichter [38].

In the rotating frame, the time derivative of the magnetization, $\delta \boldsymbol{M}_r / \delta t$, can be expressed as

$$\frac{\delta \boldsymbol{M}_r}{\delta t} = \gamma \boldsymbol{M}_r \times \boldsymbol{B}_{\mathit{eff}} - \frac{\hat{\boldsymbol{x}}' M_{x'} + \hat{\boldsymbol{y}}' M_{y'}}{T_2} - \frac{\hat{\boldsymbol{z}}' (M_{z'} - M_0)}{T_1} , \tag{1.34}$$

where the derivation from Equation (1.33) is similar to the derivation of Equation (1.25). In most cases, the time it takes an RF-pulse to turn the magnetization from the z-axis to the desired angle is much shorter than the time constants T_1 and T_2. We are therefore justified in considering the effect of relaxation only after the applied pulse. If we choose the angular frequency of the rotating frame to match the Larmor frequency, the first term in Equation (1.34) drops out, and we have the differential equations

$$\frac{\mathrm{d}M_{z'}}{\mathrm{d}t} = -\frac{M_{z'} - M_0}{T_1} \tag{1.35}$$

$$\frac{\mathrm{d}M_{x'y'}}{\mathrm{d}t} = -\frac{M_{x'y'}}{T_2} , \tag{1.36}$$

where we have introduced $M_{x'y'}$, the magnitude of the transverse magnetization in the rotating frame. By solving Equations (1.35) and (1.36), we obtain the time

dependencies of the transverse and longitudinal magnetization after an RF pulse:

$$M_{z'}(t) = M_0\left(1 - e^{-\frac{t}{T_1}}\right) + M_{z'}(0)e^{-\frac{t}{T_1}} \tag{1.37}$$

$$M_{x'y'}(t) = M_{x'y'}(0)e^{-\frac{t}{T_2}}\,. \tag{1.38}$$

We see that both are exponential functions. The constants $M_{z'}(0)$ and $M_{x'y'}(0)$ are the magnetizations immediately after the RF pulse. It is worth noting that Equation (1.38) applies only to systems with weak spin-spin interactions. For the materials we are concerned with, this description is adequate, but for solids and macromolecules, the mechanisms for transverse relaxation are more complicated [39].

The time dependencies of Equations (1.37) and (1.38) are illustrated in Figure 1.12. One clearly sees that the times T_1 and T_2 do not mark the completion of the longitudinal and transverse relaxations, but that these times instead define the rate of the exponential growth and decay. A simple illustration is to calculate the transverse magnetization at the time $t = T_2$:

$$M_{x'y'}(T_2) = M_{x'y'}(0)e^{-\frac{T_2}{T_2}} = M_{x'y'}(0)e^{-1} = 0.37 \times M_{x'y'}(0)\,. \tag{1.39}$$

We see that the transverse magnetization at $t = T_2$ is not zero, but has been reduced to 37% of its initial value.

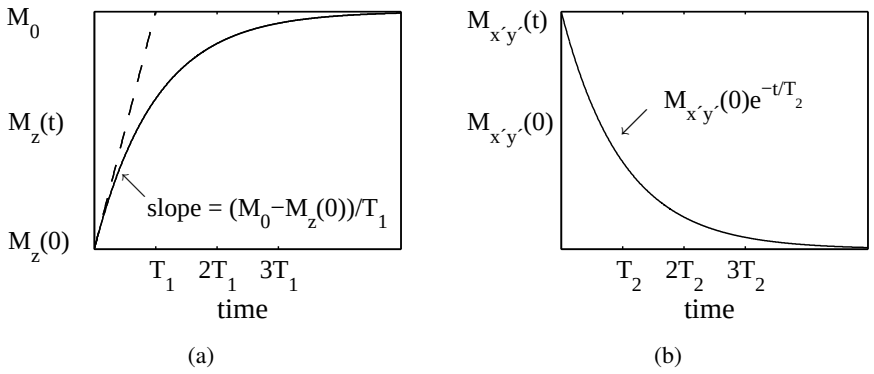

FIGURE 1.12: The time dependencies of the **a)** longitudinal and **b)** transverse Bloch equations. Adapted from [41].

The nature of the transverse relaxation

The relaxation of the transverse magnetizations is always faster than the longitudinal relaxation, i.e. $T_2 < T_1$. This fact is easily explained by looking at the

mechanisms behind T_2. The transverse relaxation is the sum of the mechanisms behind T_1 and the spread in precession rates of the individual spins, illustrated in Figure 1.13. Because the spins are situated at different locations in a macroscopic sample, and the vibrations, magnetic shielding, etc. are non-homogeneous throughout the sample, there will always be a slight spread in the magnetic field felt by the individual spins. This leads to a dephasing of the transverse magnetization vector. Furthermore, if the transverse relaxation was simply due to the longitudinal relaxation, T_1 and T_2 might at most be equal, since no net transverse magnetization remains in thermal equilibrium. For liquids, T_2 is sometimes several seconds, whereas for solids it is a fraction of a millisecond [38].

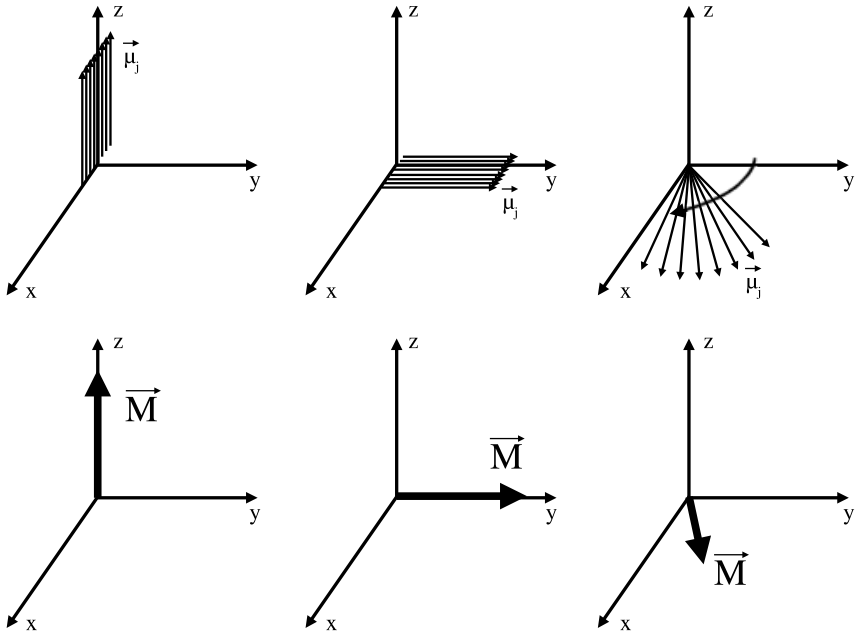

FIGURE 1.13: Illustration of the mechanisms behind transversal relaxation. The top row shows the spins of a sample flipped 90° into the transversal plane and the subsequent precession of the individual spins. The bottom row shows the same process for the net transverse magnetization. The decrease in magnitude occurs because the spins fan out during precession. Adapted from [41].

Free induction decays

When the bulk magnetization of a sample is excited from equilibrium and precesses in the static magnetic field, we can use the precession to generate a signal in a coil positioned around the sample. The most basic forms of these transient signals are called *free induction decays*, or FIDs. *Free* refers in this context to the spins

precessing about the B_0 field, free from B_1, *induction* refers to how the signal is produced, i.e. electromagnetic induction in the reception coil, and *decay* reflects the characteristic decrease of the signals amplitude, due to transverse relaxation [38]. An example FID is shown in Figure 1.14.

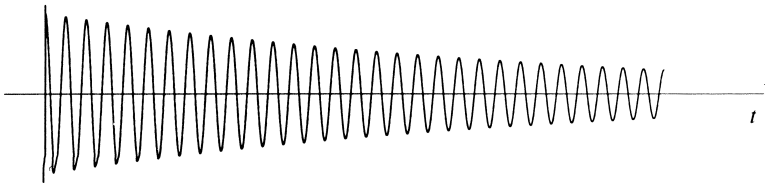

FIGURE 1.14: Example of a simulated FID signal from a system with one isochromat. Adapted from [39].

The two basic parameters of a FID signal are its magnitude and decay rate. The magnitude is dependent on a number of parameters, in particular the flip angle, the total number of spins in the sample, and the magnetic field strength [39]. Naturally, the largest magnitude is achieved with a 90 degree pulse. If the sample measured upon contains only one single resonance frequency, the resulting FID would be a sinusoidal function with decaying amplitude. On the other hand, no real sample consists of spins with only one sharp frequency, and the shape of a FID signal is instead dependent on the spectral density of resonance frequencies in the system, $\rho(\omega)$. Mathematically, we can represent an idealized FID signal resulting from an α pulse as

$$S(t) = \sin\alpha \int_{-\infty}^{\infty} \rho(\omega) e^{-t/T_2(\omega)} e^{-i\omega t} \mathrm{d}\omega\,, \quad t \geq 0\,. \tag{1.40}$$

From the equation above we might be led to believe that the decay rate of a real FID signal is only dependent on T_2, the spin-spin relaxation time. In reality, it is in fact dominated by the degree of field inhomogeneity. This will be further explained in the next section.

1.2.5 Spin echoes

The phenomenon known as *spin echoes* was first discovered by Erwin Hahn in 1950 [43], a discovery which led to the development of pulse methods in NMR. A short introduction is as follows: Say we apply a 90 degree pulse to a magnetic system in thermal equilibrium. This rotates the magnetizations vector into the x–y plane, making it precess freely in that plane. Around the sample we have a coil which we use to observe the precession of $\boldsymbol{M}$. This is done by recording the current induced in the coil by the precessing magnetization. After a time in the order of a few T_2, the signal will nearly have vanished. We then apply another

pulse, this time turning the magnetization 180 degrees. At first, this does not give any signal in our reception coil, but after a time equal to the time between the two RF-pulses, the precession signal magically returns. We have observed a spin echo.

In order to understand spin echoes we must first elaborate some on T_2, the spin-spin relaxation time introduced above. Remember that T_2 is the time constant characterizing the exponential decay of the transverse magnetization. In Equation (1.38), stated above, we have assumed the static magnetic field B_0 totally homogeneous. Ideally we would want this to be true, but in reality it is hardly the case. With a non-homogeneous magnetic field, we introduce a new time constant

$$\frac{1}{T_2^*} = \frac{1}{T_2} + \gamma \Delta B_0 \tag{1.41}$$

based on the time constant for the internal sample-dependent spread in the magnetic field, T_2, and the spread in the external static magnetic field, ΔB_0. T_2^* may in many cases be used in Equation (1.38) instead of T_2. Because T_2^* is inversely proportional to ΔB_0, the transverse magnetization will diminish faster with increasing field inhomogeneity, and always faster than solely the spin-spin relaxation T_2. This is where Erwin Hahn and his spin echoes lends a helping hand.

The reason why a non-homogeneous magnetic field will speed up the transverse relaxation is most easily understood in the rotating frame. We consider a magnetization vector at time $t = 0$, already located along the y'-axis, i.e. after a 90 degree pulse. If we take the applied magnetic field across the sample to be $B(\boldsymbol{r}) = B_0 + \Delta B_0(\boldsymbol{r})$, the angular frequencies of the precessing moments will lie in the interval $\gamma(B_0 - \Delta B_0) < \omega < \gamma(B_0 + \Delta B_0)$. Setting the angular frequency of the rotating frame at $\omega = \gamma B_0$, it becomes obvious that the initially collimated magnetic moments will spread out in the x'–y' plane, some moments rotating faster than $\hat{\boldsymbol{y}}'$, others lagging behind. This "smearing out" of $\boldsymbol{M}$ is similar to the fanning of the spins illustrated in Figure 1.13, but is field dependent instead of sample dependent.

Now why does a 180 degree pulse give rise to a refocused signal even after this smearing out is finished? The explanation is as follows: At time $t = \tau$ we apply the 180 degree pulse along the y'-axis, in other words we mirror all the moments around $\hat{\boldsymbol{y}}'$. The moments that had precessed α degrees beyond $\hat{\boldsymbol{y}}$, are now located α degrees behind, while the moments lagging β degrees are now β degrees ahead. As the moments continue to precess in the non-homogeneous magnetic field, they refocus, and will at time $t = 2\tau$ again be collimated along the y'-axis.

A whole range of different pulse sequences exists, each with different results and uses. The 90°–180° pulse sequence described above, shown in Figure 1.15, is for example used to determine the value of T_2. Note that the *echo time*, T_E, given

by $T_E = 2\tau$ is commonly used in relation to pulses instead of τ.

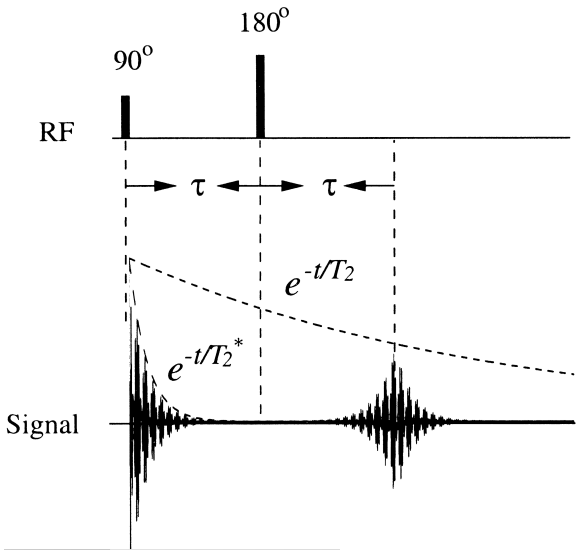

FIGURE 1.15: The 90°–180° sequence is one of the ways to form a spin echo. A FID decaying with T_2^* is formed after the 90°-pulse, while the 180°-pulse at time τ produces an echo at 2τ. Adapted from [39].

1.2.6 Other aspects of NMR

When the resonance of magnetic nuclei is studied with NMR, the frequency at which we observe resonance is not simply given by the Larmor frequency $\omega = \gamma B_0$. One of the properties of magnetic resonance that makes NMR such a powerful tool, is the fact that the resonance from a nucleus is also dependent on the nucleus' surroundings. The two most important phenomena behind this property are the *chemical shift* and the *spin-spin coupling*.

The chemical shift

Within a molecule a nucleus might be located at different chemical environments. Let us for simplicity consider a ^{1}H nucleus (proton). The electron density surrounding the proton shields or screens the magnetic field, thus changing the magnetic field sensed by the proton. This leads to the phenomenon known as the chemical shift. If we let the proton feel a magnetic field ΔB in addition to the applied field, the resonance frequency changes to

$$\omega = \gamma(B_0 + \Delta B) \tag{1.42}$$

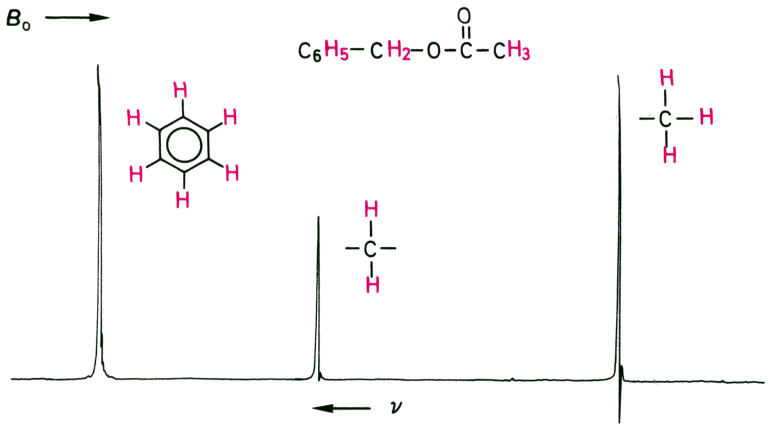

FIGURE 1.16: A hypothetical NMR spectrum from benzyl acetate illustrating the chemical shift. The splitting of the ^{1}H signal into three distinct peaks results from the three different chemical environments the proton is located at. Adapted from [42].

or

$$\omega = \gamma B_0(1-\sigma)\,, \tag{1.43}$$

where we have introduced the screening constant σ, given by $\Delta B = -\sigma B_0$. The screening constant might differ at several locations within a molecule, thus making it possible to extract information about the molecular structure with NMR spectroscopy. An illustration can be found in Figure 1.16.

It is clear from Equation (1.43) that because ω is dependent on both σ and B_0, no absolute spectral reference exists for NMR spectroscopy. Ideally, one could measure the strength of the external field B_0 and the resonance frequencies ω, at which the resonance lines occur. By knowing the field strengths used in other measurements, comparison would be possible. Technically though, precise measurements of field strength and resonance frequency is difficult.

What one instead does, is to measure the resonance signal relative to a *reference compound* or a *standard*, which must be measured upon at the same time as the sample of interest. In ^{1}H-NMR, the most used standard is *tetramethylsilane* (TMS), which gives a sharp peak that seldom overlaps with other proton resonances. After recording an NMR spectrum including the standard, a dimensionless quantity, δ, is computed:

$$\delta = \frac{\nu_{sample} - \nu_{reference}}{\nu_0}\,, \tag{1.44}$$

where ν_0 is the operating frequency of the spectrometer. This is shown in Figure 1.17. The chemical shift measured with δ is independent of the magnetic field

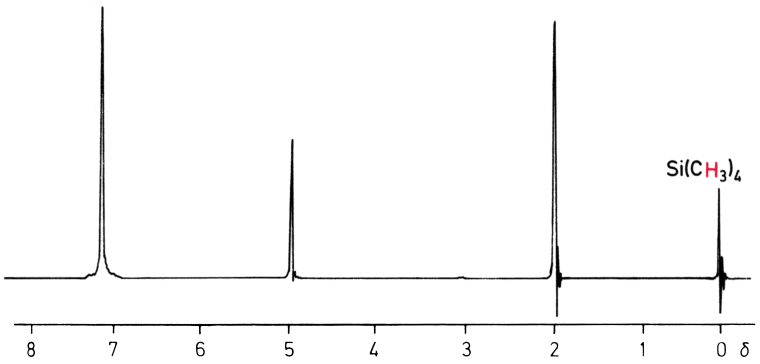

FIGURE 1.17: The ^{1}H NMR spectrum from benzyl acetate recorded with TMS ($Si(CH_3)_4$) as a reference compound. Adapted from [42].

and operating frequency, and may therefore be used as a spectral scale.

Spin-spin coupling

Another phenomenon present in NMR studies is the spin-spin coupling. This interaction occurs between nuclei that are indirectly connected by bonding electrons. Because the bonding electrons have overlapping orbitals and electrons are fermions, the bonding electrons cannot coexist in the same quantum state. What happens as a result of this, simplified of course, is the following: Given two nuclei in an external magnetic field, nuclei A and X, both with $I = 1/2$, sharing two bonding electrons, when nucleus A is aligned with the magnetic field, its bonding electron is polarized. This in turn polarizes the bonding electron of nuclei X due to the Pauli principle. An illustration can be found in Figure 1.18. The polarization of the bonding electron at nuclei X affects the magnetic field seen by X, thus splitting the NMR signal from X to a doublet. As the same reasoning goes the other way, the resonance frequency of A is coupled to X as well. In cases when $I > 1/2$ and/or more than two nuclei are coupled, the spin-spin coupling might introduce even more complex fine-structure to the resonance signal than a doublet.

An important distinction between the spin-spin coupling and the chemical shift is the difference in magnetic field-dependence. From Equation (1.42), the chemical shift is obviously dependent on B, the spin-spin coupling, however, is not [42]. If the frequency spectrum of an NMR scan is unclear, one might therefore deduce what lines in an NMR spectrum arise from which phenomenon, by varying the magnetic field.

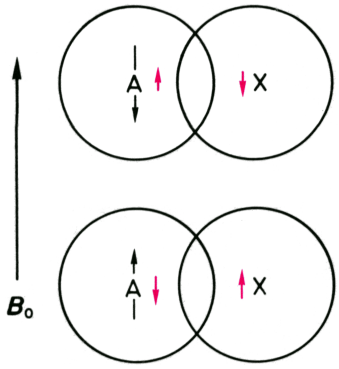

FIGURE 1.18: Schematic representation of the spin spin coupling. The nuclear moment is represented as ↑, the magnetic polarization of the electron as ↓. Adapted from [42].

1.3 Magnetic Resonance Imaging

Short introduction

When we perform NMR experiments, we utilize the magnetic resonance phenomenon by exciting the sample under investigation as a whole. The signal generated is the sum of "local" signals from all parts of the object. Magnetic Resonance Imaging (MRI) experiments differ from NMR experiments in that we want to differentiate the local signals from different parts of a given object, and use this to make images. The first to conceive the idea of using magnetic field gradients to achieve this was Paul Lauterbur [35]. He published his first article on the subject in Nature in 1973 [44], and called the technique *zeugmatography*. In 2003, Lauterbur was honored for his work, when he shared the Nobel prize in Medicine with Peter Mansfield. As in the case of NMR, the development of MRI from its small beginning has been exponential. Lauterbur's initial thoughts on MRI applications were medical imaging [45], and it took only four years before the first live human NMR image was published [46]. Today, MRI is an invaluable tool for diagnostics in medicine, but it also finds uses in many scientific fields, including physics, which this thesis proves.

When doing MRI experiments one utilizes, and must know of, all or parts of the NMR phenomena already described in the previous sections. This includes flip angle pulses, spin echoes, free induction decays, etc. Many textbooks has been written on the subject of MRI, and the aim of this section is by no means to give a complete recollection of MRI theory. It is rather meant as a framework for the later understanding and discussion of the experiments we performed using this technique. In the following we will first introduce magnetic gradients and gradient echoes, and then explain the basics concepts of signal localization by the use of

spatial information encoding. The mathematics of the FID signals will only be dealt with at the end, in connection with the k-space notation.

1.3.1 Gradient echoes

In the discussion about spin echoes in Section 1.2.5 above, we stated that a non-homogeneous magnetic field reduces the transverse relaxation time, making NMR spectroscopy more difficult. The application of gradient fields – a concept which therefore may seem strange, being a willing introduction of non-homogeneity – is frequently utilized in MRI. The essential difference between the intrinsic non-homogeneity of the static field, and the applied gradient fields, is that the non-homogeneity introduced by the gradient field is both controllable, linear and reversible. Gradient fields are utilized both in a form of spin echoes called *gradient echoes*, and to differentiate the NMR signal from different spatial regions of the sample.

Gradient fields

An applied magnetic gradient will have components in both x-, y- and z-directions. As we are only interested in the z-component, and because the B_0 field is so strong in the z-direction, we may choose to ignore the other components [39]. The gradient field, $B_{G,z}$, is a special kind of inhomogeneous field whose z-component varies linearly along a chosen direction called the gradient direction. The gradient direction is determined by the field produced by three different coils referred to as the x-gradient, y-gradient and the z-gradient coils. If only one of the gradient coils is switched on

$$B_{G,z} = G_x x\,, \quad B_{G,z} = G_y y \quad \text{or} \quad B_{G,z} = G_z z\,, \tag{1.45}$$

we call the gradient field an x-gradient field, y-gradient field or z-gradient field, respectively. In any of these gradient fields, the z-component of the magnetic field varies linearly along the chosen direction.

When all the gradient coils are turned on simultaneously, the gradient field points in a direction determined by the three individual coils,

$$B_{G,z} = G_x x + G_y y + G_z z\,. \tag{1.46}$$

resulting in the total magnetic field

$$\boldsymbol{B} = \hat{\boldsymbol{z}}(B_0 + G_x x + G_y y + G_z z)\,. \tag{1.47}$$

We may also introduce a gradient vector $\boldsymbol{G}$ that points in the gradient direction.

The gradient vector is naturally given by the sum of the x-, y- and z-gradients

$$\boldsymbol{G} = \hat{\boldsymbol{x}} G_x + \hat{\boldsymbol{y}} G_y + \hat{\boldsymbol{z}} G_z \,, \tag{1.48}$$

and it is important to note that $\boldsymbol{G}$ is generally a function of time.

Gradient echoes

The key concept of gradient echoes is that the gradients provide a method to dephase and rephase the magnetization in a controlled way. By doing this, one or multiple echoes can be created. The time between echoes created in this manner may be significantly less than with the conventional spin echo sequence described in Section 1.2.5. Let us for simplicity consider the basic pulse sequence illustrated in Figure 1.19. We apply an RF-pulse, flipping the magnetization α degrees away from the z-axis, and immediately turn on a negative x-gradient. The effects of the gradient are most easily understood from the rotating frame, where the gradient introduces different phases across the sample, dependent on position. If we let τ be the time the gradient is turned on, the acquired phase can be expressed as

$$\phi(x,t) = \begin{cases} -\gamma G_x x t \,, & 0 \leq t \leq \tau \\ -\gamma G_x x \tau \,, & t \geq \tau \,, \end{cases} \tag{1.49}$$

indicating that the spins become less and less coherent during the application of the gradient.

We can also invert the gradient at time $t = \tau$, making it positive. Inverting the gradient only changes the sign of G_x, and Equation (1.49) is therefore still valid. The resulting phase angle from both the negative and positive gradients is

$$\phi(x,t) = -\gamma G_x x \tau + \gamma G_x x (t - \tau) \,, \quad \tau \leq t \leq 2\tau \,. \tag{1.50}$$

We see from Equation (1.50) that $\phi(x,t)$ is zero at $t = 2\tau$. At that point, the positive gradient has refocused the signal, and an echo is observed. This analysis is easily extended to the cases of unequal dephase and rephase gradients, both in time and strength, or even a delay between the gradients. Note that the echo time in those cases may not be equal to 2τ.

One of the essential differences between this gradient-echo sequence and the pulse-echo sequence described earlier, is the decay rates of the FID signal and the subsequent echo amplitudes. In the pulse-echo sequence, the FID decay was characterized by the T_2^*-constant, while the echo amplitudes decayed with the slower T_2-weighting. In the gradient-echo sequence, the FID decay is dependent on the strength of the gradient, while the echo amplitudes decay with the fast

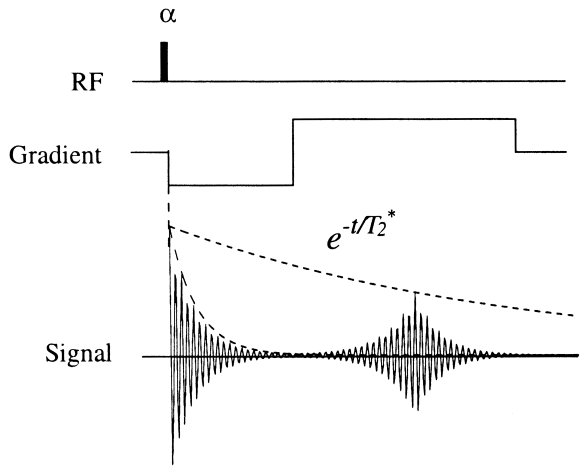

FIGURE 1.19: A basic gradient echo pulse sequence. After the application of a flip-angle pulse a negative x-gradient is used to dephase the spins. The x-gradient is then inverted, resulting in a rephasing of the spins. Note the T_2^*-dependence on the amplitude decay. Adapted from [39].

T_2^*-weighting. Consequently, the gradient-echo method may create many echoes within the time period of only one pulse-echo.

1.3.2 Slice selection

The easiest way to record a signal from only a part of a sample is to record the signal from a *slice*. By a slice, we mean a two-dimensional plane with a certain thickness. With the x-, y- and z-gradient coils of an MRI system, a slice may be selected in any direction, but most common are the slices perpendicular to the x-, y- and z-directions, called sagittal, coronal and transverse slices, respectively [39]. These slices are shown in Figure 1.20.

The way to record the signal from only a slice is through the use of a gradient. Without this, a flip-angle pulse will, as we have already discussed, excite all the spins in the sample. If we apply the gradient to the sample during the excitation period, the z-component of the magnetic field will vary linearly along the gradient direction in correspondence with Equation (1.47). If we are able to apply a flip angle pulse with a limited frequency spectrum, only the slice of the sample whose resonance frequencies correspond to the frequencies of the RF-pulse will be excited.

A flip angle pulse with only a limited frequency spectrum is called a *slice-selective RF pulse*. Ideally, we would want to create a pulse that has frequency components only in the same region as the frequencies in our slice. In reality this

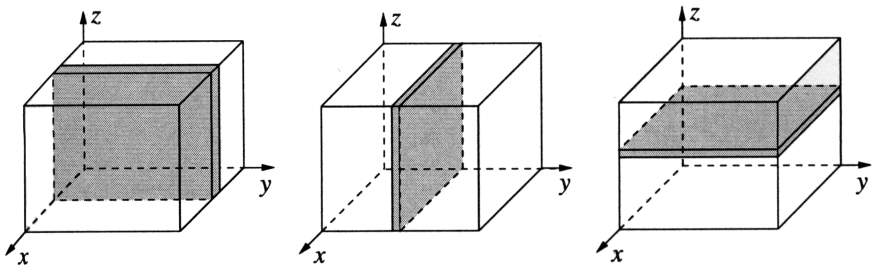

(a) (b) (c)

FIGURE 1.20: The three basic MRI-slices, selected along the **a)** x-direction, **b)** y-direction, and **c)** z-direction. Adapted from [39].

is not possible, since a pulse that is a perfect rectangular window function in the frequency domain, would have to be infinitely long in the time domain. Instead we must resort to pulses that are truncated to a finite duration. The consequence of this, is that the pulses used in practice also contain some frequencies that excite the spins in the neighbouring slices. This is known as the *crosstalk* artifact [41]. A thorough derivation on how to construct slice selective pulses and reduce crosstalk is too lengthy to include here, the reader is instead referred to e.g Haacke et al. [41].

The final part of isolating the signal from a slice is to rephase the excited spins. Remember from Section 1.3.1 that a gradient applied after a flip angle pulse will dephase the precessing magnetization. This is true for a slice selection gradient as well, since the gradient introduces different phases within the slice. Analogous to the case of gradient echoes, the rephasing is done by applying a negative gradient after the slice selection gradient. An illustration of a slice selective RF-pulse and the associated gradients is shown in Figure 1.21.

1.3.3 Spatial information encoding

The slice selection method described above gives us a way to selectively extract the signal from only a slice of the sample. This might find some uses on its own, but to perform three-dimensional imaging, slice selection alone is not adequate. In addition we need some way to encode spatial information into the signal, enabling us to separate the signal from different parts within the slice. There are essentially two different ways to do this, *frequency encoding* and *phase encoding*. The essential difference between using the gradients for encoding, and applying them to make slice selection, is that while slice selective gradients are applied in conjunction with RF-pulses, frequency and phase encoding are both performed after the spins have been activated.

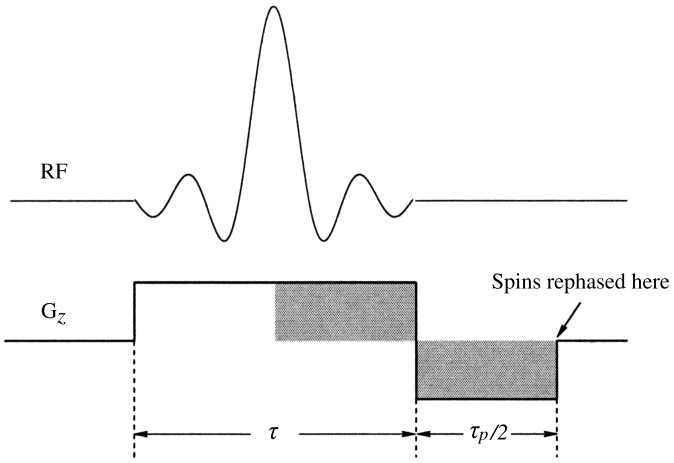

FIGURE 1.21: Example of the slice-selective RF pulse and the associated gradients for a transverse slice selection. Adapted from [39].

Frequency encoding

As the name implies, frequency encoding makes the oscillation frequencies of the spins dependent on the spatial location. We achieve this by the use of gradients, utilizing the same principle as we did to make a slice selection. The Larmor frequency of the spins are dependent on the magnetic field, so the presence of a magnetic gradient will introduce a frequency gradient across the sample. If we e.g. apply an x-gradient field, the x-dependence of the Larmor frequency at position x is given by

$$\omega(x) = \omega_0 + \gamma G_x x \,. \tag{1.51}$$

An illustration can be found in Figure 1.22.

An important note about frequency encoding is that it is not possible to assign a unique frequency to all the points in a sample with frequency encoding alone. It would be a grave misconception to think that by turning on G_x, G_y, and G_z simultaneously, each of the gradients encodes its axis different from the others, thus giving all spatial points its own frequency value. What instead happens is that we frequency encode the sample only along the gradient direction $\boldsymbol{G}_{\text{fe}}$ (Equation (1.48)), giving all the spins within planes perpendicular to $\boldsymbol{G}_{\text{fe}}$ the same frequency. For multidimensional encoding, we therefore introduce phase encoding.

Phase encoding

With the concept of frequency encoding still in memory, phase encoding is extremely easy to understand. It is readily understood from Figure 1.23 alone. As explained above, the spins along the gradient direction precess at different fre-

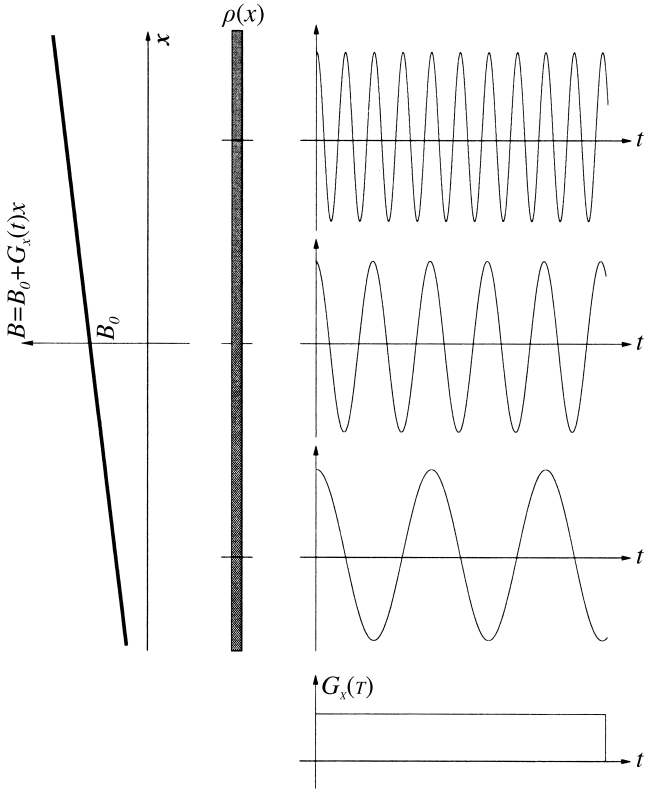

FIGURE 1.22: Frequency encoding along the x-axis. As long as the gradient G_x is applied, the Larmor frequency varies linearly along the gradient direction. Adapted from [39].

quencies during the application of a frequency encoding gradient. When we turn the gradient off again, they are only subject to B_0, and naturally return to the Larmor frequency ω_0. If we only apply the gradient for a short time, T_{pe}, then during the frequency encoding period, all the spins will have accumulated different phases along the gradient direction. In the case of the x-gradient in Figure 1.23, the initial phase angle after the gradient is switched off is

$$\phi(x) = -\gamma G_x x T_{\text{pe}} \,, \tag{1.52}$$

and in the general case it is

$$\phi(\boldsymbol{r}) = \gamma G_{\text{pe}} \boldsymbol{r} T_{\text{pe}} \,. \tag{1.53}$$

It is clear from Equation (1.53) that to adjust the initial phase angle, one must either vary the strength of the phase encoding gradient, or the length of the phase encoding interval.

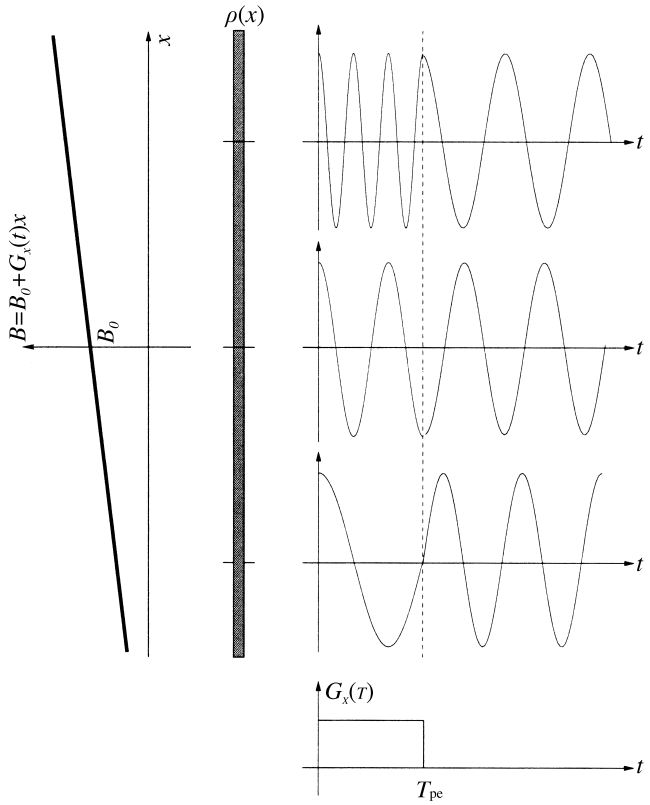

FIGURE 1.23: Phase encoding along the x-axis. When the frequency encoding gradient G_x is turned off, a phase difference across the sample is introduced. Adapted from [39].

1.3.4 Interpreting the MRI signal using *k*-space notation

Having discussed spatial information encoding and slice selective pulses, we are now almost ready to put it all together, and describe what kind of pulse sequences we can use to make three-dimensional images. However, before we do that we must look at the kind of signals one records in MRI, and how to interpret them.

MRI signals

The basic signal recorded in MRI takes the following form:

$$S(t) = \int_{-\infty}^{\infty} \rho(\omega) e^{-t/T_2(\omega)} e^{-i\omega t} \mathrm{d}\omega \,, \tag{1.54}$$

where $S(t)$ is the complex recorded signal, and $\rho(\omega)$ is the spin spectral density function of the sample [39]. This signal expression is simplified, and to arrive at it one must e.g. ignore phase shifts introduced by imperfections in excitation and reception. Within the scope of this thesis it is nevertheless adequate. To make the discussion even easier, we will also neglect the transverse relaxation.

Let us now consider the FID signal recorded from a frequency encoded sample. We stick to one dimension for simplicity. The signal generated at the infinitesimal interval $\mathrm{d}x$ around the point x, is given by

$$\mathrm{d}S(x,t) = \rho(x)\mathrm{d}x e^{-i\omega(x)t} = \rho(x)\mathrm{d}x e^{-i(\gamma G_x x + \omega_0)t} \,, \tag{1.55}$$

where we have omitted all scaling constants and inserted the x-dependent frequency from Equation (1.51). $\rho(x)$ is the spin distribution in one dimension. The spin distribution in three dimensions, $\rho(\boldsymbol{r})$, is generally what we are after in MRI, and how to extract $\rho(\boldsymbol{r})$ from $S(t)$ will soon become clear. The frequency encoded signal received from the entire object is obtained by integrating $\mathrm{d}S(x,t)$:

$$S(t) = \int_{\text{object}} \mathrm{d}S(x,t) = e^{-i\omega_0 t} \int_{-\infty}^{\infty} \rho(x) e^{-i\gamma G_x x t} \mathrm{d}x \,. \tag{1.56}$$

We are generally not interested in the carrier signal, $e^{-i\omega_0 t}$, and remove it by demodulation. The resulting signal is

$$S(t) = \int_{-\infty}^{\infty} \rho(x) e^{-i\gamma G_x x t} \mathrm{d}x \,. \tag{1.57}$$

Transformation to *k*-space

When recording the signals described above, the spin density function is extracted from S through a Fourier transform. The connection between the Fourier transform

and spatial encoding becomes clear by introduction of the k-space. A very handy side effect of this transformation, is that it also enables us to describe complex imaging schemes clearly using the popular k-space notation.

We start by transforming the frequency-encoded signal. By using the simple variable substitution

$$k_x = \gamma G_x t/2\pi \,, \tag{1.58}$$

Equation (1.57) becomes

$$S(k_x) = \int_{\infty}^{\infty} \rho(x) e^{-i2\pi k_x x} \mathrm{d}x \,. \tag{1.59}$$

We see that $S(k_x)$ is the Fourier transform of $\rho(x)$. The spin density function can consequently be reconstructed from the received signal by Fourier transforming $S(k_x)$ after recording it. This is typically done by Fast Fourier Transform algorithms on computers connected to the MRI system. Equation (1.59) can be generalized to three-dimension, where the corresponding $S(\boldsymbol{k})$ is given by

$$S(\boldsymbol{k}) = \int_{\text{object}} \rho(\boldsymbol{r}) e^{-i2\pi \boldsymbol{k}\cdot\boldsymbol{r}} \mathrm{d}\boldsymbol{r} \tag{1.60}$$

and

$$\boldsymbol{k} = \gamma \boldsymbol{G}_{\text{fe}} t/2\pi \,. \tag{1.61}$$

It is also possible to describe the effect of phase encoding as a Fourier transform, where $S(\boldsymbol{k})$ has the same form for phase encoded signals as for the frequency encoded signal in Equation (1.60), but $\boldsymbol{k}$ is different:

$$\boldsymbol{k} = \gamma \boldsymbol{G}_{\text{pe}} T_{\text{pe}}/2\pi \,. \tag{1.62}$$

Note that in phase encoding, $\boldsymbol{k}$ has a fixed value for a given $\boldsymbol{G}_{\text{pe}}$ and T_{pe}, while it is time dependent in frequency encoding.

Sampling of *k*-space

The key to multidimensional imaging lies in generating a sufficient number of signals to cover k-space. The reason for this can be found in a theorem known from signal analysis, the *Nyquist sampling criterion*. The theorem says that to perfectly reconstruct a function that is bandlimited to f_{max} from its sampled values, the minimum sampling rate, f_{s}, needs to be at least twice the highest frequency component of the function

$$f_{\text{s}} \leq 2 f_{\text{max}} \tag{1.63}$$

where f_{s} is called the Nyquist frequency [47].

Here, we will not go into the details of how the different values for $\boldsymbol{k}$ is chosen. Suffice it to say that the field of view (FOV) of the image, i.e. the size of the volume being imaged, is dependent on the distance between k-values [41]

$$\text{FOV} \propto (\Delta k_j)^{-1}\,, \quad j = x, y, z \tag{1.64}$$

and that the image resolution in direction j is given by the maximum k-value in that direction

$$\text{Resolution}_j \propto |k_j^{max}|\,, \quad j = x, y, z\,. \tag{1.65}$$

Assuming we already know what values for $\boldsymbol{k}$ we need to sample to acquire an image, we need to know how to reach the values of $\boldsymbol{k}$, i.e. how to make the signal traverse k-space. The key to this lies in Equations (1.61) and (1.62), which we state again, a bit expanded

$$\boldsymbol{k} = \begin{cases} \gamma \boldsymbol{G}_{\text{fe}} t/2\pi & \text{FID signals} \\ \gamma \boldsymbol{G}_{\text{fe}}(t - T_E)/2\pi & \text{echo signals} \end{cases} \tag{1.66}$$

$$\boldsymbol{k} = \gamma \boldsymbol{G}_{\text{pe}} T_{\text{pe}}/2\pi\,. \tag{1.67}$$

For the equations above, Equation (1.66) applies to the case of frequency encoding, and (1.67) to phase encoding. Lets put the equations to use by considering the two-dimensional imaging scheme shown in Figure 1.24. The sequence use a slice selective pulse and a G_z gradient to excite the spins in a transverse slice. The signal is then phase encoded along the y-axis by G_y, in the time interval T_{pe}. During the signal acquisition period T_{acq}, the signal is frequency encoded by G_x. Note also that the signal is recorded as a spin echo.

At the n-th excitation of this scheme, we have the following values for $\boldsymbol{k}$ in the phase-encoding interval:

$$\begin{cases} k_x = \gamma G_x t/2\pi \\ k_y = \gamma G_{y,n} t/2\pi\,, \end{cases} \quad 0 < t < T_{\text{pe}} \tag{1.68}$$

which moves $\boldsymbol{k}$ in a straight line from the origin to the point A given by

$$\boldsymbol{k}_{\text{A}} = \left(\frac{\gamma G_x T_{\text{pe}}}{2\pi}, \frac{\gamma G_{y,n} T_{\text{pe}}}{2\pi} \right). \tag{1.69}$$

The 180° pulse following the phase encoding inverts point A through the origin, moving $\boldsymbol{k}$ to point B (Figure 1.25(a)). In the subsequent data acquisition interval,

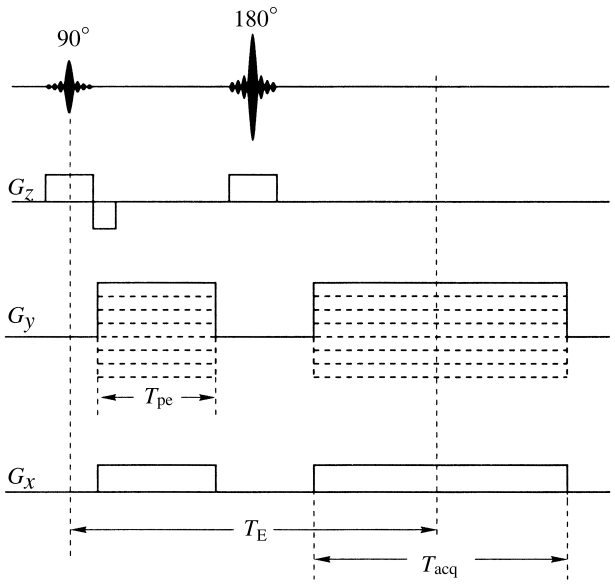

FIGURE 1.24: A two-dimensional imaging sequence, with phase encoding done by G_y and frequency encoding by G_x. Slice selection in the z-direction is achieved by the combination of G_z and the slice selective pulses. Adapted from [39].

the k-space being covered is given by

$$\begin{cases} k_x = \gamma G_x t/2\pi \\ k_y = -\gamma G_{y,n} T_{pe}/2\pi \,, \end{cases} \quad -T_{acq}/2 < t < T_{acq}/2 \tag{1.70}$$

which is a horizontal line parallel to the k_x axis. It is clear from Equation (1.70), that by repeating the sequence and varying $G_{y,n}$ using both positive and negative values, a symmetrical coverage of k-space is achieved.

In general there are vast amounts of variations on imaging schemes, all having different uses of gradients and selective or nonselective pulses, and accordingly different coverages of k-space. The coverage of k-space described above could also have been achieved by keeping the value of $|G_y|$ constant, and varying T_{pe}. We could also have phase encoded along the x-axis and frequency encoded the y-axis. In that case the horizontal lines in Figure 1.25(b) would have been parallel to k_y.

The k-space covered is generally sampled at finite intervals. The resulting rectilinear sampling from the imaging scheme discussed here is shown in Figure 1.25(c). Note that the distance between k_y-values, Δk_y, is given by the steps in $G_{y,n}$, while Δk_x is determined from the interval between sampling times.

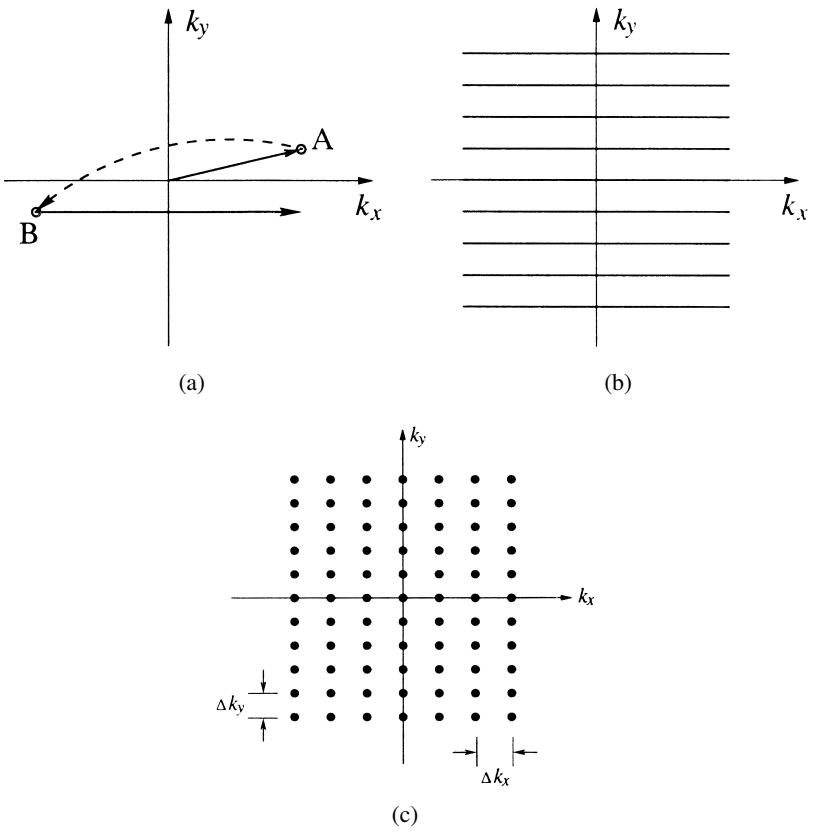

FIGURE 1.25: The two-dimensional coverage of k-space resulting from the imaging sequence in Figure 1.24. **a)** A single excitation cycle. The point A is reached after the phase encoding, while the trajectory from B onwards is the trajectory during acquisition. **b)** The complete k-space coverage by the image scheme. **c)** The finite sampling of the covered k-space. Adapted from [39].

1.4 Rough surfaces

Short introduction

The growth and structure of rough interfaces is a field that has been subject to many studies, see e.g. the review articles by Meakin [48] and Bouchaud [49], from which much of the information in this section is gathered.

1.4.1 Fracture

The reason why a fracture develops in a structure may be due to the application of repeated loads or due to a combination of loads and environmental attacks [50]. A large and potentially deadly crack, e.g. in an airplane fuselage, may start slowly as a microscopic flaw, but grows in size as the structure is continually subject to stress. An understanding of fractures is therefore important, because the residual strength of a structure is decreasing progressively with increasing crack size.

Modes of fracture

It is common to divide fractures into three types, denoted Mode I, Mode II, and Mode III, illustrated in Figure 1.26. Mode I is an opening of the fracture perpendicular to the local fracture plane. This causes tension normal to the fracture surface. Mode II causes the crack surfaces to displace relative to each other within the fracture plane, parallel the fracture direction. Mode III causes a tearing, or anti-plane shear, when the surfaces displace within the fracture plane, perpendicular to the fracture direction. Actual fractures generally consist of a combination of all three modes, and the combination may vary both along the fracture front and during the growth of the fracture [51].

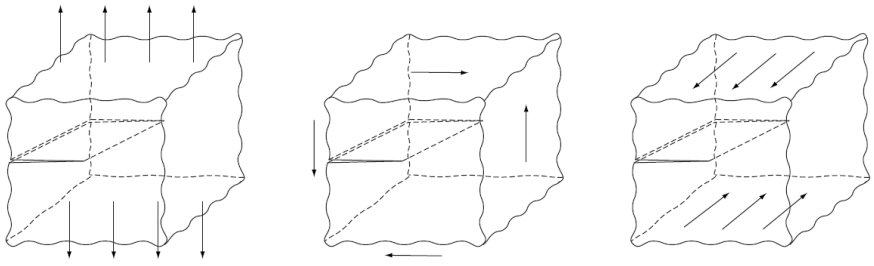

(a) I (tension) (b) II (in-plane shear) (c) III (anti-plane shear)

FIGURE 1.26: Illustration of the three modes of fracture. Adapted from [51].

We can also characterize the kind of deformation caused by stress in a material. *Elastic* deformation means that the deformed material returns to its original shape some time after the applied stress is removed, *plastic* deformation makes a material undergo a non-reversible change of shape, while *viscoelasticity* is a combination of the two. Materials that undergo plastic deformation during fracture are called ductile, and elasticly deformed materials are called brittle.

1.4.2 Roughness

Characterizing roughness and describing the growth of rough surfaces are two related subjects that have seen much scientific interest over the last 30 years. The studies have often been of practical importance, especially due to the wide range of systems that can be considered as rough surfaces. Some examples of subjects that have been treated within this context include material fracture, mountain ridges, the propagation of flame fronts, the growth of bacterial colonies and fluid-fluid displacements processes. Superficially, these processes may be quite different, but research has shown that the scaling properties associated with each of them may be remarkably similar [48].

Many times the growth of a surface can be described in terms of the propagation of a growth front or "active zone" [48]. The creation of the surface is done in the active zone, and after the growth front has passed, the structure left behind does not change.

Characterization of fracture surfaces are now mainly done by studying their *fractal self-affinity*. It was Mandelbrot et al. [52] who first introduced this technique in 1984 [49], when they studied fracture surfaces in steel. In fact, the concept of fractals was first conceived by Mandelbrot himself in 1977 [53], and quickly became an important tool for treating structures that are not easily characterized by Euclidean geometry.

A self-affine object is an object that is statistically invariant through a an affine transformation

$$(x, y, z) \longrightarrow (\lambda x, \lambda y, \lambda^{\zeta} z)\,, \tag{1.71}$$

where z is the height, and x and y are the coordinates within the plane perpendicular to z [49]. ζ is the *roughness exponent*, a quantity that characterizes the roughness of the surface. In the literature, the roughness exponent is sometimes also called the *Hurst* exponent, denoted H, though for the rest of this thesis we will stick to ζ.

Calculating the roughness exponent

There exist plenty of ways of calculating ζ, most of them consisting of calculating some function based on data, and extracting the exponent from the way the function scale. A good review, though not very recent, can be found in Bouchaud [49]. Only the methods used in this thesis will be discussed here, others methods such as *box counting* or the *return probability*, can be found in the literature.

One of the most used methods is to calculate the second order correlation function

$$C_2(r) = \left\langle \big(h(x+r) - h(x)\big)^2 \right\rangle_x^{1/2}, \tag{1.72}$$

where $h(x)$ is a one-dimensional height profile of the surface being studied. The height profile can be measured in various ways, but most common are the use of a profilometer, atomic force microscopy or optical profilometry [48]. $h(x)$ should be measured relative to a flat reference surface that minimizes drift in the surface plane [48], but the profile can also be leveled at a later stage [54]. It can be shown that C_2 scales as

$$C_2 \propto r^{\zeta}, \tag{1.73}$$

where ζ is between 0 and 1 [55]. It is obvious from Equation (1.71) that $\zeta = 1$ means the surface is *self-similar* – it scales in equal amount in all directions – and this corresponds to a regular surface at small length scales [49]. Because ζ is related to the fractal dimension [53] as

$$d_F = 3 - \zeta, \tag{1.74}$$

the lower the value of ζ, the rougher the surface.

Another commonly used method is the *detrended fluctuation method*, sometimes called the *Bridge* method [56]. The method consists of calculating the standard deviation of the height h within bands of varying length l, and averaging over all the possible starting points of the bands

$$w(l) = \left\langle \big(h'(x) - \bar{h}'\big)^2 \right\rangle_L^{1/2}. \tag{1.75}$$

Before calculating the standard deviation, the linear trend between the first and the last point is subtracted for each band. Without subtracting a trend, the method is called the *variable bandwidth method*, a method which is numerically faster, but has been shown to give poorer results [57]. One usually limits the length of l to half the total profile length, because of the insufficient independent sampling for $l > L/2$. As for the second order correlation method, ζ can be estimated from the

scaling of w [53, 58]:

$$w \propto l^{\zeta} . \tag{1.76}$$

A third option is to calculate the height–height correlation function

$$C(r) = \left\langle (h(x) - \bar{h})(h(x+r) - \bar{h}) \right\rangle , \tag{1.77}$$

and take the Fourier transform. The Fourier transform is most easily calculated with an FFT-algorithm. As outlined by Feder [58], the power spectrum of C, $S(\omega)$, should then scale as

$$S(\omega) \propto \omega^{-(1+2\zeta)} . \tag{1.78}$$

Three computer-generated self-affine profiles are shown in Figure 1.27. How the roughness exponent characterizes the surface is seen from Equation (1.71). The surface is invariant to a change in length scales by a factor λ within the surface plane, as long as it is combined with a change of length scales by λ^{ζ} in the vertical direction. For physical systems, this is valid only in the scaling regime, which is bounded by upper and lower correlations lengths, ξ^{+} and ξ^{-}, in both the horizontal ($||$) and vertical ($\perp$) direction [48]. For the horizontal and vertical ranges, δr and δh, this means that the self-affine scaling is found over the range

$$\xi_{||}^{-} < \delta r < \xi_{||}^{+} \tag{1.79a}$$

$$\xi_{\perp}^{-} < \delta h < \xi_{\perp}^{+} . \tag{1.79b}$$

After the first years of roughness exponent calculations, it was believed that the exponent might be *universal* for all fracture modes and materials [49]. The values of ζ found in experimental studies of materials as different as graphite, porcelain and steel [54] were all $\zeta \approx 0.8$ [59]. Even though later experiments have proved the existence of a small-scale roughness exponent different from 0.8, the roughness exponent is still believed by some researchers to be universal for large scales. Lately, it has also been shown that some materials exhibit anisotropic self-affine properties, i.e. the roughness is not the same in both horizontal directions [59]. This is even expected to have commercial applications, in that it allows determination of the path followed by a crack, from the self-affine analysis of its fracture surfaces [60].

1.4.3 Fractures in soft materials

In order to support the concept of an universal roughness exponent, the experimental research on surface roughness has been conducted on a wide range of materials, including wood, steel, plaster, porcelain, polymer gels, etc. Most of the experi-

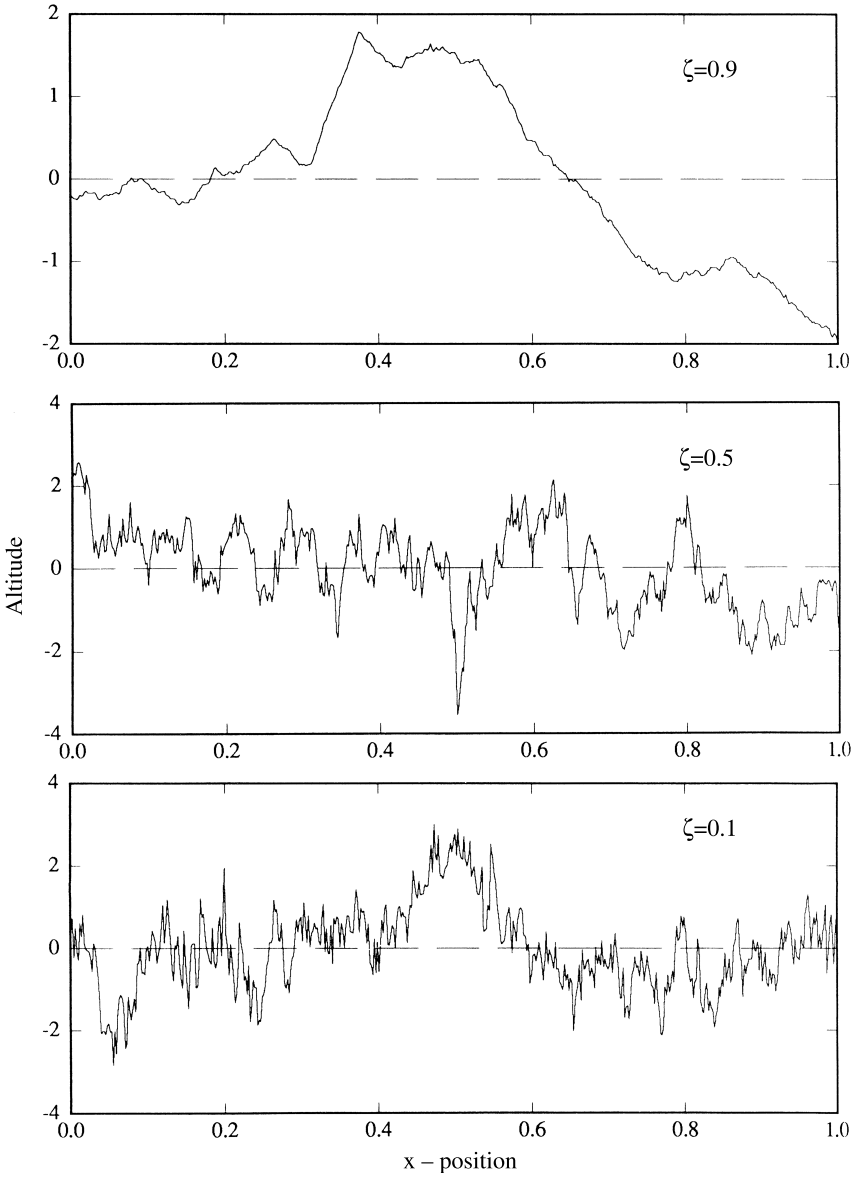

FIGURE 1.27: Illustration of self-affine profiles for three different values of ζ. Adapted from [58].

ments have been done on brittle materials. To our knowledge, no work has been done on fractures in materials directly comparable to the one utilized in this study. A study of polymer gels can be found in [61], but the gel is in that case brittle. Tanaka et al. [62] explain a brittle gel by pointing out that if a pair of fracture surfaces fit each other, it indicates that no plastic deformation takes place in the fracture of the gel. This is not the case for fractures in Laponite gels, so it is questionable whether the studies of polymer gels are comparable to our study.

Some of the distinguishing features between fractures in brittle and soft materials are discussed by Shull [63]. He points out that linear elasticity can not be used to describe the elastically deformed regions of soft, ductile materials. Linear elasticity is a common assumption of fractures in solid materials. While fracture properties in solid materials are essentially independent of the speed of deformations, the situation is different for most gels. Experimental evidence shows that fracture behaviour in gels depends markedly on the strain rate [64]. Furthermore, fracture is considered to occur when all bonds between the structural elements of a material in a certain macroscopic plane break. Normal materials are considered inhomogeneous in the sense that the breaks will start to develop in tiny cracks or weak spots. In colloid gels and composites, the weak spots are the boundaries of the aggregated particles in the fractal network, between which the cracks will move.

Tanaka et al. [62] point to another aspect of gels that makes the fracturing of them different from many of the normally studied materials. When a gel is suddenly stretched out of its equilibrium in a solvent bath, the gel will eventually absorb solvent to recover the dimension perpendicular to the direction of elongation, and the swelling ratio of the gel increases. Even without a solvent bath, a restructuring of the gel may occur if the crack growth is sufficiently slow. Then the region of the gel which is stretched during fracturing can absorb some solvent from the surrounding regions. The characteristic time of the permeation of solvent may therefore be a control factor in the fracture process.

Chapter 2

Experiment

2.1 Experimental setup

The MRI experiments were carried out at the Federal University of Pernambuco (UFPE) in Recife, Brazil, during a six months stay in the second half of 2007. A series of follow-up experiments were done by Eduardo Novais de Azevedo in March 2008, and the results from this session are also included.

2.1.1 MRI system

The MRI images were obtained with a $^{\text{UNITY}}$*INOVA* spectrometer manufactured by Varian Inc. The spectrometer includes a horizontal cryocooled superconducting small bore magnet made by Oxford Instruments. The magnet produces a magnetic field with magnitude 2.0 T, and the field has a high degree of stability and homogeneity, needed to obtain high quality MRI images. The magnet setup, including the attached cooling system, is shown in Figure 2.1.

The system also includes an RF coil, manufactured by Varian Inc., with internal diameter 6 cm and length 16 cm, see Figure 2.2. These are the absolute maximum dimensions of the samples that can be imaged with this system. In our case we would also like the samples to be smaller than this, in order to increase resolution and homogeneity of the magnetic field. The operating frequency of the system is 85.007 MHz, enabling the system to excite and record the signal from ^{1}H protons.

2.1.2 Sample holder

The initial intention of using the same sample holder as Nielsen [66] was quickly discarded during the pre-tests. It became clear that to achieve satisfactory resolution and signal-to-noise ratio, the gel samples would have to be imaged over several hours. A sample holder without walls could not keep the samples stable during the

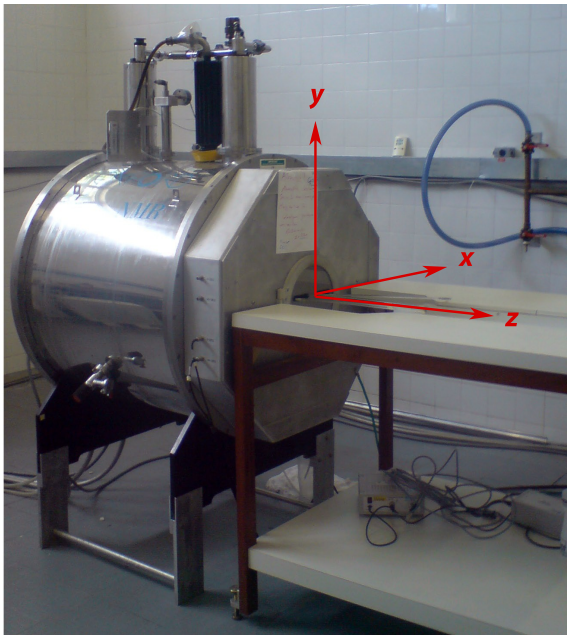

FIGURE 2.1: The Oxford MRI magnet with the attached cooling system visible on top. The gradient directions are shown in red.

FIGURE 2.2: The Varian RF coil. When installed in the machine, the cylindrical axis of the saddle-type coil is along the axial bore of the magnet, i.e. the z-direction of the system. Taken from [65].

entire scanning sessions, as they started to collapse under the force of gravity. The subsequent test using a printer cartridge container cut to fit within the RF coil, also made it clear that the gel needed to be kept in a closed environment. This was to minimize the evaporation and eventual fracturing of the gel during measurements.

The final solution was found after a search in various Brazilian department stores, and proved to be a container for paper clips. This container fulfilled all the requirements shown by the pre-tests: spatial dimensions suitable for the MRI apparatus, walls to keep the sample from dispersing, a lid too keep the water from evaporating, and a container made up by a plastic material. The plastic has relatively little proton mobility and no appreciable ^{1}H signal in the time scale of gel water FIDs, hence the plastic container is invisible to MRI.

Two modifications were made to the container. The first was to make a slit in one of the side walls, in order to facilitate an initial cut made to the sample. The second was to make an extra wall, to be inserted into the sample holder after fracturing the surface, in order to get equal sample lengths in both lateral directions. Because the MRI field of view needs to encompass all the material, and we wanted to image slices in both directions, the wall was inserted, and the excess gel removed. The dimensions of the sample holder are given in Figure 2.3.

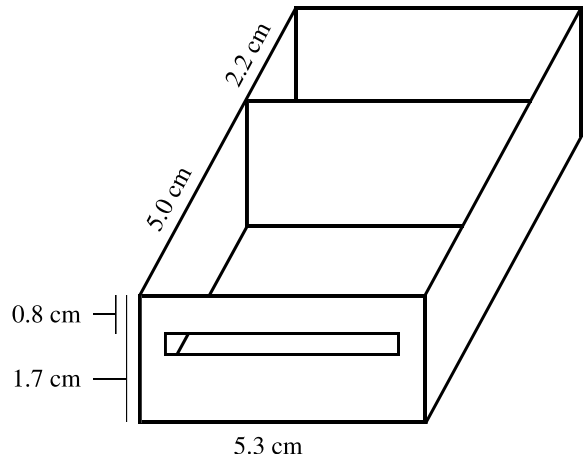

FIGURE 2.3: The dimensions of the gel sample holder.

After recommendations from Professor Ricardo Emmanuel de Souza, a different sample holder was made to test the resolution of the system and the profile extraction scripts. A matrix of holes approximately 0.8 mm in diameter and depth about 1 mm was made in the bottom of a small cylinder of Teflon. The holes were made with a needle in the workshop at UFPE, where a matching lid was also fitted.

For the roughness calculation test, a sample with known roughness exponent was borrowed from Professor Schmittbuhl in Strasbourg. The sample was a quad-

ratic block of silicone of approximate size 5×5 cm, and this size made it possible to use the same holder as for the Laponite imaging.

2.1.3 Stepping motor and load cell

To control the fracture velocity, a stepping motor 1331T006S from Faulhaber was used. This allowed precise control of the velocity from 1 to about 150 mm/min. A load cell, 1-PW4C3/300G-1 from HBM, was attached to the table of the stepping motor, and allowed force measurements. The maximum weight of the load cell was 300 g, well above the maximum load employed in the fracture experiments.

2.1.4 Software

A LabVIEW VI, written by Ole Tore Buset, was used to control the stepping motor, while another LabVIEW VI was written to read and record the signals from the load cell. The appurtenant software of the MRI-system, VnmrJ, was used to record images in the FDF format. The public domain image-processing program ImageJ, with a FDF plugin, was used to convert the images to pure text format. In the pure text format, an image is represented as a two-dimensional matrix, where the value of each element (i, j) represents the spin density at coordinates (i, j). The pure text images can be loaded into MATLAB, where all further analysis was performed.

2.2 Experimental method

2.2.1 Laponite gel samples

We used the purely synthetic Laponite clay, *Laponite RD*, purchased from Rockwood Additives Ltd. The Laponite gels were prepared according to the recommendations by the manufacturer [19]. We added 3 w/w % Laponite powder to deionized water at room temperature ($\sim$24 °C) with rapid agitation. The water was stirred in a beaker using a magnetic stirrer powerful enough to create a vortex in the water. The mixing was continued for 30 minutes after all visible aggregates had dissolved. During the mixing, the solution evolves from a white opaque, to a transparent water-like liquid.

Quickly after terminating the mixing, the Laponite–water solution was poured into the sample holders, where a scotch tape placed over the slit prevented the water from pouring out. The pre-tests showed that, at least to the eye, the Laponite samples were static over a long period of time when kept in a closed environment. The samples were therefore placed in air-tight containers while settling, and kept there together with a small cup of water until they were used. To store the samples in this fashion is important, because it ensures that the concentration of Laponite

remains constant. If kept at ambient conditions, the water will evaporate from the sample [66]. Note that we did not use the lids of the sample holders to seal the boxes before fracturing. The reason for this was that the lid had an edge that would come in contact with the still liquid solution, and destroy the otherwise flat surface. After fracturing though, this was no problem, both because the fracturing removes some gel, and because we are disregarding the edges.

After fracturing, the wall/separator was inserted into the sample holder in the part of the holder without slit, and the gel on the other side of the wall was removed, in order to reduce MRI-imaging artifacts.

2.2.2 Fracture

The experimental method for making fracture surfaces was based upon the *peel-test-like* method employed by Tanaka et al. [67], illustrated Figure 2.4. A filter paper was attached to the top of the gel by simply pressing it gently onto the surface, and letting the water enter the paper for about 20 minutes. When the filter paper was removed, a ca. 1 mm thick layer of Laponite stuck to the filter paper, and a fracture surface was left behind. On some samples, in order to facilitate the fracture, an initial cut of approximately 1 cm was made into the gel through the slit, a few millimeters below the filter paper. During the pre-tests however, this method of initiating the fracture was discarded. It was found that because the filter paper stuck so well to the gel, a fracture would appear even without the initial cut. The cut only increased the area along the edge unsuitable for analysis, thus giving less fracture surface to extract data from.

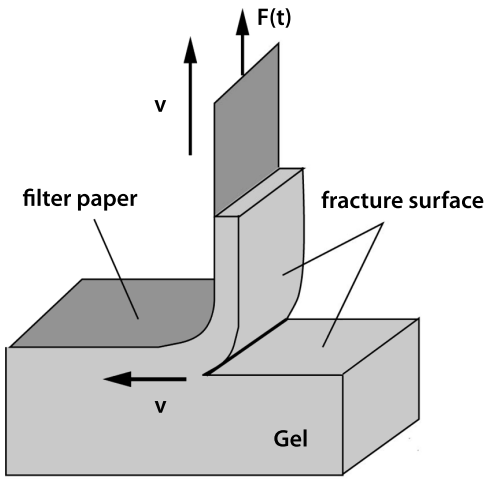

FIGURE 2.4: Fracturing the Laponite gel using a *peel-test-like* method. Figure adapted from [67].

The filter paper was attached to a load cell through a paper clip and a string. As the wet filter paper showed a tendency to break when pulled by the clip, an adhesive tape was put on one end of the paper, and the clip fastened through the tape. The load cell was mounted on the table of the stepping motor, and the stepping motor placed directly above the sample. To ensure that the paper is always pulled at right angles to the surface, causing a pure Mode I fracture, the motor was mounted at a 45° angle. In this way, the point where the pulling string is attached to the motor moves forward as well as upwards while the fracture is made.

During the fracturing, the pulling force was measured by the load cell. The speed of the stepping motor was easily controllable with LabVIEW. For the experimental sessions, we varied the fracturing velocity from 10 to 100 mm/min, in steps of 10 mm/min. The experimental setup is shown in Figure 2.5.

The output voltage from the load cell was recorded in LabVIEW using a NI USB-6210 DAQ card. Initially, the use of an amplifier before the DAQ card was attempted, in order to increase the digital resolution. This was however found to introduce too much noise on the signal, due to faulty power supplies. After extensive testing we failed to achieve a satisfactory signal-to-noise ratio, even after bypassing the amplifier and grounding the load cell body. The data from the load cell were therefore never used. Measurements of the same kind were however done simultaneously by Knut Magnus at NTNU. His treatment and results can be found in Magnus [68].

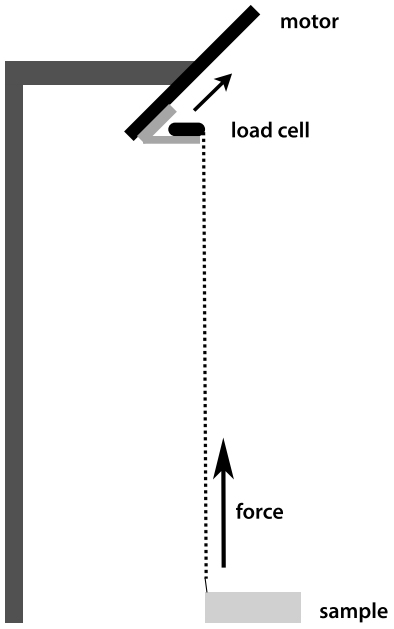

FIGURE 2.5: Illustration of the experimental setup. The load cell is mounted on top of the stepping table.

After the fracture surface was made and the wall inserted, the lid was placed on top of the sample holder, the slit and lid sealed with tape, and the sample was ready for imaging.

2.2.3 Imaging

Mounting the sample

The prepared sample, inside the sealed sample holder, was placed into the MRI system by the help of a styrofoam half-cylinder (see Figure 2.6). A small carving that fixed the sample holder on top of the cylinder had been made in the styrofoam, and this facilitated the adjustment and alignment of the sample in the magnetic field.

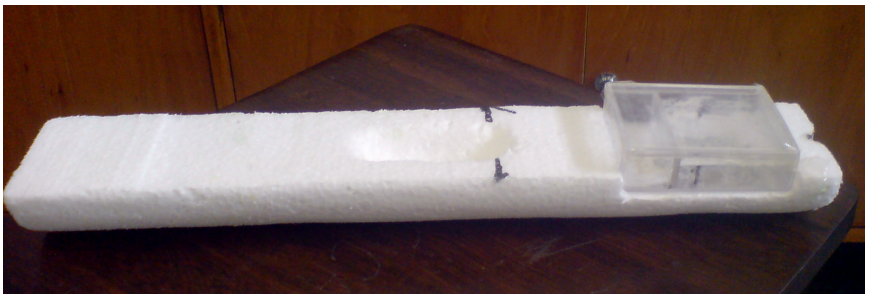

FIGURE 2.6: Image of the sample holder placed on the styrofoam half-cylinder used for insertion into the MRI system. Sample holder visible on the right.

Alignment of the sample is important for two reasons: It is primarily important that the sample is located in the centre of the coil, as this is where the magnetic field is most homogeneous. We also wanted the fracture surface to be as horizontal as possible, because this made the subsequent profile extraction in MATLAB easier. The centring in the magnetic field was done by setting the field of view in the imaging software, and extracting the sample profile in the z-direction. The sample profile is the integrated signal from the entire sample as a function of a chosen spatial coordinate. Hence, as the field of view is centred around the centre of the magnetic coil, it is easily seen from the sample profile whether the sample needs to be further inserted or retracted from the magnet centre. The horizontal alignment was done by taking coarse images of sample, and manually rotating the styrofoam cylinder in response to the images.

Determining T_1 and T_2

In order to determine proper scan parameters, the values of T_1 and T_2 for the gel samples were measured. T_1 was measured using the *inversion recovery* sequence, also known as *S2pul* [65]. In this sequence, the magnetization of the sample, initially in thermal equilibrium and located along the z-axis, is flipped into the negative z-direction by a 180° pulse. After a time τ, a 90° pulse is applied to turn the magnetization into the x–y plane. By varying τ, the value of T_1 can be calculated by recording the FID resulting from the 90° pulse (see Figure 2.7). To see the reason for this, remember that T_1 is the longitudinal relaxation time, and that the amplitude $S(\tau)$ of the measured FID at time τ after the 180° pulse is $S(\tau) \propto \big(1 - 2\exp(-\tau/T_1)\big)$. The magnitude of the measured FID is thus directly proportional to T_1.

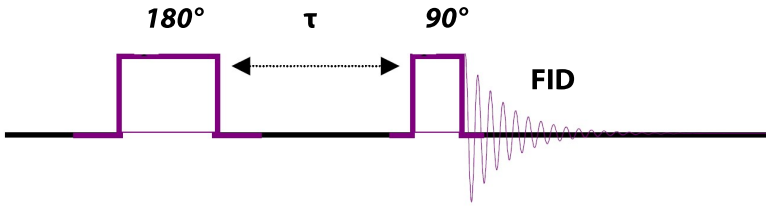

FIGURE 2.7: The inversion recovery pulse sequence used to measure T_1. Figure adapted from [65]

To measure T_2, the *CPMG* sequence was used. The sequence is named after Carr and Purcell who invented it in 1954, and after Meiboom and Gill, who modified it in 1958 [65]. In this sequence, a 90° pulse is applied to flip the magnetization into the x–y plane. As already discussed in the theory, Section 1.2.5, the transversal magnetization left to precess in the static magnetic field will decay with T_2^* due to the inhomogeneity of the magnet field. By applying a series of 180° pulses, the magnetization is refocused, and a measurement of T_2 is possible by recording the echo amplitudes. The modification introduced by Meiboom an Gill was to apply the 180° pulse along a direction orthogonal to the 90° pulse. This reduces possible errors due to accumulated phases from imperfect 180° pulses [65]. An illustration of the CMPG sequence is shown in Figure 2.8.

The measured values for T_1 and T_2 were 1700 ms and 140 ms respectively. This led us to choose the value of the repetition time, T_r, to be 6000 ms, and the echo time, T_E, to be as small as the software would allow us. The important thing about T_r is that it should be large enough to allow for a sufficient amount of magnetization to return to equilibrium before the next pulse sequence is applied. A value on the order of 3–4 times the value of T_1 is usually sufficient [65].

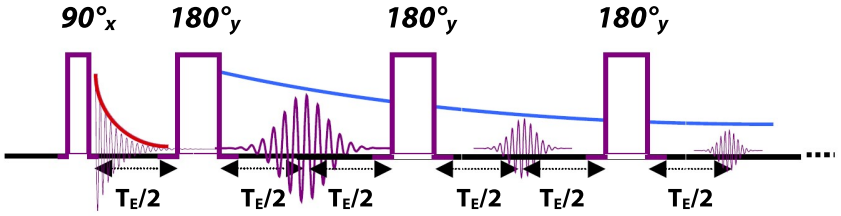

FIGURE 2.8: The CPMG pulse sequence used to measure T_2. The FIDs decay with T_2^*, indicated by a red line, while the echo amplitudes decay with T_2, indicated by the blue line. Figure adapted from [65].

Shimming

To reduce the linewidth of the signal, a *shimming* was performed. Shimming is the process of removing small inhomogeneities in the static magnetic field, and involves adjusting the magnetic field with an extra set of small coils placed outside the primary coil [41]. This method allows for easy adjustment of the homogeneity, should e.g. the surrounding structures have changed. It also makes it possible to adjust the field with respect to the sample being studied, which in it self may reduce homogeneity. The shimming was done automatically by software included by the MRI manufacturer, and typically reduced the line width of the recorded ^{1}H frequency from about 40 to 18 Hz.

Scan parameters

A final summary of the scan parameters can be found in Table 2.1. This represents the *normal* values for the parameters. During the experimental sessions, some of these parameters were varied. The variation was either due to testing, to see what values worked best, or because of coincidences, e.g. a total time of 12 h instead of 8 h because of the time left before refilling of liquid nitrogen. If a value different from the table value was used, and this had importance for the results, it will be noted in the text.

TABLE 2.1: A summary of the MRI scan parameters.

T_r	6000 ms	Matrix	256 x 256
T_E	14.8 ms	FOV	6 x 3 cm
Averages	20	Total time	∼8 h
Slices	20	Linewidth	∼18 Hz
Gap between slices	2 mm	Pulsewidth	4000 µs
Slice thickness	0.23 mm	Pulse shape	sinc

2.2.4 Test samples

We performed two tests, one to test the profile extraction and the resolution of the imaging, and one to test the validity of the calculated roughness exponents. In the following we will refer to the tests as the *resolution test* and the *roughness test* respectively. In contrast to the Laponite gel samples which are easily imaged with MRI due to the high water content, the teflon cylinder and the polymer sample used in these tests, give little or no signal. To image these, we therefore imaged not the sample itself, but water placed on top of it. In order for water to enter into the small pores of both samples, they were first placed over a beaker of boiling water. The idea behind this was that while liquid water will not wet the surface completely, vapour will have no problem entering the small pores. An image of the process is shown in Figure 2.9. How well this method works to completely wet the surface is unknown, but for our resolution it should be sufficient. As an extra guarantee, we pricked the holes of the resolution-test sample with a needle once the water was poured over the sample. Any large quantity of air left in the hole should then be pushed out and replaced with water as we retract the needle. On the roughness-test sample, there were no holes to prick, but we dragged a needle carefully over the surface, without noticing any air escaping.

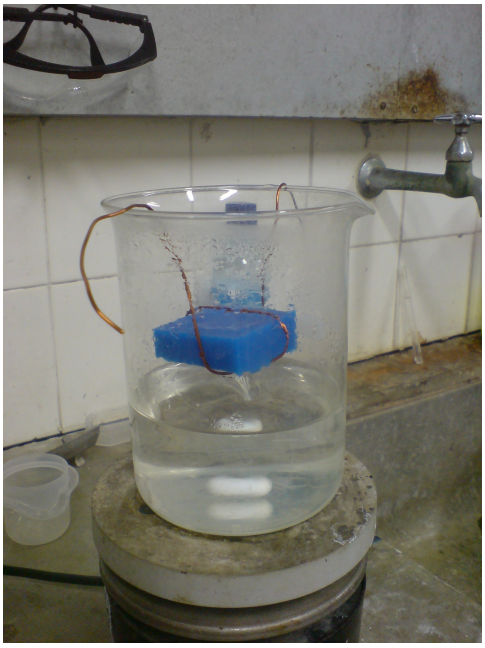

FIGURE 2.9: The resolution test sample placed over a beaker of boiling water.

For the resolution-test sample, we used the vapour method, poured water on top and secured the cylinder with the lid. For the roughness-test sample, we filled the sample holder with water, and immersed the sample in it, upside down, after first using the vapour method. The imaging parameters were largely the same as for the Laponite samples, as this was the experimental method we wanted to test. One exception is the 4.5×4.5 cm FOV in the resolution test, giving a resolution of 0.18 mm, as opposed to 0.12 mm for the Laponite imaging. The reason for the difference is that the resolution test was performed early in the experimental sessions, when 4.5×4.5 cm was the FOV we intended to use.

Chapter 3

Data analysis and discussion

3.1 Data acquisition and processing

3.1.1 Raw MRI images

We used the MRI setup to record the spin density within *slices* of the sample. Each slice had the same thickness, and the resolution within the slice was determined by the field of view and the size of the imaging matrix. As we wanted to calculate the roughness exponent both parallel and perpendicular to the direction of the fracturing, we recorded slices in both these directions. In MRI, a slice perpendicular to the z-axis is called *axial* or *transverse*, while a slice perpendicular to the x-axis is *sagittal* [41]. In this thesis we will for clarity refer to the direction along the fracturing as parallel, and the perpendicular direction in the surface plane as transversal. For all our images but one, we used a 256×256 imaging matrix. The field of view was mostly 6×3 mm, but was also varied a bit, to see if the results were resolution-dependent. For all the fracturing velocities considered, the matrix, FOV, and resulting resolution are shown in Table 3.1. A slice thickness of 0.23 mm was used for all images.

TABLE 3.1: The matrices and resolutions for all considered velocities.

velocity	imaging matrix	FOV	resolution
10 mm/min	256×256 mm	6×3.0 mm	0.23×0.12 mm
20 mm/min†	512×256 mm	6×3.0 mm	0.12×0.12 mm
50 mm/min	256×256 mm	6×2.6 mm	0.23×0.10 mm
70 mm/min	256×256 mm	6×3.0 mm	0.23×0.12 mm
90 mm/min	256×256 mm	6×3.0 mm	0.23×0.12 mm

†Imaged only in transversal direction

The images obtained by MRI were stored by the imaging software as a series of FDF files. Each FDF contained a header with scan parameters and the slice stored

as a 256 × 256 image matrix. Each pixel in the image contained a 32 bit value, representing the spin density recorded within that specific voxel. An example of the recorded images is shown in Figure 3.1.

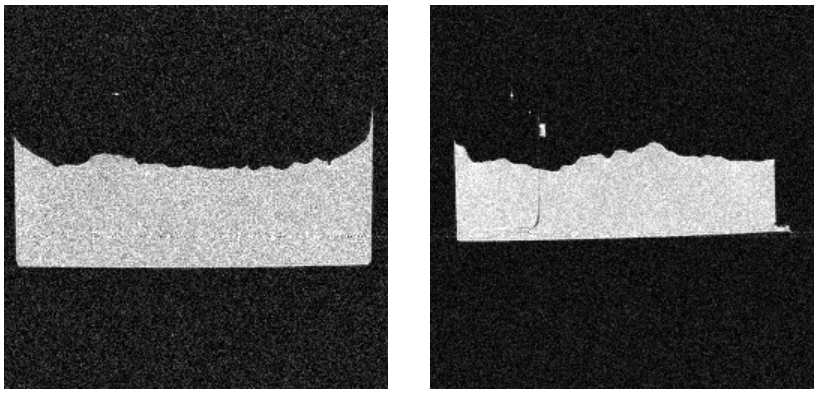

(a) Transversal (b) Parallel

FIGURE 3.1: Example of unprocessed MRI images. The clay samples are clearly visible in the centre of each image. The spin density is represented by the intensity of the image, where bright areas represent higher density. The surface of this particular sample was made with fracturing speed 90 mm/min. x-resolution is 0.23 mm, y-resolution is 0.12 mm.

The FDF files were converted to pure text images with the public domain image processing software ImageJ. The *Multi FDF Opener* plugin was used to load the images into ImageJ. The saved pure text images contains no header, but are easily opened in MATLAB.

3.1.2 Profile extraction

As the images in Figure 3.1 show, our MRI slices contain a lot of information that we strictly do not need. Because the principles behind MRI prevents us from imaging only the top part of the sample, the field of view encompasses the entire block of gel. The only thing that we are really interested in for further analysis is the surface profile, i.e. the coordinates of the sample–air interface. A MATLAB script was written to extract this from the images. The principles of the extraction will be explained here, whereas the whole source code is included in Appendix A.

Scaling

The pure text image is loaded into MATLAB and placed in a two-dimensional matrix. To be able to use the same script for different imaging schemes the image is first scaled. By different imaging schemes we mean e.g. averages, FOVs, imag-

ing matrices, etc. A variation in either of these parameters will result in changed signal-to-noise ratios. The scaling is done by subtracting the lowest pixel value from all the pixels, and multiplying by the inverse of a chosen typical signal value. By doing this, we know the pixels containing the gel sample have approximate value 1, while the noise is between 1 and and 0. The typical signal value is found rather heuristically by choosing the median of the tenth largest column values. This works because we know that more than half of the columns contain gel, and so the median will also be a gel-value. The reason for taking the tenth value instead of the largest is that the image may contain spikes, i.e. artifacts resulting in some pixel values being much higher than the real signal.

Profile

After the image has been scaled, we are ready to find the profile. The algorithm for this is simple. First we calculate a mean noise level from the all the pixels of the top five rows. We then set a threshold value to distinguish signal from noise, typically halfway between. For each column we move down from the top row, until a pixel with value higher than the threshold is found. If the next two pixels are also above the threshold, and no more than two of the next 15 are below, we have found the sample–air interface for this column. The reason for imposing the extra conditions for the following points, is again because of artifacts. We make sure that we have not encountered a spike above the surface, and take into consideration that some pixels within the sample may have artificially low values, e.g. due to minute air pockets.

The found surface profile naturally includes the empty areas on both sides of the sample. We therefore plot the profile, and use the plot to manually determine what part of the profile will be stored for further analysis. In choosing only a part of the profile, we also exclude points on each side of the sample, to reduce boundary effects. The final profile is stored to a file as a function of x and y. A pseudo code version of the profile extraction script is shown in Figure 3.2.

The profile extraction from the test samples was done in much the same way as for the Laponite samples, but especially regarding the roughness test sample, one difference is worth mentioning. The fact that we do not image the rough surface directly, but the water covering it, makes the extracted profile a mirror image of the real profile. This should not affect the roughness calculations – the surface is statistically the same – but for the sake of clarity, the profile is mirrored back to the real one. Also, the sample itself gives a small signal, see Figure 3.4, but this is to weak to affect the profile extraction.

```
load(image)
scale(image)
threshold=0.5(signal—noise)+noise
for x=1:xmax
    for y=ymax:1 && found=false
        larger =image(x,y)>threshold
        nexttwo=(image(x,y—1) && image(x,y—2))>threshold
        for i=1:15
            if(image(x,y—i)>threshold), next15=next15+1
        end
        if (larger=true && twonext=true && next15>13)
            profile(x,y)=(x,y)
            found=true
        end
    end
end
plot(profile)
save(profilepart)
```

FIGURE 3.2: Outline of the profile extraction script, in pseudo code.

3.2 Data analysis and results

3.2.1 Roughness exponent calculations

Because of the vast number of functions used in the literature to calculate the roughness exponent, and following the recommendation of Schmittbuhl et al. [56] and Bakke et al. [57], we used more than one method for calculating the exponent. The three we used were the detrended fluctuation analysis

$$w(l) = \left\langle \left(h'(x) - \bar{h}'\right)^2 \right\rangle_L^{1/2} \propto l^{\zeta} \ , \tag{3.1}$$

the second order correlation function

$$C_2(r) = \left\langle \left(h(x+r) - h(x)\right)^2 \right\rangle_x^{1/2} \propto r^{\zeta} \ , \tag{3.2}$$

and the Fourier transform of the height–height correlation function

$$\begin{aligned} C(r) &= \left\langle (h(x) - \bar{h})(h(x+r) - \bar{h}) \right\rangle \\ S(\omega) &= |\mathrm{Ftr}\, C(r)|^2 \propto \omega^{-(1+2\zeta)} \ . \end{aligned} \tag{3.3}$$

A more detailed description of the three different methods was given in Section 1.4.

A MATLAB script was written to calculate the functions above from the already extracted profiles. For all velocities and directions, the calculations were based on

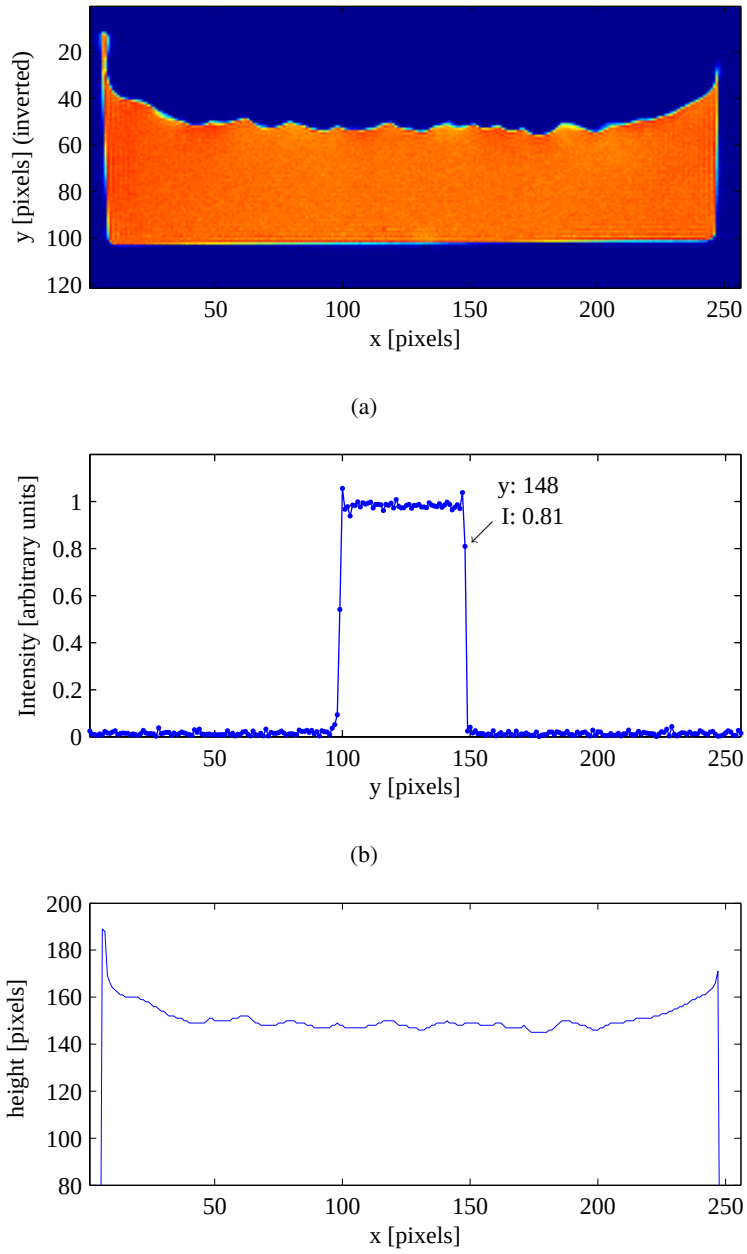

FIGURE 3.3: Profile extraction taken from a sample created with velocity 90 mm/min, transversal direction. **a)** A slice opened in MATLAB. **b)** Cross-section of the slice taken at $x = 150$. The arrow points to the profile coordinate chosen by the script for this particular cross-section. **c)** The entire extracted profile. Note that the contours on top of the sample in **a)** are clearly recognizable in the profile.

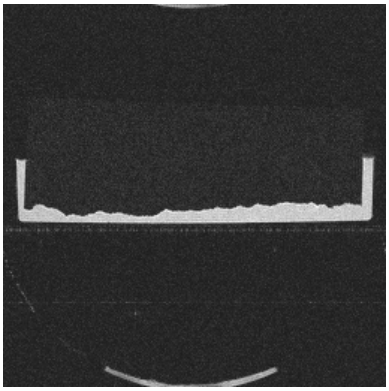

FIGURE 3.4: Example of an unprocessed MRI image of the silicone sample used for the roughness test. The spin density is represented by the intensity of the image, where bright areas represent higher density. The bright white area is water, while the arc near top/bottom is an artifact. The sample itself also give a weak signal and is visible upside down in the middle.

an average over all 20 slices. When calculating the exponent using the detrended fluctuation analysis and the second order correlation function methods, we averaged over all the slices before line fitting. When calculating the Fourier transform of the height–height correlation function, we averaged before taking the FFT.

Because all three methods scale as power laws, the exponent can be found by straight line fitting the data loglog. The canned line-fitting method in MATLAB unfortunately does not include error estimates of the line fits, so a line fitting script was written, based on the *fit*-routine in Numerical Recipes [69]. To fit the data, a suitable straight-line area of the plot needed to be chosen. This was done in the simplest way possible, by manual selection. The MATLAB script calculated the functions, plotted them in a loglog representation and paused for further input. The first and last x-axis value of the straight-line area was found by manual inspection, and given to the script. These values were then used to fit the data, and a new plot was made, including the fit. The script also stored the values of the fit for later plotting and analysis.

The calculated exponents for all considered velocities in both directions are shown in Figure 3.5, while examples of the straight line-fits are shown in Figure 3.6. As one can see from the plots in Figure 3.6, the fits are rather good over approximately one decade.

Resolution test

An unprocessed MRI image and the corresponding extracted profile for the resolution test are shown in Figure 3.7. The holes in the sample-holder filled with water

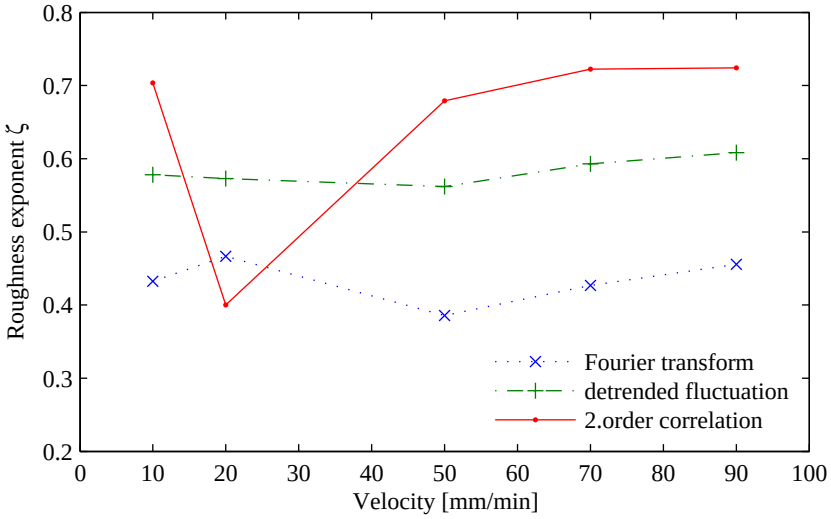

(a) Transversal direction

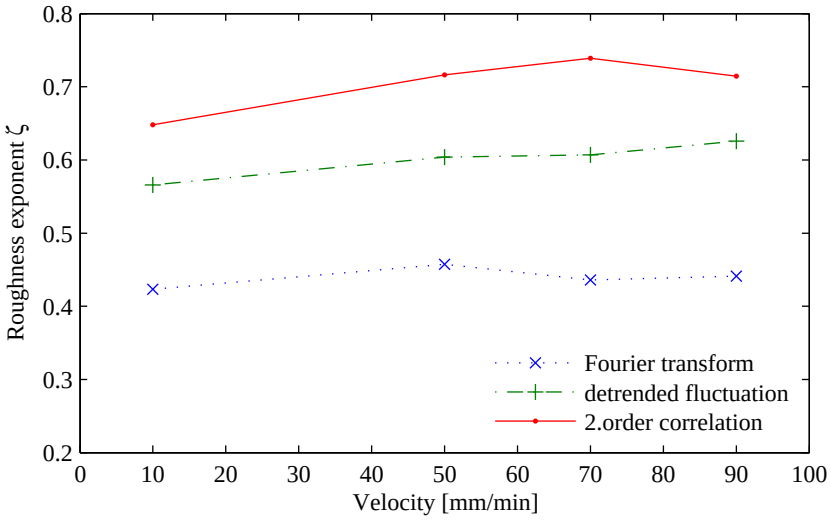

(b) Parallel direction

FIGURE 3.5: The roughness exponents for all velocities, calculated with the three methods presented in Equations (3.1), (3.2) and (3.3).

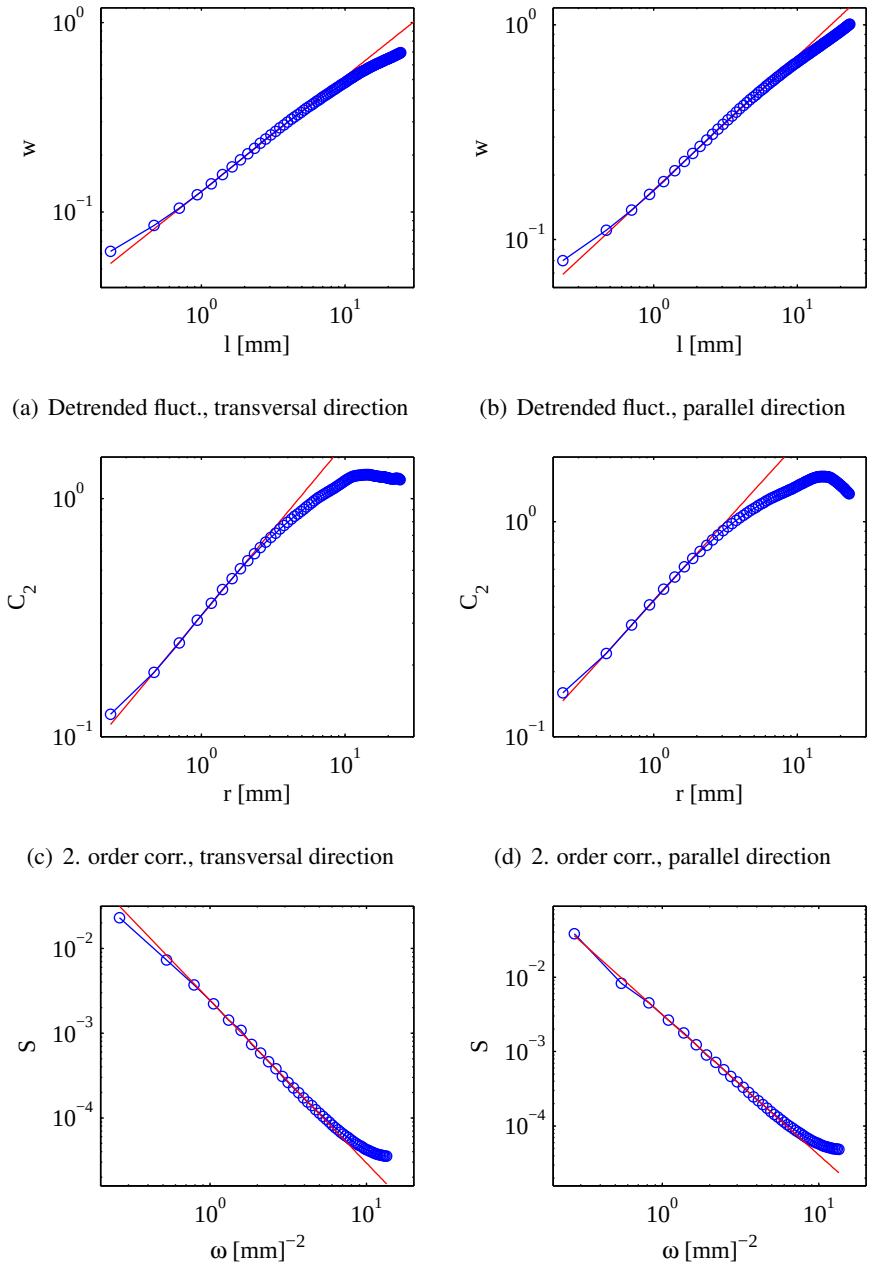

(a) Detrended fluct., transversal direction

(b) Detrended fluct., parallel direction

(c) 2. order corr., transversal direction

(d) 2. order corr., parallel direction

(e) Fourier transform, transversal direction

(f) Fourier transform, parallel direction

FIGURE 3.6: A representable selection of the straight-line fitted data, shown here for all three functions and both directions. The line fits are shown in red. These particular plots are for a fracturing velocity of 90 mm/min. The roughness exponents corresponding to the fits can be found in Figure 3.5.

are clearly visible in the MRI-image. Remember that it is the water placed in the sample holder that is being imaged, not the sample holder itself. In addition to the holes being visible on the image, the holes and their positions are also reflected in the profile extracted from the image.

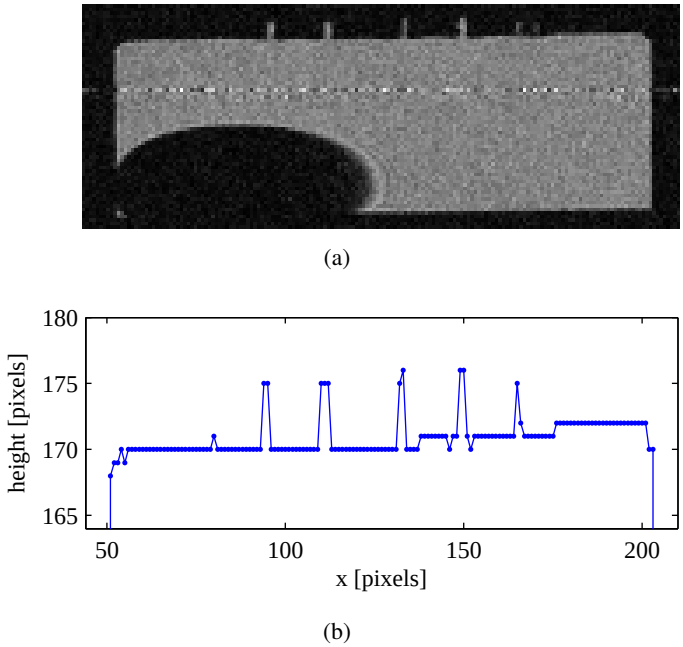

FIGURE 3.7: Representable **a)** FDF-MRI-image and **b)** extracted profile from the resolution test. The contours in the MRI-image are clearly visible in the profile. Note that the image in **a)** has been cropped and flipped vertically for clarity. The elliptical void at bottom left can thus be understood as an air bubble within the closed sample holder.

The reason why the distance between the holes on the image does not correspond to distances between holes in a regular matrix is easily understood from Figure 3.8. To see a whole row of 10 dots in one image, the sample would have to be perfectly aligned with the matrix. This would not have been straightforward to achieve, and was not necessary in order to test the resolution. What we wanted to see was a correspondence between the width and depth of the holes, and the number of pixel per hole on the extracted profile. As the width of the largest hole visible on the profile is $4\,\text{px} \times 0.18\,\text{mm} \approx 0.8\,\text{mm}$, and the depth/height is $5\,\text{px} \times 0.18\,\text{mm} \approx 1\,\text{mm}$, we conclude that the resolution set by the imaging-matrix and FOV is the resolution we achieve when extracting a profile. Note that it is natural that the holes are smaller at the bottom than at the top, because they were made by a needle.

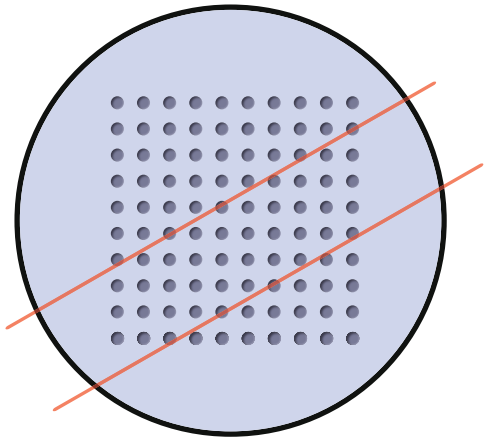

FIGURE 3.8: Schematic illustration of the extracted profile's dependence on the sample alignment. The red lines illustrate slices.

Roughness test

An unprocessed MRI image and corresponding profile for the roughness test are shown in Figure 3.9. The profile clearly reflects the surface as it is visible in the MRI-image. The part of the profile chosen for analysis is shown in Figure 3.9(c). When choosing the profile part, a portion of the edges have been discarded. As already noted, it is the water covering it, not the sample itself that is being imaged in this test. To actually get a proper representation of the surface, the profile should be flipped vertically. A plot of this is not included here, but one can see the result just by turning the page upside down. Of course, since the functions we use to calculate the roughness deal with correlations and standard deviations, the roughness is invariant to this transformation.

The calculated roughness functions and the corresponding line fits are shown in Figure 3.10. The roughness exponents resulting from the fits are given in Table 3.2. Just as for the Laponite samples, the fits are good over at approximately one decade. The value of the exponent resulting from the three different calculation methods differ significantly. This might be caused by the limited number of data points used for the analysis, and will be discussed further in Section 3.3.

TABLE 3.2: Calculated roughness exponents for the roughness test.

Detrended fluctuation	Second order correlation	Fourier transform
0.53	0.57	0.42

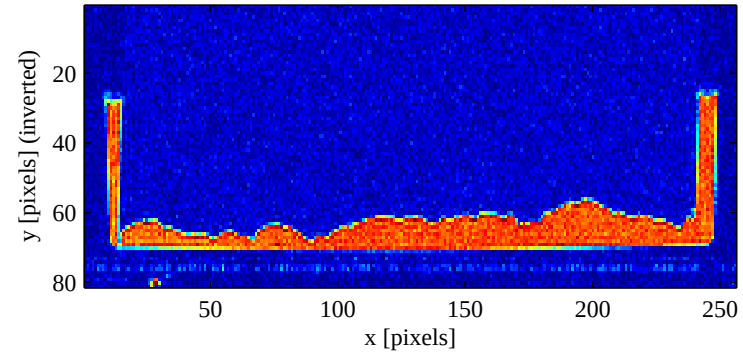

(a)

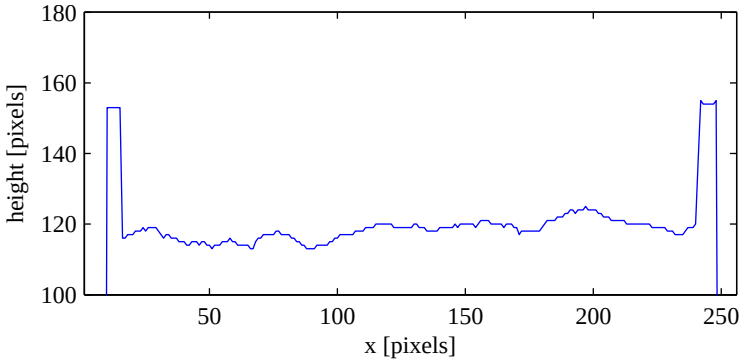

(b)

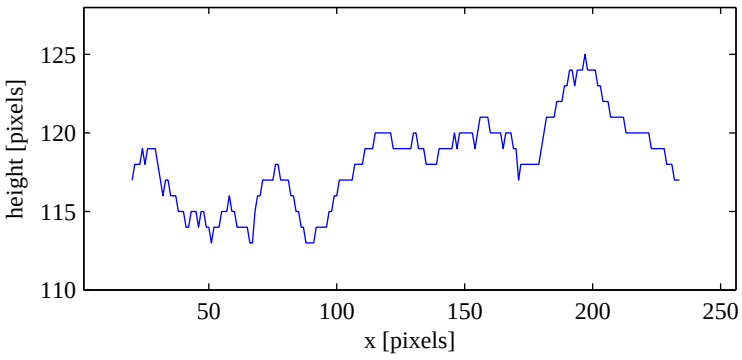

(c)

FIGURE 3.9: Representable image and extracted profile from the roughness test. **a)** MRI-image, **b)** extracted profile, **c)** the profile part chosen for analysis, with the height blown up for clarity. Note that the image in **a)** has been cropped and colored by MATLAB.

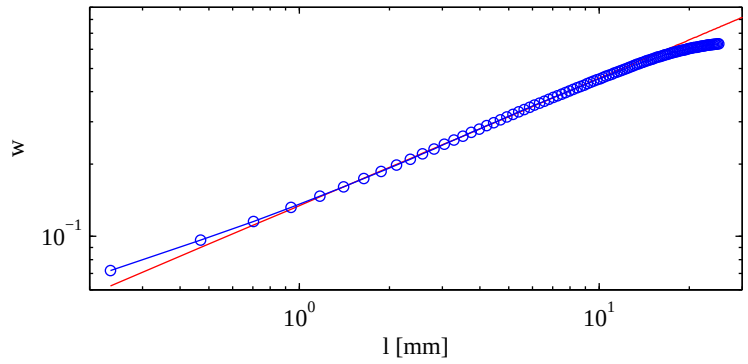

(a) The detrended fluctuation analysis

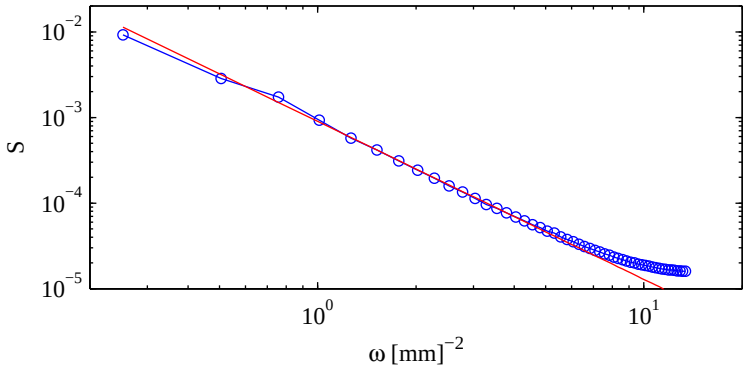

(b) Fourier transform of the height–height correlation function

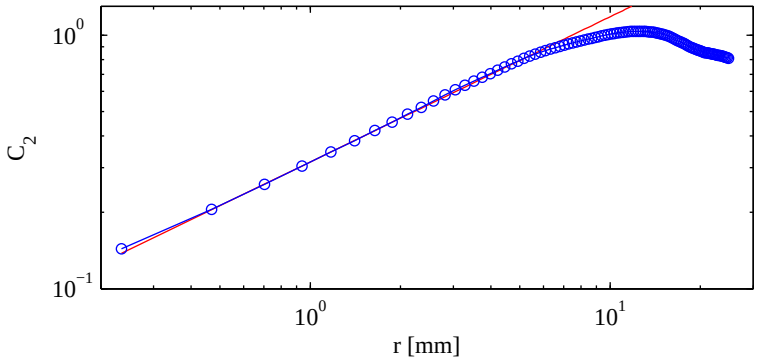

(c) Second order correlation function

FIGURE 3.10: Loglog plots of the three calculated roughness functions for the roughness test. The line fits are shown in red. The exponents corresponding to the fits can be found in Table 3.2.

3.3 Discussion

3.3.1 Validity of the roughness measurements

In the literature, Schmittbuhl et al. [56] and more recently Bakke et al. [57] have assessed the accuracy and reliability of the different methods of calculating the roughness exponent, by testing the methods against synthetically generated, "ideal", profiles. The synthetic profiles all have a well known, predetermined roughness exponent. With this method they can test the effects of both finite size and misorientation.

Finite-size effects

By considering the roughness exponent of the synthetically generated profiles as *true*, the differences between the computed *output* exponents and the true exponents can be measured. This was done for a number of profile lengths. The length most relevant for our experiment is 256 data points – slightly more than our profile after extraction, but close enough to be relevant. It is clear from both articles that none of the functions give the right output exponent for the entire considered range of $\zeta = [0.1,\ 0.9]$. In fact, for a system as limited as 256 points, a significant *intrinsic error* is reported.

For the Fourier transform method [56], the deviation $\zeta - \zeta_{\text{true}}$ grows almost linearly from about 0 at $\zeta_{\text{true}} = 0.1$ to approximately -0.08 at $\zeta_{\text{true}} = 0.5$. The deviation stays at about -0.08 from $\zeta_{\text{true}} = 0.5$ to $\zeta_{\text{true}} = 0.9$. On the whole, the method underestimates the value of ζ.

The detrended fluctuation method [57] has a rather large deviation of about 0.15 for $\zeta_{\text{true}} = 0.1$ but this decreases to less than ± 0.01 for $\zeta_{\text{true}} > 0.5$, except at $\zeta_{\text{true}} = 0.7$, where the deviation is almost -0.04.

The situation for the second order correlation function is different. Judging from the article Bakke et al. [57], this method is actually unsuited for analyzing profiles as short as 256 points. The intrinsic error for low ζ_{true} is more than 100 %, and it seems that the method is not even one-to-one. A measured ζ_{output}-value can correspond to a ζ_{true}-value both above and below ζ_{output}, making it all rather pointless. We therefore disregard all results obtained using this method.

Focusing only on the Fourier transform method and the detrended fluctuation method, the intrinsic errors reported above are very suitable for improving the exponents obtained from our roughness calculations. A MATLAB script was written that used linear interpolation to find the true exponent even when our measured ζ_{output}-values fell between those considered in the articles.

Misorientation

A linear drift superimposed on the signal might be difficult to avoid, simply because perfect alignment of the sample is hard to achieve. The effect of a misorientation on the detrended fluctuation method is a roughness exponent close to 1, for length scales larger than l_c:

$$l_c = s^{1/(\zeta-1)}\,, \tag{3.4}$$

where s is the slope of the ramp [56]. This should actually mean that our samples are sufficiently level, as we do not observe exponents close to 1. The effect on the Fourier transform method is a slope close to -2 ($\zeta = 0.5$). Although we have measured values of ζ close to this, we do not consider this to be an effect of the sample alignment, since the values resulting from the detrended fluctuation method are obviously unaffected.

Limited vertical resolution

Delaplace et al. [70] have studied the influence of the discrete description of an experimentally measured crack front path. Although the study of an in-plane crack font during its propagation is not the same as studying the rough surface left behind, the results should be transferable. The authors sampled the roughness fluctuations with a varying number of levels, and found that for high resolutions, the roughness was consistent from small to large length-scales. For low resolutions like ours though (~ 4 bits), the discrete sampling is a problem. In recent correspondence, Professor Schmittbuhl has expressed concerns about this [71]. Unfortunately, neither of his suggestions of increasing the system size or reducing pixel size are currently feasible with our setup. The rather low roughness exponent found in our study could therefore be a result of poor vertical resolution [70]. It is partly for this reason we conduct the roughness test. Without independent confirmations of our calculations, the problem of low resolution will continue to be an unresolved uncertainty.

3.3.2 Results with intrinsic errors subtracted

The results of our roughness calculations with the intrinsic errors subtracted are shown in Figure 3.11. An estimation of the uncertainties is also included in the figure. Finding a good estimate for the error bars is actually not straightforward – an apparent fact in almost all the literature on roughness calculations. In the pioneering days, when all exponents were 0.8 and the world seemed universal [49], the errors of the power law line fits were taken as the uncertainties. As the above discussion on intrinsic errors, finite-size effects and misorientation shows, that is

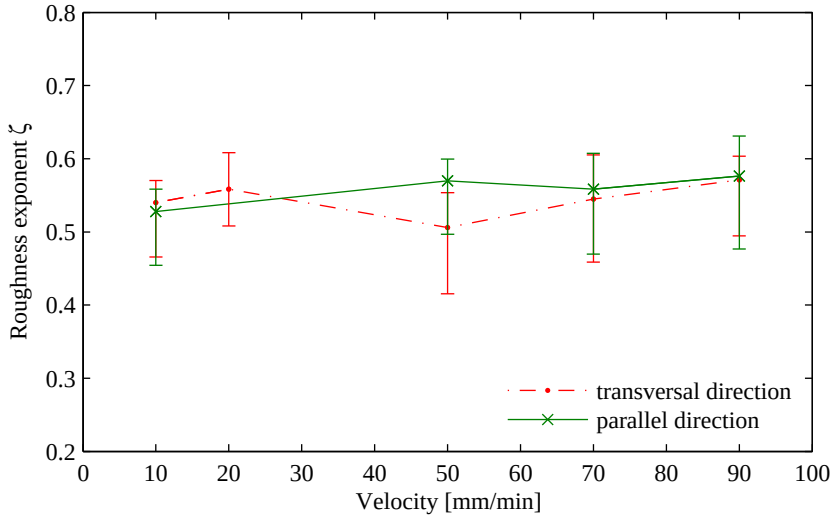

FIGURE 3.11: The calculated exponents with intrinsic errors removed. The error bars are the uncertainties found by Equation (3.5).

simply not adequate. This fact is also emphasized by Bakke et al. [57] and Schmittbuhl et al. [56].

What we have done is to estimate the uncertainty of the Fourier transform method to be ± 0.05. This is the maximum observed error-value for all ζ exponents and sample size 256 in Schmittbuhl et al. [56], and as such it should be quite conservative. For the detrended fluctuation analysis, we use the error of the line fit. In Figure 3.11 then, the data points are the mean of the two calculated values, while the error bars are the maximum error possible from the two methods:

$$\zeta_{\text{final}} = \frac{\zeta_{\text{ftr}} + \zeta_{\text{detr}}}{2} \pm \max, \min\left[(\zeta_{\text{ftr}} \pm \text{err}_{\text{ftr}}), (\zeta_{\text{detr}} \pm \text{err}_{\text{detr}})\right]. \qquad (3.5)$$

The results presented in Figure 3.11 are not exactly what we were hoping for, but a positive result nonetheless. The reason for creating fractures at different fracturing velocities was to discover the dependence of the roughness on the fracturing velocity, and our results show that there is none. Merging all the values – simply taking the average of all the means $\pm$ the average of all errors – we find the roughness exponent to be 0.56 (+0.05, -0.07), both parallel and perpendicular to the fracturing direction. The roughness created by fracturing velocities outside this range remains to be tested.

Roughness test

The results from the roughness test with intrinsic errors subtracted are shown in Table 3.3. Just as for the Laponite samples, we have discarded the value calculated with the second order correlation method. Some months after these data were calculated, we finally got Professor Schmittbuhl's own roughness measurement. As it turns out, to use this particular sample for the roughness test was not a very wise choice. The results sent to us by Professor Schmittbuhl, shown in Figure 3.12, are found by a profilometer that has a much higher resolution than our MRI-setup. The number of data points is also significantly larger, a 2062×2063 grid was used to calculate the roughness.

TABLE 3.3: Calculated roughness exponents for the roughness test, with intrinsic errors removed.

Detrended fluctuation	Fourier transform	Total
0.51	0.50	0.51 (+0.4, -0,6)

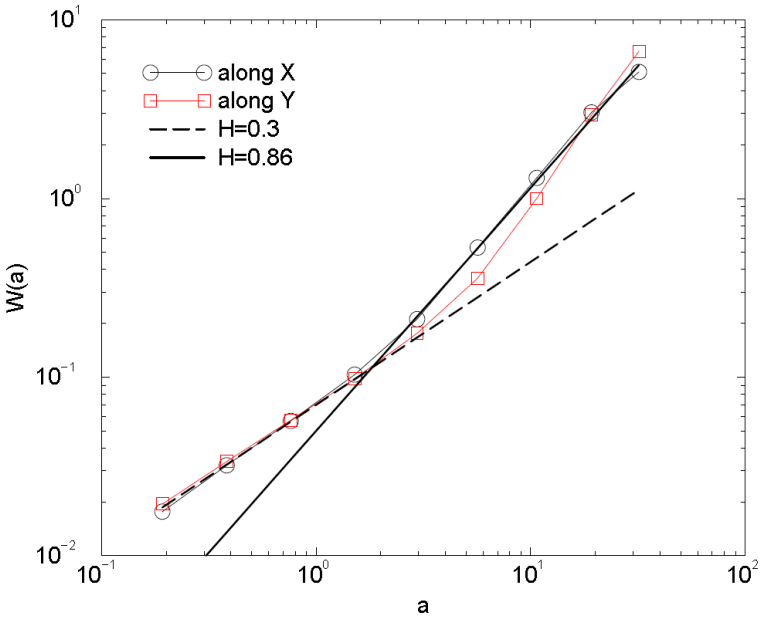

FIGURE 3.12: The roughness exponent for the roughness test calculated by Professor Schmittbuhl.

As one can observe in the figure, the measurement shows a crossover between two scaling regimes. A roughness exponent of 0.3 is found for distances smaller than approximately 1 mm, whereas 0.86 is found for distances larger than 1 cm. It is important to note that our measurements were performed along what Professor

Schmittbuhl has called the y-direction. In fact, this means that our measurements are done right on the crossover. Thus, while our result of $\zeta = 0.51$ is not explicitly confirmed by Professor Schmittbuhl, it is certainly not refuted either. An exponent of approximately 0.5 in the crossover between 0.3 and 0.8 seems reasonable. Further tests should however be carried out, and Professor Schmittbuhl has already agreed to lend us another sample, this time without a crossover.

3.3.3 Velocity dependent roughness from Mode-II fracturing

In what might seem contrary to the results presented above, we have actually observed a fracturing-speed dependent roughness as well. Recall from Section 2.2.2 that for the results already presented, the motor was mounted at a 45° angle, directly above the sample. A slightly different motor–sample setup was used during an initial experimental session, see Figure 3.13. In this setup, the motor was not tilted and the movement of the stepping table was therefore purely vertical. In addition, the sample was not placed directly below the sample, thus causing the paper to be pulled at an angle. The vertical distance between motor and sample was 2.3 m to keep the angle more or less constant during the pulling. Except for a FOV of 6×6 cm and a 265×256 imaging matrix, all imaging parameters were the same as for the experiments already presented. The change from this setup to the tilted motor setup was caused by a discussion with Knut Magnus at NTNU, who pointed out that neither the pulling speed, nor the pulling angle, are constant during the entire fracturing with the setup in Figure 3.13 [72].

The results for all velocities and both directions using this setup are presented in Figure 3.14, with intrinsic errors removed. As one can see, the results differ not only from the ones already presented, but also between the two directions. In the transversal direction the data indicate a linear relationship between fracturing speed and roughness, even though the uncertainties are quite large. By fitting the data to a straight line, we find the following relationship

$$\zeta_{\text{trans}} = 0.002v + 0.34\,, \tag{3.6}$$

where the velocity v is given in millimeters per minute. In the parallel direction, we cannot claim this kind of dependency. Here the roughness exponent seems more random.

We believe that an explanation for this kind of behaviour can be found by looking at the forces involved in the fracturing. As the filter paper is pulled at an angle, horizontal forces are present in this setup. If we recall the fracturing modes presented in Figure 1.26, we see that a fracture containing horizontal forces is no longer pure Mode I, but instead a combination of Mode-I and Mode-II. With in-

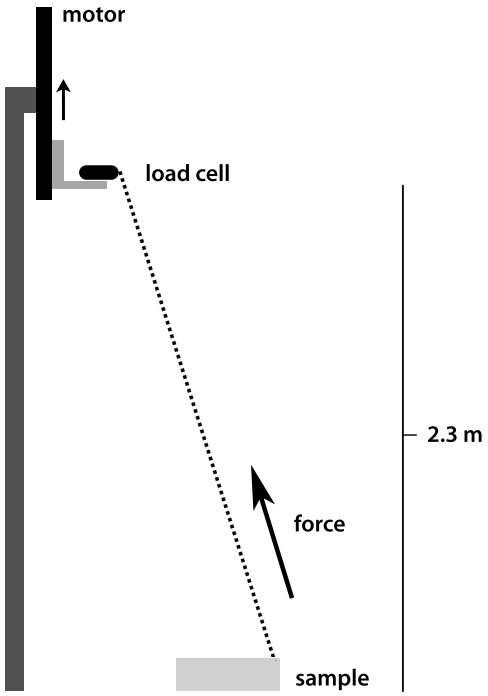

FIGURE 3.13: The motor–sample setup used during the initial experimental session.

plane shear we think it is reasonable to expect some kind of stretching and releasing during the fracture, which could result in a transport, i.e. some gel that sticks to the filter paper will be deposited at intervals along the fracturing direction. We expect this to create a large-scale roughness, or bumps, and evidence of this can actually be seen on some of the MRI-images, see Figure 3.15. We can regard the bumps as a superimposed large scale roughness on top of the pure Mode-I roughness, and this alters the total exponent.

The roughness in the transversal direction should be invariant to the large-scale roughness, at least as long as the bumps extend over the whole transverse. Whether the slice is recorded on the top of a bump or in the bottom of a depression only alters the reference height of the surface, a value which is irrelevant for ζ. It is our impression, both from looking at the fracture surfaces and the resulting exponents, that the bumps are created rather haphazardly. One could imagine them being dependent on local density variations in the gel, whether the gel sticks to the walls of the sample holder, small deviations from the correct pulling angle, etc. This explains why the parallel roughness is rather random.

We believe the dependence of the transversal roughness on the fracturing velocity to be another result of the Mode-II fracturing. In addition to creating bumps in the parallel direction, the in-plane shear introduces velocity-dependent transver-

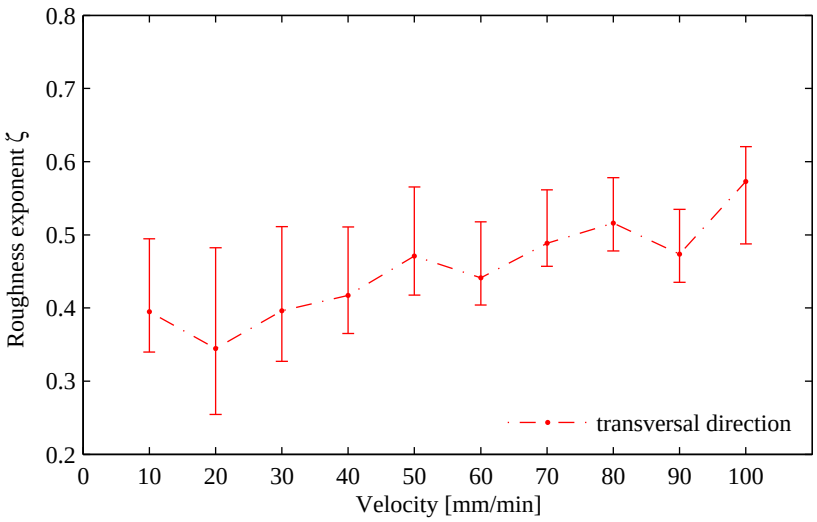

(a) Transversal direction

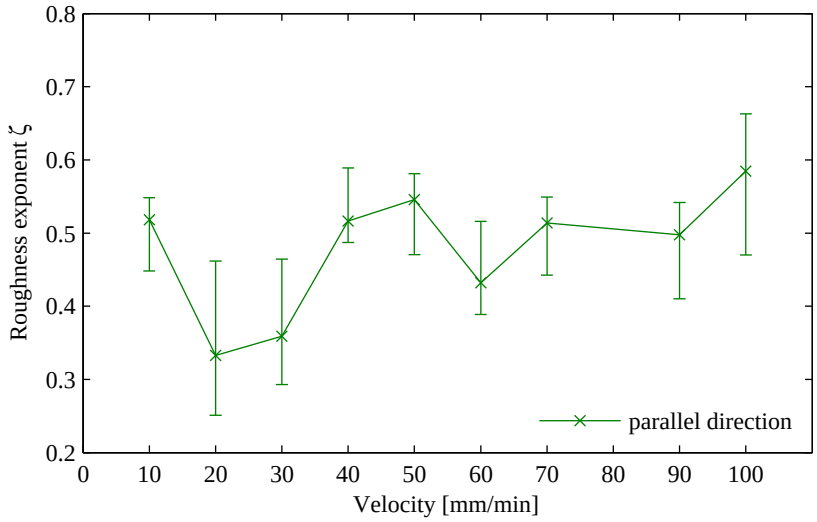

(b) Parallel direction

FIGURE 3.14: The results from the alternative motor–sample setup.

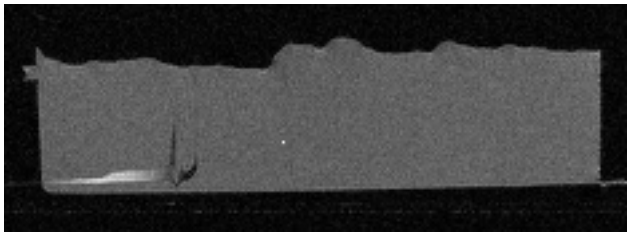

FIGURE 3.15: Large scale roughness in the parallel direction due to Mode-II fracturing. The fracturing velocity for this particular sample was 90 mm/min.

sal roughness. Unfortunately, we have not been able to find any good references explaining this behaviour. There seems to be few studies of mixed-mode fractures in the literature, due to the increased complexity of the fracture mechanisms with such setups. Some experiments have been done on solid materials – e.g. Lung et al. [73] who found that Mode-I fractures results in self-affine surfaces while Mode-III causes self similarity – but none that are applicable to our kind of system.

If we were to attempt a qualitative explanation, it is tempting to consider the *persistence* of the gel. In Physics and Fractal Structures [74], Jean-François Goyet explains the meaning of ζ larger or smaller than 1/2. For $\zeta > 1/2$ it is most probable that any given step in a height profile will go in the same direction as the previous step. A surface with this property is said to be *persistent*. The situation is opposite for $\zeta < 1/2$, where the steps have highest probability of going the opposite way as the previous step. This kind of behaviour is called *antipersistency*.

Looking at Figure 3.14(a) we see that the roughness of the Laponite surface goes from being antipersistent at low velocities to persistent at high velocities. We believe that it is not unlikely for the clay gel to possess properties that are suppressed at high pulling speeds, but that leads to antipersistency when the velocity is low. A coupling to the shear thinning behaviour previously reported for Laponite suspension [75] seems obvious. In fact, just by considering the shear-thinning itself, a velocity-dependent roughness makes sense, as we would expect the roughness to decrease with decreasing viscosity.

More work, both experimentally and theoretically, is needed before a full understanding can be reached. At the moment, however, a more detailed explanation than the one outlined above is beyond the scope of this thesis.

Chapter 4

Concluding remarks

In this experiment we performed Magnetic Resonance Imaging experiments on fracture surfaces of Laponite gels. The gels were formed by adding 3 w/w % free flowing Laponite powder to de-ionized water, and letting the gel settle for more than 24 hours. The fracture surfaces were created by the controlled removal of a filter paper attached to the gel surface. We used the MRI equipment to image slices in both lateral directions, and a MATLAB script was written to extract the profile of the sample–air interface.

Fracture surfaces were created with fracturing speeds in the range between 10 and 100 millimeters per minute. Using a fracturing setup ensuring a pure Mode-I fracture, we observed no dependence between fracturing speed and roughness. The roughness exponent ζ was calculated using both a spectral and a correlational method, and was found to be 0.56 $(+0.05, -0.07)$ in the entire velocity-range studied.

We also imaged the fracture surface of a silicone sample whose roughness exponent had already been measured by a profilometer. The profilometer measurements revealed a crossover between a small scale exponent $\zeta = 0.3$ and a large scale exponent $\zeta = 0.86$. Our measurements were done on length scales that coincides with the crossover, and the measured value of 0.51 (+0.4, -0.6) is therefore reasonable. Measurements on another sample should still be made to better assess the validity of the rest of our work. Should the new measurements disagree with results from proven methods, all our results are questionable.

Imaging surfaces that were made by a combination of Mode-I and Mode-II fracturing, we found a linear dependence between fracturing velocity and the roughness exponent, in the transversal direction. A line fit resulted in the following dependency: $\zeta_{\text{trans}} = 0.002v + 0.34$, where the velocity is millimeters per minute. In the parallel direction, a large scale roughness distorts the surface, making us unable to find any dependency. We attributed the transversal roughness to

the in-plane shear of the Mode-II fracture, and outlined an explanation where the velocity-dependency is due to properties of the clay gel that are not yet fully understood. We particularly believe the shear-thinning behaviour of Laponite dispersions to be important.

To our knowledge, this is the first time the roughness exponent has been found for fractures in clay gels. Both the gel's low viscosity and its transparency means that traditional methods such as profilometry and AFM are unsuitable. Although the Hurst exponent has previously been found from MRI images in texture analysis [76], we also believe this is the first time MRI has been used to find the roughness of self-affine fracture surfaces.

Future experiments should focus primarily on three things: First, it is paramount that another roughness test sample is imaged, preferably one that does not have a crossover in the imaging range. The roughness measured will hopefully be the same as the one found with other methods. Second, the soundness of our results should be investigated by other tests. Our assumption that the gel samples are stable during the imaging period, can easily be tested by taking two or more images back to back. If the second image – or rather the roughness calculated from it – is significantly different from the first, our assumption is wrong and the results questionable.

Third, more measurements on the same system should also be made, provided the tests described above are positive. The velocity range should be expanded both upwards and downwards, and new measurements in the same range are also desirable. The reason for the limited number of measurements with the Mode-I setup presented in the previous chapter, was that we performed extensive measurements and testing on the other setup before realizing its drawbacks. Completing the 10 to 100 mm/min range with the Mode-I setup should be a minimum. Also, some test with other Laponite concentrations were previously done without giving satisfactory results. Redoing this would be interesting, as we believe the surfaces should be rougher with increasing concentrations.

NOTE ADDED IN PROOF: We have recently been made aware by Professor Schmittbuhl that the results presented in Figure 3.12 are uncorrect. Because the label on the silicone sample had worn away, the sample got mixed up with a another, and the results are *not* the correct ζ for our roughness test sample. Although the sample is similar to the one we used, we are at the moment unsure how well the results in Figure 3.12 translates to our sample. Unless the correct profilometer data are in agreement with those in Figure 3.12, the discussion about crossovers in the previous chapter might be disregarded. If anything, this confusion only strengthens the urge above; Another roughness test sample should be imaged.

Part II

A synchrotron WAXS study of ordering in NaFh dispersions

Chapter 5

Theory

5.1 Synchrotrons

Short introduction

In the course of the more than 40 years [77] synchrotron radiation has been used, it has evolved tremendously. A study in 2004 [78] estimated that about 40000 scientists use synchrotron radiation very often in an interdisciplinary approach to study fields as diverse as interface physics, magnetism, absorption, scattering, structural biology and more. Originally seen as an unwanted byproduct of high energy particle accelerators [79], there are now (2007) roughly 50 synchrotron light sources around the world [80]. After the first generation of synchrotrons – so-called parasites on high energy machines – the first facilities dedicated only to synchrotron radiation were built around 1980. The synchrotrons of today, however, belong to the third generation, and utilize injection devices and more powerful magnets to generate highly specialized, high brilliance synchrotron light. This, and other aspects of a synchrotron, will be discussed in the sections below.

5.1.1 Synchrotron radiation

Synchrotron radiation is the electromagnetic radiation emitted by relativistic, charged particles traveling in a curved path. All charged particles emit electromagnetic radiation when they accelerate, but there are a few things that separate synchrotron radiation from the radiation generated in e.g. an antenna. In synchrotron facilities, the charged particles – usually electrons – emit radiation when powerful magnets deflect them from their paths.

A moving charge in a static magnetic field is subject to the well known Lorentz force

$$\boldsymbol{F} = e\boldsymbol{v} \times \boldsymbol{B} \,, \tag{5.1}$$

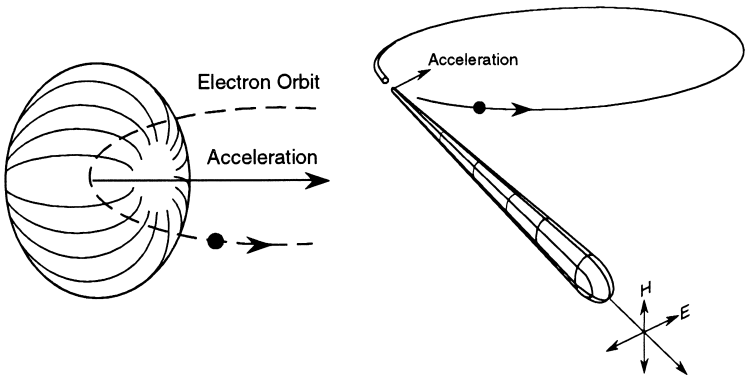

(a) $\frac{v}{c} \ll 1$ (b) $\frac{v}{c} \approx 1$

FIGURE 5.1: Emission spectrum from **a)** classical and **b)** relativistic electrons. Note that **b)** is as viewed from the laboratory frame, not the electron frame. Adapted from [82].

where the cross product means that the particle is accelerated perpendicular to both the magnetic field and the particle's direction of motion. This is contrary to the radio antenna, where the acceleration is parallel to the electric field imposed on the antenna. Furthermore, synchrotron facilities always use relativistic particles as radiation emitters because of how the energy flux is emitted at relativistic energies. For relativistic particles, the velocity is close to the speed of light, $v \approx c$, and the kinetic energy is high compared to the rest mass energy, i.e. $E = \gamma mc^2$ with $\gamma \gg 1$. Because of the relativistic space-time Lorentz transformations [81], the radiation pattern becomes sharply focused in the direction of motion of the radiating charge. This is illustrated in Figure 5.1. The opening angle of the radiated cone is given by $1/\gamma$, and this results in an opening angle of only 0.001 radians for electrons with energy of 511 MeV [82].

5.1.2 Storage rings

Most facilities that utilize synchrotron radiation are based upon a storage ring. A storage ring is an arrangement of components that enables the relativistic particles to circulate in a closed orbit for several hours without significant loss of intensity. Along the curved parts of the ring, synchrotron radiation is emitted and can be used for research. The storage ring has several advantages, most importantly that it saves energy by not having to continually accelerate particles to near light speed velocities.

Modern synchrotron facilities typically accelerate the particles in components separate from the storage ring. One of the main advantages of this is when the

particle current needs refilling, or the beam goes down, the refilling takes shorter time. A common setup is to use a combination of a linear accelerator, *linac*, and a booster synchrotron to accelerate the particles [82]. The linac accelerates the electrons in a linear path in high electric fields, and the resulting current is injected into the booster synchrotron. In the booster, the electrons continue to be accelerated for each revolution, and are kept in orbit by increasing magnetic fields in the bender magnets. When the electrons are ready to be injected, fast switching magnets in the booster changes the trajectory of the current and deflects it into the storage ring. A linac–booster–storage ring setup is shown in Figure 5.2.

Because they radiate, the electrons lose energy and speed as they move around the storage ring. The energy lost per turn has to be restored by using a radio frequency electric field. The RF field's frequency is a harmonic of order k of the revolution frequency of the particles [81]:

$$\omega_{RF} \propto k \times \frac{2\pi c}{L_0}\,, \tag{5.2}$$

where L_0 is the length of the orbit. The RF voltage is designed so that a particle arriving a bit before the ideal time will receive less energy than a particle arriving a bit to late. This means that a properly tuned RF field will stabilize the energy of the particles and pack them together into what is known as *bunches*. The nominal energy E of a bunch is called the *synchronous energy*. Storage rings can be loaded with anywhere from one to a thousand bunches, distributed uniformly or anisotropically around the ring.

Injection devices

Todays third-generation synchrotrons differ significantly from the earlier versions, where the radiation came from bending magnet radiation only. The synchrotron-shape is now generally polygon instead of circular, and at every corner of the polygon, the magnet is bent from one straight section into another. One or more of the straight sections must contain the radio frequency cavities where the electron bunches are focused and accelerated, but the rest usually contains *wigglers* or *undulators*, collectively termed as injection devices. An illustration can be found in Figure 5.3. Injection devices consist of a linear array of north–south magnetic dipoles of alternating polarity [77]. Because the electrons feel an alternating change in magnetic direction as they move through the array, they are rapidly being deflected inwards and outwards and undergo a nearly sinusoidal trajectory.

The reason for installing injection devices is both to alter the properties of the emitted radiation, and to increase the intensity. In a standard bending magnet design, the emitted radiation is spread out like the light from a well focused

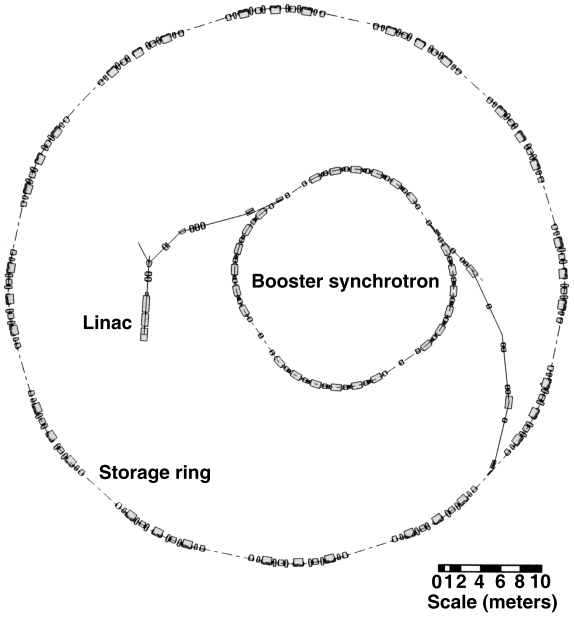

FIGURE 5.2: Schematic illustration of the Advanced Light Source synchrotron at Berkeley. The relativistic electrons in the synchrotron are first accelerated by the linac and booster synchrotron, before being injected into the storage ring. Adapted from [77].

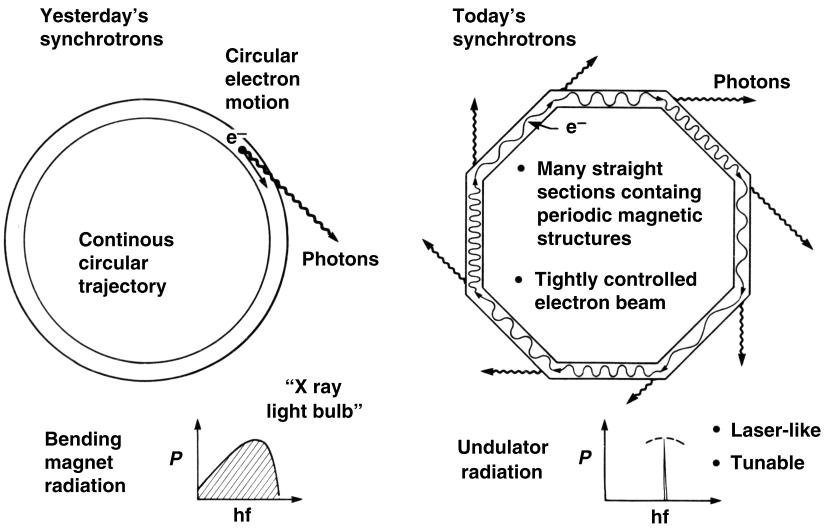

FIGURE 5.3: The evolution of synchrotron facilities. **a)** Early synchrotrons used mainly bending magnets, whereas **b)** today, the bending magnets are supplemented with injection devices. Adapted from [77].

lighthouse, and contains a continuum of frequencies determined by the radius of curvature and the speed of the particles. If τ is the duration of the pulse from one passing particle, the pulse contains frequencies up to a critical frequency given by [81]

$$\omega_c = \tau^{-1} = \frac{3c\gamma^3}{2r}. \tag{5.3}$$

In an injection device, because the particles are being accelerated back and forth, the flux and brightness of the radiation is enhanced by a factor approximately equal to the number of poles [82]. The difference between a wiggler and an undulator is the degree of deflection the electrons undergo as they pass the device, shown in Figure 5.4.

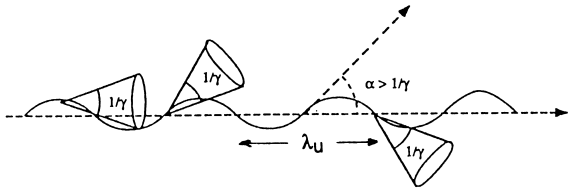

(a) Wiggler

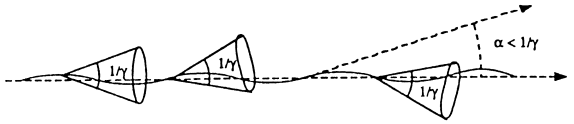

(b) Undulator

FIGURE 5.4: The difference between a wiggler and an undulator. Adapted from [81].

In a wiggler, the maximum deflection α is larger than the opening angle of the radiation cone, $1/\gamma$. This means that an observer in the forward direction receives more pulses of approximately the same duration as from a bending magnet, but because the pulses are separated in time, they are are not able to interfere. In the undulator regime, the angular deviations of the trajectory is smaller than, or close to, the photon emission angle, i.e. $\alpha \lesssim 1/\gamma$. The amplitudes of the field radiated at each period of the trajectory are thus added coherently, and may interfere. This interference results in a spectrum that is enhanced at certain wavelengths, in contrast to the continuous spectrum produced in bending magnets and wigglers. More specifically, the undulator radiation spectrum consists of a fundamental, and several harmonics. The photon energy ε_n of the nth harmonic is

$$\varepsilon_n[\text{keV}] = \frac{0.949 n E^2[\text{GeV}]}{\lambda_u[\text{cm}]}\left(\frac{1}{1 + K^2/2 + \gamma^2\theta^2}\right), \tag{5.4}$$

where λ_u is explained in Figure 5.4, K is given by α/γ, and θ is the angle of emission relative to the undulator axis [77]. In practice, this means that a synchrotron experimenter is able to tune and select the photon energy of the undulator light to match his experiment. The value of K is dependent on the magnetic field of the undulator dipoles, and is most easily tuned by changing the undulator gap. For $K \ll 1$, the only significant photon flux is the fundamental, thus giving a sharp quasi-monochromatic radiation in the forward direction [77].

It is common that synchrotron radiation is highly polarized. For bending magnets the polarization is dependent on the angle of emission, while for the radiation emitted from undulators and wigglers, the polarization is in the plane of the orbit [82].

Beam decay

The electron beam in a storage ring always loses intensity with time, a concept which is known as *beam decay*. There are several reasons for this decay, and some are unavoidable consequences from the ring designs. As the electrons emit radiation, some of the radiation will unavoidably hit the chamber walls, and this creates positive ions in the chamber. The negative electrons may interact with the ions, leading to beam decay. Furthermore, even if the interactions do not lead to decay, they may also decrease stability and increase the extent of the electron bunch. To minimize decay, and increase the lifetime for the stored current, a high vacuum on the order of 1×10^{10} Torr within the chamber is desirable [81].

5.2 X-ray diffraction

Short introduction

X-ray diffraction is a powerful tool used to probe the structure of matter. Ever since its discovery by Max von Laue in 1912 [83], the range of problems where X-rays have proved to be decisive in unraveling the structure of a given material has grown to staggering proportions [84]. Among the fields that utilize X-ray diffraction, we find materials science, surface and interface science, structural biology and soft condensed matter [85]. With the introduction of synchrotron X-ray sources, particularly of the third generation (see Section 5.1), the pace of innovation in X-ray science has increased markedly.

5.2.1 Diffraction

Diffraction is a very common phenomenon that manifests itself in our daily lives, for example as the rainbow on the surface of a compact disc, or as the vivid colors

on an oily puddle of water. We will here deal with diffraction from X-rays, but diffraction is in itself a phenomenon that may occur for all wavelengths of light, and even other kind of waves. The essential condition for diffraction is that the distance between scattering centres must be about the same as the wavelength of the waves being scattered [86]. What makes X-ray diffraction particularly interesting, is that the wavelength of X-rays is about 10^{-10} m (1 Å). This is the same order of magnitude as the structural spacings of crystals, which makes X-rays suitable for crystallographic structure determination.

The Laue formulation of diffraction

The atoms in a crystal are ordered into what is known as a crystallographic lattice. A basic assumption for diffraction is to assume that a beam of radiation hitting an atom in the lattice, will make the atom radiate the incident radiation in all directions at the same frequency [87]. Because X-rays are electromagnetic waves, the radiation emitted from different sites in the lattice will interfere as it radiates outwards. In certain directions, determined by the structure of the lattice, constructive interference gives rise to enhanced radiation intensity.

In most cases, we can regard the incident beam as a plane wave, which we write as $e^{i\boldsymbol{k}\cdot\boldsymbol{r}}$, where $\boldsymbol{k}$ is the wave vector. The diffracted beam can be written as $e^{i\boldsymbol{k}'\cdot\boldsymbol{r}}$, and we use this to define the scattering vector $\boldsymbol{q}$ simply as the difference between the wave vectors of the incident and the diffracted beams:

$$\boldsymbol{q} = \boldsymbol{k}' - \boldsymbol{k}\,. \tag{5.5}$$

Some of the properties of $\boldsymbol{q}$ are easily seen from Figure 5.5. Within the scope of this thesis we may assume *elastic* scattering where no energy or momentum is exchanged between photon and scatterer. It is then obvious that $|\boldsymbol{k}| = |\boldsymbol{k}'| = 2\pi/\lambda$, and the magnitude of the scattering vector is given by

$$|\boldsymbol{q}| = \frac{4\pi \sin\theta}{\lambda}\,. \tag{5.6}$$

In the above equation, θ is the scattering angle, and λ is the wavelength of the wave.

Let us now consider the interference of the scattered waves due to two particles at different locations. An illustration can be seen in Figure 5.6. Provided that the sample-to-detector distance is large compared to the sample diameter, the scattered waves from the two atoms have the same direction [29]. After the scattering, a phase difference between the scattered waves exists, resulting from the differences in path length. The phase delay of the wave scattered from particle 2 is the sum of

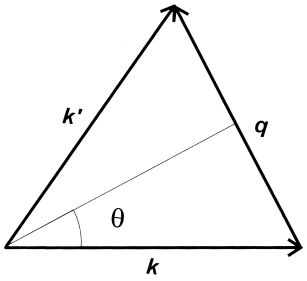

FIGURE 5.5: Definition of the scattering vector. Adapted from [29].

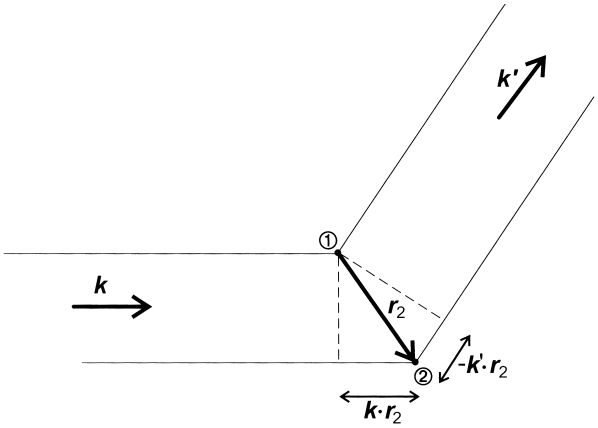

FIGURE 5.6: The phase difference between the scattered waves originating at atoms 1 and 2. Adapted from [29].

the two components indicated in Figure 5.6, and this is easily shown to be

$$\Delta\phi = r_2(\boldsymbol{k}' - \boldsymbol{k}) = r_2\boldsymbol{q}\,. \tag{5.7}$$

The result for two scatterers can be generalized to the case of a large three-dimensional Bravais lattice, where the scattering vector r_2 must be substituted with the translation vector $\boldsymbol{R}_{uvw}$. The translation vector is the sum of the three fundamental translation vectors $\boldsymbol{a}$, $\boldsymbol{b}$, and $\boldsymbol{c}$:

$$\boldsymbol{R}_{uvw} = u\boldsymbol{a} + v\boldsymbol{b} + w\boldsymbol{c}\,, \tag{5.8}$$

where u, v and w are integers. By correct choice of u, v and w, the translation vector connects any two lattice points. For the scattered waves from all lattice points to interfere constructively, the overall phase factor must equal unity, i.e.

$$e^{i\boldsymbol{q}\cdot\boldsymbol{R}_{uvw}} = 1\,. \tag{5.9}$$

The Laue condition for diffraction from a crystal states that Equation (5.9) is only satisfied when $\boldsymbol{q}$ is equal to a reciprocal-lattice vector $\boldsymbol{G}_{hkl}$, that is:

$$\boldsymbol{q} = \boldsymbol{G}_{hkl} \,. \tag{5.10}$$

A complete discussion of the reciprocal lattice is too comprehensive to include here – see e.g. Elliot [87] for a more thorough treatment – but a few definitions are given. Many times it is useful to describe the crystal structure in terms of *crystal planes* instead of atomic positions (lattice points). A convenient way to do this is to define the vector

$$\boldsymbol{G}_{hkl} = 2\pi \frac{\hat{\boldsymbol{n}}_{hkl}}{d_{hkl}} \,, \tag{5.11}$$

where $\hat{\boldsymbol{n}}_{hkl}$ is a unit vector normal to the plane (hkl), and d_{hkl} is the interplanar spacing. The indices (hkl) are called *Miller indices* and are for a plane defined as the "smallest three integers corresponding to the reciprocals of the intersections of the plane with the axes" [87]. In addition to the definition in Equation 5.11, the reciprocal lattice vector can be represented in terms of these indices and three basic reciprocal lattice vectors

$$\boldsymbol{G}_{hkl} = h\boldsymbol{a}^* + k\boldsymbol{b}^* + l\boldsymbol{c}^* \,, \tag{5.12}$$

where each reciprocal lattice vector is perpendicular to two regular basis vectors, e.g.

$$\boldsymbol{a}^* \cdot \boldsymbol{a} = 2\pi \tag{5.13a}$$

and

$$\boldsymbol{a}^* \cdot \boldsymbol{b} = \boldsymbol{a}^* \cdot \boldsymbol{c} = 0 \,. \tag{5.13b}$$

Returning to the Laue condition, it is clear that the more known Bragg condition for diffraction can be derived from it. By equating the magnitudes in Equation (5.10), $|\boldsymbol{q}| = |\boldsymbol{G}_{hkl}|$, Bragg's law follows immediately:

$$2d \sin\theta = n\lambda \,. \tag{5.14}$$

Bragg's law may also be derived geometrically by looking at the reflection from two parallel planes, which is done in Figure 5.7. While this interpretation is often more easily understood, the phenomenon of X-ray diffraction from crystallographic planes is not a surface reflection. The X-rays penetrates to several million crystallographic layers, and each layer contributes only a very small part to the diffracted beam. Nevertheless, Bragg's law and its derivation from surface planes is easy to remember and a useful tool when calculating the interlayer distance from a measured diffraction angle.

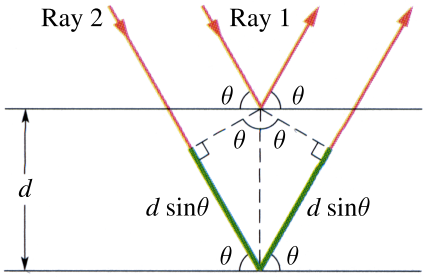

FIGURE 5.7: Geometrical illustration of Bragg's law. For constructive interference to occur, the difference in optical path length traveled by the two waves, $2d \sin\theta$, must be equal to an integer multiple of the wavelength. Adapted from [88].

5.2.2 The atomic form factor

Knowing Bragg's law we are ready to consider the amplitude of the scattered waves. The overall scattering amplitude of waves diffracted from the plane (hkl) in a crystal is given by

$$E_{hkl} \propto \sum_i f_i e^{i\boldsymbol{G}_{hkl}\cdot\boldsymbol{R}_i} , \tag{5.15}$$

where f_i is the atomic form factor and the summation extends over all atoms. The form factor depends on the type of radiation used. For the case of X-ray diffraction, the scattering process can be thought of as the interaction of the incoming beam with the electrons in the atoms. The electrons absorb the X-ray photon, immediately followed by a de-excitation and re-radiation. Since the wavelength of X-rays are comparable to the size of atoms, *intra*-atomic interference effects are important, making the X-ray atomic form factor strongly dependent on $\boldsymbol{q}$.

In order to find an expression for the form factor, we substitute the summation in Equation (5.15) with an integral. It is reasonable to assume that the amplitude scattered from a particular volume element $\mathrm{d}V$ is proportional to $n(\boldsymbol{r})\mathrm{d}V$, where $n(\boldsymbol{r})$ is the electron charge density contained within the volume element at position $\boldsymbol{r}$. By integrating over the whole sample volume we then get

$$E = \int n(\boldsymbol{r}) e^{i\boldsymbol{q}\cdot\boldsymbol{r}} \mathrm{d}V , \tag{5.16}$$

where we have substituted $\boldsymbol{G}_{hkl}$ with a general scattering vector $\boldsymbol{q}$. We can write the total electron concentration of the sample as the sum over the electron concentrations n_i of the individual atoms i, i.e.

$$n(\boldsymbol{r}) = \sum_i n_i(\boldsymbol{r} - \boldsymbol{r}_i) . \tag{5.17}$$

By including this in Equation (5.16) and making the substitution $\boldsymbol{r} - \boldsymbol{r}_i = \boldsymbol{\rho}$ we get

$$E = \sum_i e^{i\boldsymbol{q}\cdot\boldsymbol{r}_i} \int n_i(\boldsymbol{\rho}) e^{i\boldsymbol{q}\cdot\boldsymbol{\rho}} \mathrm{d}V \,. \tag{5.18}$$

It is clear from comparing Equation (5.18) with Equation (5.15) that the X-ray atomic form factor is given by

$$f_i = \int n_i(\boldsymbol{r}) e^{i\boldsymbol{q}\cdot\boldsymbol{r}} \mathrm{d}V \,. \tag{5.19}$$

5.2.3 Scattering intensity

Intensity for systems with only one type of particles

When we perform diffraction experiments, or for that matter any experiment with electromagnetic radiation, the measured quantity is not the amplitude of the electric field, but rather the intensity of the radiation. Because experimental measurements always require a definite time and the particles in a sample are generally moving, the measured intensity is also a time-average. Knowing this, we can express the intensity measured by the detector in the following way:

$$I(\boldsymbol{q}) \propto \left\langle |E(\boldsymbol{q})|^2 \right\rangle \propto \sum_{j,k} f_j f_k \left\langle e^{-i\boldsymbol{q}(\boldsymbol{r}_j - \boldsymbol{r}_k)} \right\rangle . \tag{5.20}$$

In many cases, diffraction experiments are carried out on samples where there is only one type of particles. When that is true, the atomic or molecular form factors f_j are all the same, and do not need to be considered further [29]. This means that only the sum over all phase terms is important:

$$C(\boldsymbol{q}) = \sum_j e^{-i\boldsymbol{q}\cdot\boldsymbol{r}_j} \,. \tag{5.21}$$

It is useful to introduce another function $S(\boldsymbol{q})$ called the *interference function*,

$$S(\boldsymbol{q}) = \frac{1}{\mathcal{N}} \left\langle |C(\boldsymbol{q})|^2 \right\rangle , \tag{5.22}$$

where the number or particles, $\mathcal{N}$, is introduced because the scattered intensity must be proportional to this number. $S(\boldsymbol{q})$ has many names, and is also known as the *structure function* or the *scattering function*. Combining the last three equations, we see that the intensity is proportional to the interference function multiplied by the number of particles

$$I(\boldsymbol{q}) \propto \mathcal{N} S(\boldsymbol{q}) \,. \tag{5.23}$$

Intensity from ideal crystals

Although many scattering experiments are performed on liquids or systems with only one particle type, we also need to discuss crystal diffraction for crystals that consist of more than one type of atoms. For these kind of systems we cannot ignore the form factors. A starting expression for the scattering intensity distribution can be expressed as [29]

$$I(\boldsymbol{q}) \propto \mathcal{N}_1\mathcal{N}_2\mathcal{N}_3 \, |f_c(\boldsymbol{q})|^2 \, S(\boldsymbol{q}) \, . \tag{5.24}$$

The number of unit cells along the three axes of the lattice is given by $\mathcal{N}_1$, $\mathcal{N}_2$ and $\mathcal{N}_3$, while $f_c(\boldsymbol{q})$ is the cell structure factor. This factor is due to the superposition of the waves scattered from all n atoms in the cell

$$f_c(\boldsymbol{q}) = \sum_{j=1}^{n} f_j e^{-i\boldsymbol{q}\cdot\boldsymbol{r}_j} \, . \tag{5.25}$$

The interference function $S(\boldsymbol{q})$, which now describes the interference between all unit cells of the crystal, needs some modification from Equation (5.22). It can be shown, see e.g. Strobl [29], that in the case of a crystal, $\boldsymbol{q}$ must be substituted with $\boldsymbol{G}_{hkl}$. This should hardly come as a surprise, seeing as we have already discussed the Laue condition for diffraction from crystals: $\boldsymbol{q} = \boldsymbol{G}_{hkl}$.

Using the Laue condition, and introducing ρ_c, the number of unit cells per unit volume, the interference function of the lattice can be written as

$$S_L(\boldsymbol{q}) = \rho_c \sum_{hkl\neq 000} \delta(\boldsymbol{q} - \boldsymbol{G}_h kl) \, . \tag{5.26}$$

Combining this function with Equation (5.24), the scattered intensity distribution from an ideal crystal is

$$I(\boldsymbol{q}) \propto \mathcal{N}_1\mathcal{N}_2\mathcal{N}_3 \, |f_c(\boldsymbol{q})|^2 \, \rho_c \sum_{hkl\neq 000} \delta(\boldsymbol{q} - \boldsymbol{G}_h kl) \, . \tag{5.27}$$

Intensity from real crystals

Next, we move on to consider the intensity from a non-ideal crystal. We have so far assumed that the scattering atoms are completely aligned with the points in an ideal Bravais lattice. In reality, thermal motion in a crystal leads to deviations of all atoms from their equilibrium positions. The most simple case to consider is when the whole unit cell is displaced, a phenomenon caused by acoustic lattice vibrations [29]. One way to express this is through the *pair distribution function*, $g_2(\boldsymbol{r})\mathrm{d}^3\boldsymbol{r}$. It describes the average structure in the region around a chosen atom

or molecule, and is defined as "the number of atoms or molecules whose centre of gravity is, on average, in a volume element of size $\mathrm{d}^3\boldsymbol{r}$ at a distance $\boldsymbol{r}$ from the chosen atom" [29]. For an ideal crystal, this is expressed by a δ-function, while in the case of acoustic vibration, we exchange the δ-function with a probability distribution

$$g_2(\boldsymbol{r}) = \sum_{uvw \neq 000} w(\boldsymbol{r} - \boldsymbol{R}_{uvw})\,. \tag{5.28}$$

By expressing the pair distribution function in the form of a convolution, the interference function can be shown to be

$$S(\boldsymbol{q}) = \mathrm{Ftr}\; w \cdot S_L(\boldsymbol{q}) + (1 - \mathrm{Ftr}\; w)\,, \tag{5.29}$$

where Ftr means to take the Fourier transform. The fact that the interference function for an ideal crystal, S_L, is present in the equation is interesting. This means that the same reflections are observed for a real crystal, as would be expected for an ideal crystal, but that the intensities are weakened by a factor Ftr w, called the *Debye–Waller factor*. In many cases, the probability distribution w is approximated with a Gaussian, which gives Ftr $w = \exp(-\langle \Delta r^2 \rangle q^2/6)$ as the value of the Debye–Waller factor. The second term in Equation (5.29) is known as *thermal diffuse scattering*, which is a continuous background scattering component that sometimes needs to be considered when dealing with real data.

Besides thermal motion, other factors that need to be considered when discussing the measured intensity from a crystallite include the finite size of the sample and the properties of the beam: polarization, monochromatization and collimation. It is generally true that the width of a Bragg peak is inversely proportional to N, the number of unit cells in the sample. The already discussed Laue condition, where we achieve scattering exclusively at $\boldsymbol{q} = \boldsymbol{G}_{hkl}$ remains true only for infinitely large crystals. The case for finite-sized samples is illustrated in Figure 5.8. If $\boldsymbol{q}$ falls within the elliptical contour shown in the figure, appreciable intensity is obtained, and the scattered beam will have some divergence [84]. If the scattered waves were recorded on a two-dimensional detector, this would result in a smearing out of the Bragg peak on the detector. An equivalent smearing occurs for a beam that is not perfectly collimated or perfectly monochromatized. Broadening due to beam properties is termed *instrumental* and is generally undesirable.

The broadening of a Bragg peak due to particle-size can be estimated from the *Scherrer* equation

$$L = \frac{\lambda K}{\beta \cos\theta}\,, \tag{5.30}$$

where L is the mean crystallite dimension in Ångstrøms along a line normal to the reflecting plane, K is a constant near unity, and β is the full width at half maximum

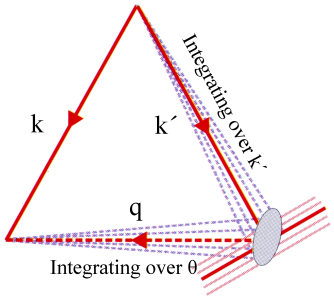

FIGURE 5.8: The effect of a finite-sized sample on X-ray diffraction. The scattering from the reciprocal shape of a small crystallite is represented by the gray ellipse. For a given orientation, the detector accepts all of the scattered wave vectors $\boldsymbol{k}'$ that falls on the red line. Adapted from [84].

of the peak expressed in radians of 2θ [86].

5.2.4 Powder diffraction

There are several ways of designing an X-ray diffraction experiment. For samples that exist as single crystals, single-crystal X-ray diffraction measurements may be performed. The method used for the experiment in this thesis however, is *powder diffraction*. In powder diffraction experiments, one assumes that the scattering volume contains crystallites oriented in all possible directions. Imagine a crystal oriented with respect to the incident beam, so that it fulfills Bragg's law and produces a diffraction peak. If this crystal was to be rotated around the direction of the incident wave, the scattered wave vectors would also be rotated, and distribute themselves evenly on a cone that has its tip at the crystal. This is illustrated in Figure 5.9. With the assumption that the crystallites in a powder sample have all possible orientations, scattering into this cone will even occur without rotation of the sample. The cone has apex half angle 2θ, and is called the *Debye–Scherrer* cone after the two physicists who first correctly interpreted X-ray scattering from a powder [84].

5.2.5 Scattering from a layered clay

The interference function

For those working with scattering from macromolecules (like clays), it is not only the peak position, but also the shape of the diffraction peak that contains information. As the discussion in Section 5.2.3 show, the scattering from small thin crystals, such as those of the clay minerals, contains additional scattering adjacent

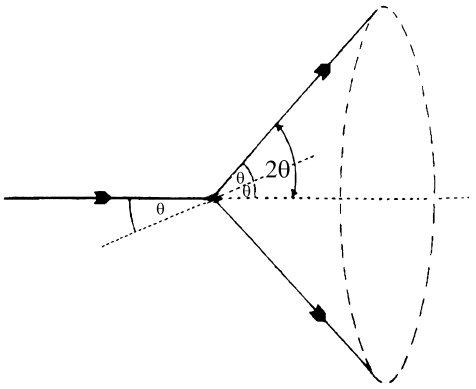

FIGURE 5.9: Schematic illustration of the Debye–Scherrer cone resulting from the diffracted radiation from lattice planes at θ-degrees with respect to the incident beam. Adapted from [87].

to the Bragg peak positions. This suggests that we need to change the interfere function $S(\boldsymbol{q})$ from a discrete function of (hkl), into something continuous in θ [86]:

$$S_{lc}(\theta) = \sum_{N=n_1}^{N=n_2} p(N) \frac{\sin^2(2\pi N D \lambda^{-1} \sin\theta)}{\sin^2(2\pi D \lambda^{-1} \sin\theta)} \,. \tag{5.31}$$

In the above equation, N is the number of unit cells stacked in the direction perpendicular to the layers, and d is the interplanar distance d_{001}. The summation over N is introduced because we assume the sample is composed of crystallites with different values of N. $p(n)$ is then the proportion of crystallites with $N = n$. Equation (5.31) can be derived by considering the layered clay as a *diffraction grating*, see Alme [89] for a short discussion.

The layer structure factor

In addition to the interference function, we need to introduce the *layer structure factor* that is also continuous in θ. In the discussion about ideal crystals, the cell structure factor was given in Equation (5.25), and the layer structure factor can be derived from this. If we for simplicity assume a centre of symmetry in the unit cell and take the distances $\boldsymbol{r}_j$ to be from that centre, the sine part of $e^{-i\boldsymbol{q}\cdot\boldsymbol{r}}$ vanishes and we can write the structure factor as

$$G(\theta) = \sum_{j=1}^{n} f_j \cos(\boldsymbol{q} \cdot \boldsymbol{r}) \,. \tag{5.32}$$

If we assume $\boldsymbol{q}$ perpendicular to the Bragg plane, which is true for $(00l)$ diffraction peaks, the dot product can be reduced to qz_j, where z_j is the projection of r_j onto

the line from the centre of symmetry to the $(00l)$ plane. The final expression for the layer structure factor is found by rewriting q as we did in Equation (5.6), $q = 4\pi \sin\theta/\lambda$, and we find

$$G(\theta) = \sum_{j=1}^{n} f_j \cos\left(4\pi z_j \frac{\sin\theta}{\lambda}\right). \tag{5.33}$$

The Lorenz-Polarization factor

One final factor that needs to be included is the *Lorenz-Polarization factor*. This factor is a combination of the *Lorenz factor* and the *polarization factor*. The former is a geometrical factor that considers the volume of the crystal exposed to primary radiation, and the number of crystals that are favourably oriented for diffraction. It is given by

$$L = \frac{1}{\sin(2\theta)\sin^{\beta}\theta}. \tag{5.34}$$

This factor depends on the sample being studied, with the exponent β taking the value of 1 for a random powder, and 0 for single crystals [86]. For layered clays, β is somewhere in between these values.

The polarization factor relates the scattered intensity to the polarization of the incoming light. In much the same way as light reflected off the hood of a car becomes polarized, so does the radiation reflected from planes of atoms [86]. If the incident beam is unpolarized, the polarization factor is only dependent on the scattering angle: $P = (1 + \cos^2 2\theta)/2$ [84]. If, on the other hand, the incident beam is polarized – such as the case of synchrotron radiation – the polarization factor is dependent on ψ, the angle of deflection in the horizontal plane. This is illustrated in Figure 5.10. The reason for this is that the synchrotron X-ray beam has its electrical field polarized in the horizontal plane. The electrons excited by the field oscillate along the x-direction, and in consequence they do not radiate in that direction. The polarization factor for a horizontally polarized incident beam is thus [84]

$$P = \cos^2\psi. \tag{5.35}$$

If we combine these two factors, and stick to the synchrotron variation of the polarization factor, the Lorenz-Polarization factor becomes

$$Lp(\theta,\psi) = \frac{\cos^2\psi}{\sin(2\theta)\sin^{\beta}\theta}. \tag{5.36}$$

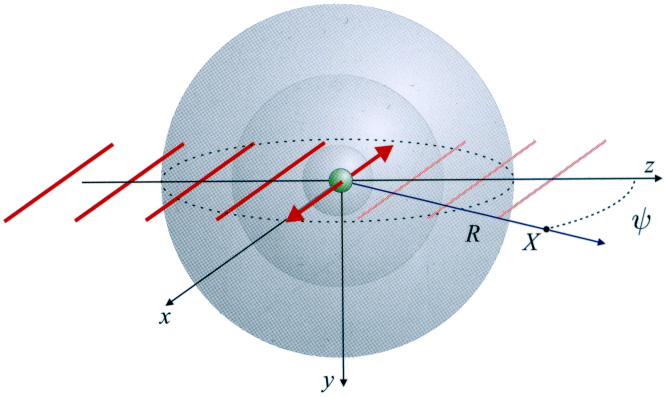

FIGURE 5.10: Illustration of X-ray scattering by an electron (classical description). The electrical field of an incident wave (red lines) sets the electron in oscillation along the x-axis (red arrows). The oscillation makes the electron radiate like a dipole, hence the amplitude in the horizontal plane decays with $\cos\psi$. That is $P = 1$ along z and $P = 0$ along x. Adapted from [84].

Putting it all together

To conclude, we combine all three factors – the layer structure factor, the interference function, and the Lorenz-polarization factor – and obtain an expression for the measured scattering intensity from a layered clay

$$I(\theta) \propto |G(\theta)|^2 \, S(\theta) Lp(\theta, \psi) \, . \tag{5.37}$$

We also include the Debye–Waller factor, to account for thermal acoustic vibrations in the system. Our final expression then, all considered factors included, is

$$\begin{aligned} I(\theta) \propto \quad & e^{-\frac{\langle \Delta r^2 \rangle q^2}{6}} \times \frac{\cos^2 \psi}{\sin 2\theta \sin^{\beta} \theta} \\ & \times \left[\sum_{j=1}^{n} f_j \cos\left(4\pi z_j \frac{\sin\theta}{\lambda} \right) \right]^2 \\ & \times \left[\sum_{N=n_1}^{N=n_2} p(N) \frac{\sin^2\left(2\pi N D \frac{\sin\theta}{\lambda}\right)}{\sin^2\left(2\pi D \frac{\sin\theta}{\lambda}\right)} \right] . \end{aligned} \tag{5.38}$$

Chapter 6

Experiment

6.1 Experimental setup

6.1.1 ESRF

This synchrotron wide-angle X-ray scattering (WAXS) experiment was performed at the *Swiss-Norwegian Beamline* (BM1A) at the *European Synchrotron Radiation Facility* (ESRF) in Grenoble, France (Figure 6.1). The experiment was performed as part of a three-day experimental session in March 2007. ESRF is a joint facility supported and shared by 18 European countries, and is the most powerful synchrotron radiation source in Europe [90].

FIGURE 6.1: The synchrotron at ESRF as seen from La Bastille, Grenoble. Taken from [91].

6.1.2 Sample holder

The sample holder was custom made at the engineering workshop at NTNU, and was based on a previous design by Daví Fonsêca. It included an 80 mm long, 2 mm

diameter glass capillary (*Hilgenberg Mark* tube with 0.01 mm wall thickness), and an aluminium setup for mounting the capillary. The aluminum setup consisted of two parts. Firstly, a small movable frame allowed for vertical translation. The frame had a hole on top that the capillary could be inserted into. Secondly, a quadratic base was made with a rail for the frame to move in, and this was attached to the goniometer. The sample holder was originally designed for an experiment at another beamline, and proved far from ideal. A notch had to be made in the base in order to fit it to the goniometer, and since the goniometer had no motor for vertical translation, the frame had to be moved manually each time a vertical translation was needed. An image of the setup is shown in Figure 6.2.

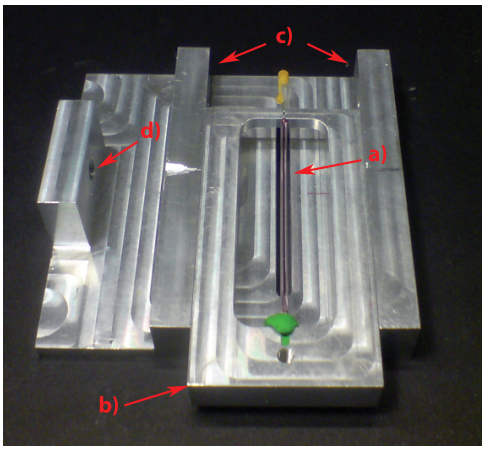

FIGURE 6.2: The sample holder used at ESRF. **a)** The capillary. **b)** Movable frame. **c)** Rail. **d)** Hole for goniometer attachment.

6.1.3 Software

The native software of the detector, *MAR345dtb*, was used for data collection, and the collected images were stored as binary .mar2300 files. The binary files contain a header with scan parameters, including scan time, beam intensity, pixel size, etc. The Fit2D software, developed at ESRF by Dr. Andy Hammersley [92], was used firstly for LaB_6 calibration and secondly to perform batch integration of the binary data files. A Perl-script written by Professor Yves Méheust was used to generate macros for Fit2D, and MATLAB was used for all further analysis and plotting.

6.2 Experimental method

6.2.1 NaFh samples

The NaFh clay used in this experiment was purchased from Corning as pure fluorohectorie and ion exchanged through dialysis to produce sodium fluorohectorite having the nominal chemical formula $Na_{0.6}Mg_{2.4}Li_{0.6}Si_4O_{10}F_2$ [30]. A more thorough description of the ion exchange process can be found in Méheust et al. [93].

The sample was prepared at the Complex lab at the Department of Physics, NTNU, four weeks before going to ESRF. Clean deionized water was mixed with 1×10^{-3} M NaCl, and 3 w/w % NaFh. The correct quantities of salt and clay were measured using an *Ohaus* precision scale, while the mixing was done on a mechanical shaker manufactured by *Heidolph*. After all the NaFh had dispersed in the saline water, the solution was inserted into the capillary using a syringe with a long needle. The reason for using a syringe was to prevent bubbles of air inside the capillary. When the needle is inserted all the way into the end of the capillary before being emptied, the air is pushed out as the liquid goes in. The capillary was sealed properly with capillary wax from *Hampton Resarch*, and the sample was left in an upright position to settle.

6.2.2 Imaging

The aim of the experiment was to study the preferential orientation of the NaFh platelets within the sample. We did this by scanning the capillary vertically in steps of one millimeter, and recorded the scattered intensity at each step. We started by taking the first scan just below the sample, and after that moving the sample one millimeter down between each image. This resulted in a series of 38 images. Of these 38, three were taken below the sample, and the last one at the very top. In other words, the relevant images we are left with are the bottom 33 millimeters of the sample, as well as an additional scan at 56 mm for reference. In order to move the sample between each scan, the experimental hutch had to be opened and the sample moved manually. This proved to be a rather lengthy procedure, due to a safety waiting time of one minute to allow evacuation of the hutch.

An example image of the collected X-ray diffraction patterns is shown in Figure 6.3. For the imaging, the monochromatic beam with wavelength $\lambda = 0.8089$ Å was slit-collimated down to 0.3×0.3 mm, and the sample-to-detector distance and parameters of the detector were calibrated using a standard LaB_6 sample. A summary of the X-ray imaging parameters can be found in Table 6.1.

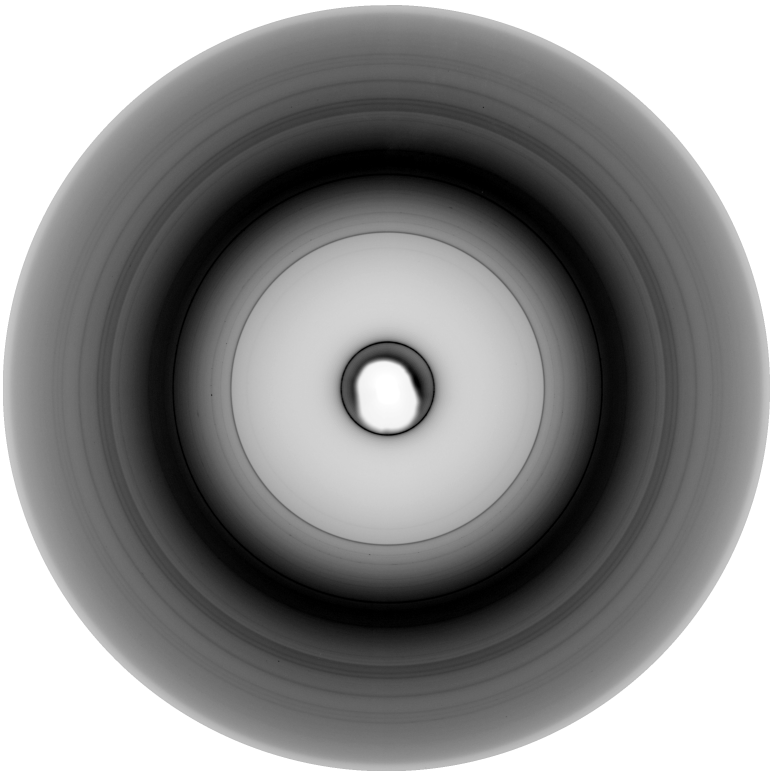

FIGURE 6.3: Example of a collected X-ray diffraction pattern. The data are shown using an inverted linear grayscale, dark pixels meaning higher intensity. The beamstop is visible in the centre, just outside is the (001) Bragg peak, while the next clear ring results from inplane difraction. The broad dark ring is the diffuse scattering from water.

TABLE 6.1: Summary of the X-ray imaging parameters.

Vertical pixel size	$150\,\mu m$
Horizontal pixel size	$150\,\mu m$
Sample-to-detector distance†	389.6180 mm
Wavelength	0.8089 Å
Angle of detector tilt†	6.7187×10^{-03} deg
Time of scan	180 s
Collimator	0.3×0.3 mm
Calibrant	Lanthanum Hexaboride

†Determined from calibration with LaB_6

Chapter 7

Data analysis and discussion

7.1 Data acquisition and processing

7.1.1 Calibration

After all the data acquisition was finished we imaged a sample of LaB_6. Except for a scan time of 60 s, this was done with the same parameters as for the NaFh imaging. LaB_6 is a substance with well known and clearly defined Bragg peaks. Since the 2θ scattering angles are tabulated, this allows for precise determination of the sample-to-detector distance, the tilt of the detector plane and the beam centre relative to the detector. To find the parameters, we used a very convenient function of Fit2D. The program has built-in algorithms for the calibration based on tabulated values for a number of calibrants, including LaB_6. All one needs to do is to load the diffraction image, select the calibrant used, and mark a number of points on the (001) Debye ring.

7.1.2 Applying the Méheust model to analyze the data

Recently, Méheust et al. have developed a model for inferring orientational distributions in anisotropic powders from two-dimensional WAXS images [33], and this model proved perfectly suited to analyze the data in our experiment. For the rest of this thesis, we will refer to the model simply as the *Méheust model*. Before the model was used to treat our data, the current author actually helped port a distribution to MS Windows, and even extended the scripts to account for the fact that our sample contains both nematic and anti-nematic geometries. A complete description of the model can be found in the Journal of Applied Crystallography article [33], but the most important aspects will be explained here.

The geometry of the model is shown in Figure 7.1. It considers a clay sample placed at the origin O of the laboratory frame $(O, \boldsymbol{x}, \boldsymbol{y}, \boldsymbol{z})$, and looks at the inten-

sity recorded in the detector plane $zO'z$. It is important to note that Fit2D defines $\phi = 0$ to be along y, not z as in Figure 7.1. All the results outputted by the scripts are therefore given with this as a reference. In the results and discussion presented here though, we have accounted for this, and Figure 7.1 is hence correct.

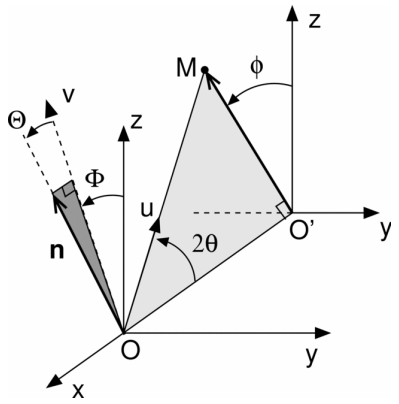

FIGURE 7.1: The geometry of the Méheust model. The most important quantities for our analysis are the azimuthal angle ϕ, the angle with the zOx plane Φ and the angle with the yOz plane Θ. The latter two angles define the orientation of the reference director $\boldsymbol{n}_0$ of the crystallite with respect to the fixed frame. Taken from [33].

The NaFh sample is considered as a population of oriented nano-layered crystallites with an orientation distribution probability (ODP) function f dependent on the angle between the director $\boldsymbol{n}$ and a reference orientation $\boldsymbol{n}_0$. The density probability function is normalized with respect to the total solid angle available to the description

$$\int_0^{2\pi}\int_0^{2\pi} f(\alpha)\sin\alpha \, \mathrm{d}\alpha \, \mathrm{d}\beta = 1\,. \tag{7.1}$$

We assume there exist two different anisotropic geometries in our sample, a *uniaxial nematic* configuration and a *uniaxial anti-nematic* configuration. We base this on earlier studies of NaFh (e.g. Fossum et al. [27]), on birefringent studies of the same sample type [28], and simply by looking at the WAXS-images. In the classical uniaxial nematic geometry, the reference orientation is the mean orientation for the population of nano-stacks [33]. Just by considering the symmetry of our sample (disregarding the area closest to the walls) we can assume such a geometry to exist only in an area where the particles have their mean orientation along z. As this means that the particles are "lying down", the anisotropic scattering should have its peaks within $-45° < \phi < 45°$ or $135° < \phi < 225°$, and we use this as a condition for when to apply the nematic distribution in our scripts.

In the anti-nematic configuration, the crystallites have their direction, on aver-

age, in a plane perpendicular to the reference direction [33]. In our sample, this means that the particles are "standing up", but that the particle director can have a random direction within the $\boldsymbol{x}\,O\,\boldsymbol{y}$ plane. Order parameters for the configurations can be defined as

$$S_2 = \tfrac{1}{2}\left\langle 3\cos^2\alpha - 1\right\rangle_f = \left\langle \chi_n(\alpha)\right\rangle_f , \qquad \text{nematic} \tag{7.2}$$

$$S_2 = \left\langle 3\sin^2\alpha - 2\right\rangle_f = \left\langle \chi_a(\alpha)\right\rangle_f , \qquad \text{anti-nematic,} \tag{7.3}$$

with $\langle\ \rangle$ denoting an average:

$$S_2 = 2\pi \int_0^{\pi/2} \chi(\alpha)\, f(\alpha) \sin\alpha \, \mathrm{d}\alpha , \tag{7.4}$$

and α being the angle between $\boldsymbol{n}$ and $\boldsymbol{n}_0$ in both cases.

Without discussing the model in two much detail, it assumes that the ODP distribution f only depends on one characteristic angle. The dependence on the angle has to be chosen with a given functional form, which in this case we have chosen to be a Maier-Saupe function

$$f_n(\alpha) \propto \exp(m\cos^2\alpha) , \qquad \text{nematic} \tag{7.5}$$

$$f_a(\alpha) \propto \exp(m\sin^2\alpha) , \qquad \text{anti-nematic,} \tag{7.6}$$

where an expression for α can be found geometrically e.g. by taking the dot product of $\boldsymbol{n}$ and $\boldsymbol{n}_0$

$$\boldsymbol{n}(\phi) = \begin{pmatrix} \sin\theta \\ -\cos\theta\sin\phi \\ \cos\theta\cos\phi \end{pmatrix} \tag{7.7}$$

$$\boldsymbol{n}_0 = \begin{pmatrix} \sin\Theta_0 \\ -\cos\Theta_0\sin\Phi_0 \\ \cos\Theta_0\cos\Phi_0 \end{pmatrix} . \tag{7.8}$$

Here $\boldsymbol{n}(\phi)$ is expressed as a function of the scattering angle θ. This is because for a crystallite to scatter, the stacking planes must make an angle θ with the incident beam that corresponds to the Bragg condition for the crystallite. As a consequence of this, the model can be used to extract information not just from the (001) peak, but from all $(00l)$ peaks, if visible.

Although it might seem complicated when explained so superficially, the model is actually quite straightforward and has the advantage that it can determine the ori-

entation distribution of the particles from only a single two-dimensional scattering image.

7.1.3 Extracting azimuthal profiles from the WAXS data

To extract a Bragg peak – or rather a Debye–Scherrer cone – to analyze, we use Fit2D. A Perl script written by Yves Méheust generates macros that tells Fit2D to compute diffraction lines at azimuthal angles ϕ_m, varying ϕ_m between 0 and 355° in steps of 5°. Both to reduce noise, and to utilize all the data, each diffraction line is obtained by integrating over ϕ in the region $[\phi_m - 2.5°,\ \phi_m + 2.5°]$. An example of such a diffraction line is shown in Figure 7.2. In generating the macros, the Perl script accounts for beam decay, and tells Fit2D to scale the intensity accordingly. The information about intensity, beam centre, sample-to-detector-distance, etc. is extracted from information found in the .mar2300 header and a log-file stored during LaB_6 calibration.

The azimuthal profile for the (001) peak was found from the diffraction lines by a MATLAB-script written by Yves Méheust, with minor modifications by the current author. An approximate q value for the peak is given to the script, and for each diffraction line it looks for the maximum peak intensity in a small window around the approximate value. The true q value is then found by taking the average of the q's chosen for all lines. Figure 7.3 shows all extracted azimuthal profiles.

7.2 Data analysis and results

7.2.1 Fitting the azimuthal profiles

It seems obvious from Figure 7.3 that our sample contains a sediment, a nematic phase and an isotropic phase. This is consistent with earlier studies of the same system [30]. What is interesting is the red asymmetric profile centred around $I \approx 1700$. The intensity-peak of this profile seems to be shifted approximately 90° with respect to the profiles above it, and indicates a uniaxial nematic geometry, where the NaFh particles are lying down. As will be discussed later, this phenomenon has previously been observed using other experimental techniques, but has never been properly treated.

In the following, the 14 profiles starting at the uniaxial nematic at $I \approx 1700$ and ending at the green profile at $I \approx 3000$ will for simplicity be given the collective name *the nematic phase*. A disagreement exists whether what we so far have called the uniaxial anti-nematic instead should be denoted biaxial nematic, or even just nematic [30]. That discussion will not be taken here, but a distinction between the region where all particles on average are parallel to their neighbours, and the

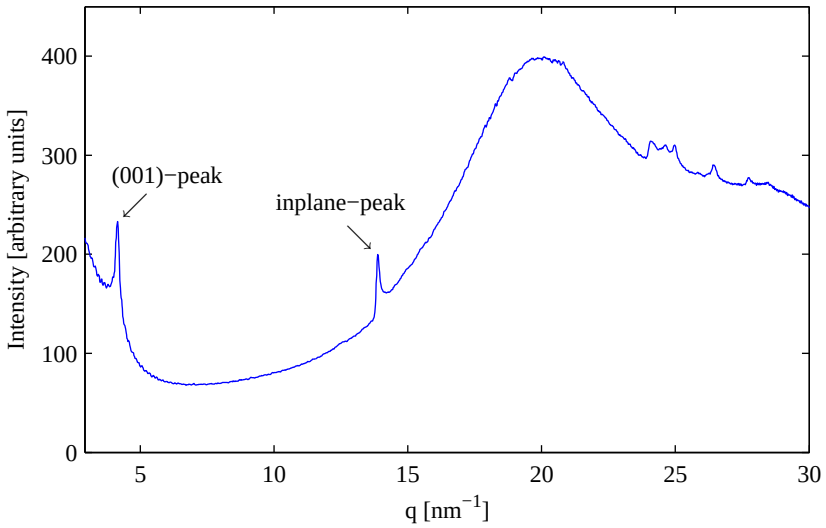

(a)

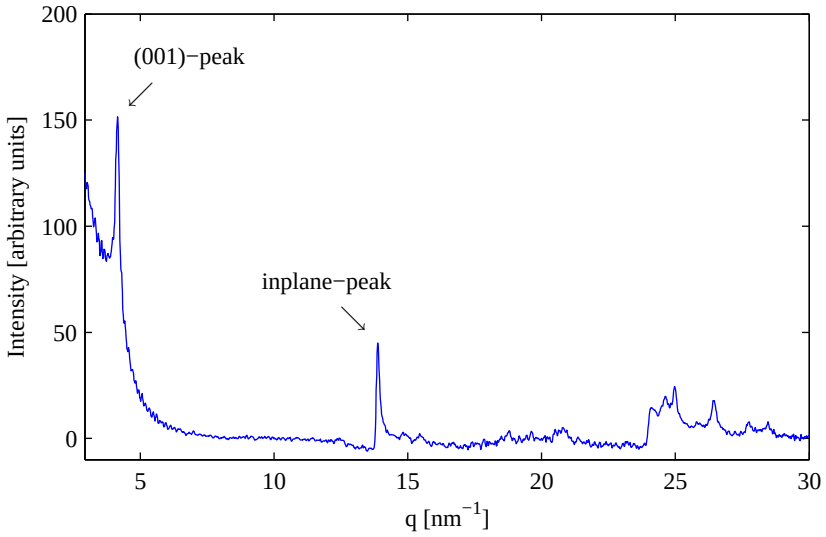

(b)

FIGURE 7.2: **a)** An example of a diffraction line used for analysis in the Méheust model. This particular line was computed from the ϕ-region $[-2.5°,\ 2.5°]$ for the scan at height 16 mm in the capillary. **b)** The same diffraction line with the background from a reference scan at the top of the capillary subtracted.

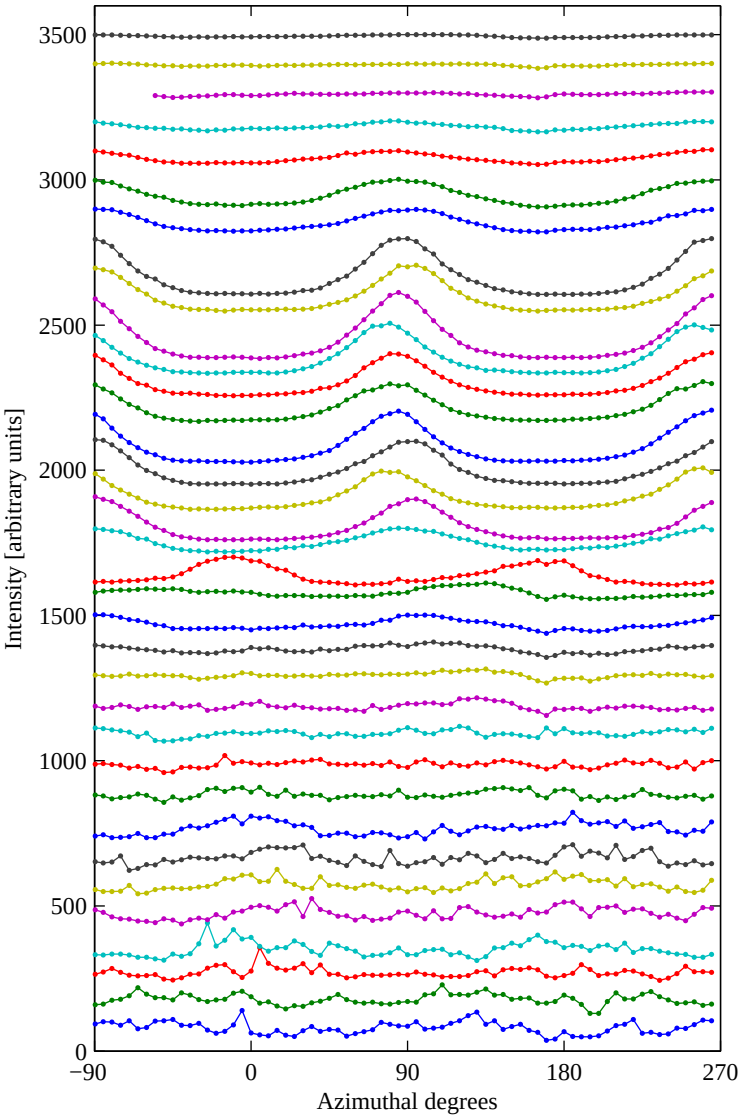

FIGURE 7.3: Azimuthal profiles for the (001) ring translated vertically according to the height they were recorded at. The distance between each profile is 1 mm, excluding the topmost, which were recorded at the top of the capillary (as a reference). The lowermost profile is the one taken at the bottom of the capillary.

region where they just have their directors in the same plane is in all cases relevant, so we will stick to the nematic/anti-nematic terminology for clarity.

The azimuthal profiles of the nematic phase are plotted again in Figure 7.4, this time along with the corresponding fits from the Méheust model. As one can see from the figure, only a limited number of points around the peaks are plotted. This is due to another aspect of the model, in which you can choose the range of data points considered for the fit (a fitting window). Varying the range provides a nice way to estimate the uncertainties of the fitted parameters due to two effects: The first effect is a possible deviation between the data profile and the model used to fit it. If the assumed ODP's functional form does not fit very well with the data, the obtained parameters will depend on the range chosen for the fit. Moreover, as ϕ moves away from the maximum peak values, the intensity decreases to the noise level of the diffraction profiles. Thus, the points in the flat sections between the peaks in Figure 7.4 are really of little relevance when fitting the model to the data [33].

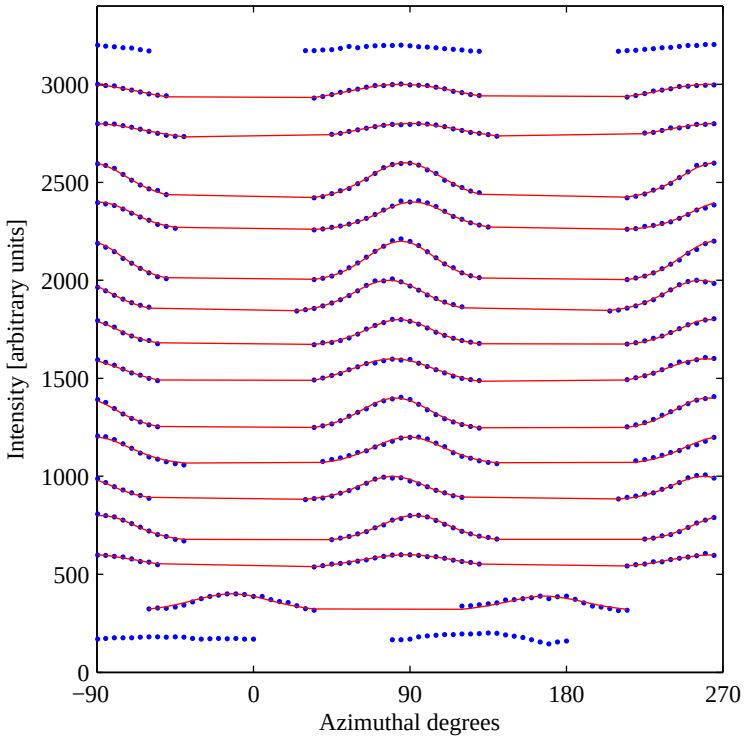

FIGURE 7.4: The azimuthal profiles and corresponding fits in the nematic phase. The data points are shown as blue dots, while the fits are red lines. The profiles just above and below the nematic phase are also included, just to show that these are too isotropic to be worth considering.

TABLE 7.1: The results from fitting the azimuthal profiles.

h	Θ_0	Φ_0	m	S_2	geom.
30 mm	30.11 ± 6.15	173.52 ± 0.15	1.70 ± 0.08	0.37 ± 0.01	anti-nem.
29 mm	36.70 ± 4.30	-2.64 ± 0.59	2.63 ± 0.16	0.51 ± 0.02	anti-nem.
28 mm	13.57 ± 0.71	176.31 ± 0.09	3.82 ± 0.15	0.63 ± 0.01	anti-nem.
27 mm	16.43 ± 1.92	-179.30 ± 0.10	4.63 ± 0.22	0.68 ± 0.01	anti-nem.
26 mm	9.39 ± 2.29	174.71 ± 0.04	4.68 ± 0.55	0.68 ± 0.03	anti-nem.
25 mm	12.73 ± 0.76	167.01 ± 0.13	4.21 ± 0.10	0.66 ± 0.01	anti-nem.
24 mm	15.98 ± 3.06	-7.08 ± 0.02	4.75 ± 0.23	0.69 ± 0.01	anti-nem.
23 mm	4.87 ± 2.96	-10.03 ± 0.09	2.80 ± 0.50	0.52 ± 0.06	anti-nem.
22 mm	4.34 ± 1.69	-8.73 ± 0.13	4.24 ± 0.35	0.66 ± 0.02	anti-nem.
21 mm	13.95 ± 2.73	-1.61 ± 0.28	3.97 ± 0.27	0.64 ± 0.02	anti-nem.
20 mm	12.34 ± 3.56	-10.86 ± 0.05	4.67 ± 0.32	0.69 ± 0.02	anti-nem.
19 mm	8.77 ± 3.01	2.12 ± 0.04	4.22 ± 0.12	0.66 ± 0.01	anti-nem.
18 mm	45.69 ± 4.35	-3.78 ± 0.56	3.92 ± 0.68	0.63 ± 0.06	anti-nem.
17 mm	22.33 ± 1.08	-12.90 ± 0.40	3.56 ± 0.36	0.51 ± 0.05	nem.

The fits shown in the figure are rather good, which indicates that the parameters calculated from the fits should also be good. The reason why only the fits in the nematic phase are shown is that these are actually the only fits worth considering. The Méheust model assumes an anisotropic orientation distribution. Using the model to fit profiles that are isotropic, or very weakly anisotropic, is like forcing your right-hand glove onto your left hand, quite pointless. The fits would be bad, and the parameters meaningless.

7.2.2 Parameters obtained from the fit

The values obtained for each profile in the nematic phase are presented in Table 7.1. The uncertainties were found by the method already described: we varied the fitting window around the peaks between 30 and 95 points (half width) in steps of five, and calculated the standard deviation from the formula

$$\sigma = \sqrt{\frac{1}{N-1}\sum_{i=1}^{N}(x_i - \overline{x})}\,. \tag{7.9}$$

The computed values for Φ_0 and Θ_0 shown in the table are interesting enough, but what we are really interested in is the mean orientation of the particle director relative to the vertical. For the nematic geometry this can easily be found by taking the dot product of the reference orientation $\boldsymbol{n}_0$ (Equation (7.8)) and $\hat{\boldsymbol{z}}$. For the anti-nematic geometry we must account for the fact that the particle director is in fact perpendicular to the reference orientation, i.e. $\Phi_0 \longrightarrow (\Phi_0 + \pi/2)$. The angle

between the mean particle director and the vertical is then given by

$$\arccos\left(\cos\Theta_0 \cos\Phi_0\right) , \qquad \text{nematic} \tag{7.10}$$

$$\arccos\left(\cos\Theta_0 \sin\Phi_0\right) , \qquad \text{anti-nematic.} \tag{7.11}$$

The results computed from the above equations are shown in Figure 7.5 as a function of height.

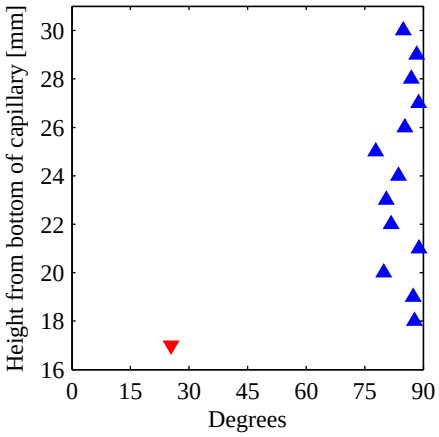

FIGURE 7.5: Mean orientation of the particle director in the nematic phase, in degrees from the vertical. ▲ means the anti-nematic distribution has been used to fit the data, ▼ means nematic. The uncertainty is shown only where it is larger than the symbol.

The orientations presented in the figure confirm our earlier assumption that we have a nematic layer below the anti-nematic region, although the exact value for the nematic orientation is a bit surprising. Whereas the mean director orientations of the particles in the anti-nematic region are all quite close to the horizontal (within 13°), the orientation of the mean nematic director is 26° off the vertical. Both the capillary and the NaFh particles have a symmetry that at first glance should make such an angle highly unlikely. Though if we assume that our X-ray beam is not completely centred in the capillary, we could also be observing an effect of the glass walls that would account for such an orientation. We will discuss this further in the next section.

In addition to the mean orientation of the particles, we are also interested in the degree of ordering. A measure of this is the nematic order parameter, which we have plotted in Figure 7.6. Although we have no real references in the isotropic/sediment regions, the results indicate that S_2 decays toward zero above and below the nematic phase. This is as expected. If we disregard the deviating point at $h = 23\,\text{mm}$, the order is also remarkably consistent in the ten measurements from

18 to 28 mm. An arithmetic mean of the order parameter in this region gives a value of $S_2 = 0.66 \pm 0.03$.

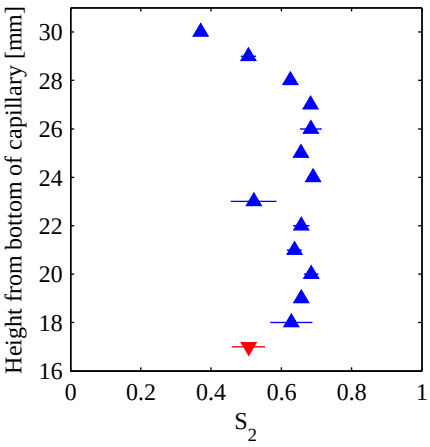

FIGURE 7.6: The calculated nematic order parameter in the nematic phase. ▲ means the anti-nematic distribution has been used to fit the data, ▼ means nematic. The uncertainty is shown only where it is larger than the symbol.

It would be nice to combine the information of Figures 7.5 and 7.6. That way we would have both the preferred orientation of the particles, and the spread around the orientation. We do this by looking at the ODP and the obtained values for m. From the definition of the distribution we can find the fraction x of the particles that are contained in an interval $[0,\ \alpha_0]$ about n_0:

$$\frac{2\pi \int_0^{\alpha_0} C \exp(m\cos^2\alpha)\sin\alpha \, d\alpha}{2\pi \int_0^{\pi/2} C \exp(m\cos^2\alpha)\sin\alpha \, d\alpha} = x\,. \tag{7.12}$$

Due to the symmetry of the NaFh particles, all particles are contained within $\alpha = \left[0,\ \pi/2\right]$, so the denominator is included for normalization.

Equation (7.12) is not solvable analytically, but it is easily solved numerically using MATLAB. We chose $2/3$ as a suitable value for x and performed the integrations. The result is shown in Figure 7.7. In our opinion, this is the essential information that can be extracted from the WAXS images. We now have *both* the mean orientation of the particles in the nematic phase *and* the spread about the mean.

Two comments about Equation (7.12) should be made. We have used the nematic version of the Maier Saupe distribution (Equation (7.5)) to find the spread

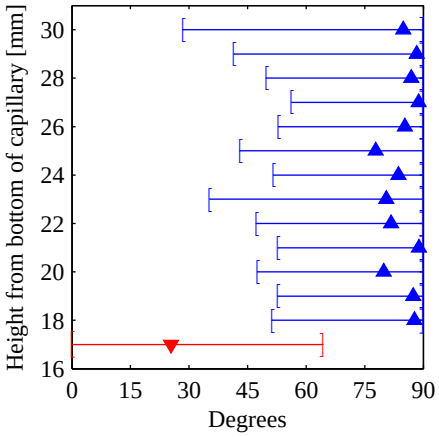

FIGURE 7.7: Mean particle orientation with the spread in the distribution shown as an interval around the mean orientation. Two thirds of the NaFh particles have their orientation within the intervals. As previously, ▲ means anti-nematic distribution, ▼ means nematic.

in orientation for both the nematic and anti-nematic geometries. This is justified because looking at $\exp(m \sin^2 \alpha)$ from $\pi/2$ to 0 is really the same as looking $\exp(m \cos^2 \alpha)$ from 0 to $\pi/2$. Secondly, as α is limited to the range $[0, \pi/2]$ for our sample, any values outside this region can be folded back into the correct range. This is the reason for the asymmetric intervals in Figure 7.7.

7.3 Discussion

7.3.1 Observations with other experimental techniques

As already mentioned, the phenomenon of a nematic layer bordering the anti-nematic phase has been observed previously in the same kind of system, but it has, to our knowledge, never been discussed properly in the literature. We will here present observations from MRI and birefringent light studies as confirmations that the layer exists.

An MRI image of a NaFh–water–salt suspension is shown in Figure 7.8. The diameter of the sample tube is 10 mm, and, the sample contains 3 % NaFh and 1×10^{-4} M NaCl. Uniaxial nematic geometries at the top and bottom of the nematic phase is clearly visible in the leftmost image. In diffusion MRI, an area with larger signal amplitude indicates an area with less diffusion along the gradient direction. Disregarding for the moment the additional nematic layer at the top of the nematic phase, the images in Figure 7.8 are therefore a nice confirmation of our WAXS analysis. In the leftmost image, the diffusion gradient is along the vertical, and the

two bright areas are areas where water diffusion is slow. Obviously, with a vertical gradient, the diffusion paths through a layer of particles laying down should be considerably more tortuous than in areas where diffusion is parallel to the platelet faces [94]. The situation in the middle and right images are opposite. Here, the diffusion gradients are horizontal and the water can diffuse parallel to the NaFh disks in the nematic layers. In the anti-nematic area though, a large fraction of the standing particles are in the way of the water, and signal is high.

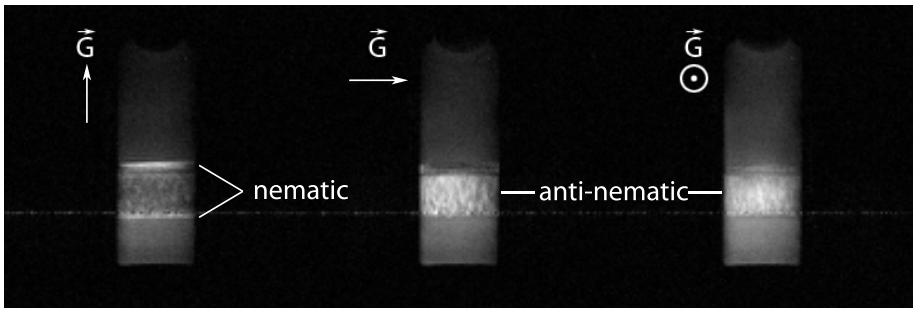

FIGURE 7.8: Diffusion-weighted MRI images of the nematic phase in a NaFh sample. The gradient is indicated on each image. We thank Eduardo Novais de Azevedo for permission to use the image.

The fact that two uniaxial nematic layers are visible in Figure 7.8 requires a little more attention. Nils Ivar Ringdal at NTNU has performed birefringence studies of the same system and has found that whether one, two or none nematic layers are formed is dependent on a range of factors. Further experiments must be done before a complete understanding is reached, but it seems that the grain size of the NaFh, the concentrations of NaFh and salt, and the sample geometry is important [28].

An example of Ringdals's birefringence images is shown in Figure 7.9. A brief outline of the experimental setup is as follows: The sample was placed between crossed polarizers and the image recorded with a PC-controlled CCD-camera. If the sample is isotropic, no light will pass the analyzer and the image is black. If, on the other hand, the sample is anisotropic, the polarization is changed by the sample, and light will come through. By altering the alignment of either the crossed polarizers or the sample, the orientation of the clay particles can be determined. The particular sample shown in Figure 7.9 consisted of 2 w/w % NaFh and 1×10^{-3} M NaCl. In addition to the sediment, three separate strata of nematic phases can be observed in the figure. The layer of horizontally aligned particles between the sediment and nematic is indicated with an arrow. Notice also the slight tendency of a bright birefringent line between the two middle strata.

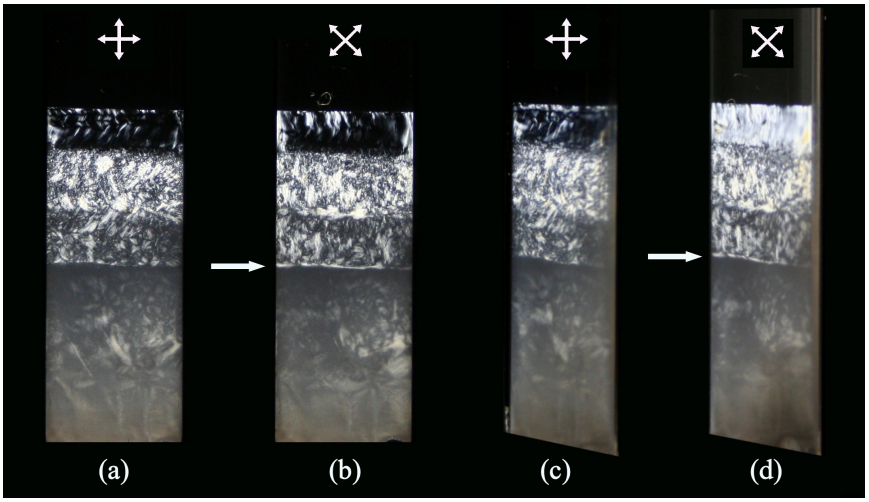

FIGURE 7.9: A sample of NaFh dispersed in saline water, imaged between crossed polarizers. **a)** The axes of the crossed polarizers are oriented parallel and perpendicular to the edges of the sample tube. **b)** A birefringent line at the isotropic-nematic boundary appears brightest when the axes of the crossed polarizers are oriented at 45 degrees to the vertical. Hence, the particles in this layer are oriented with their director either parallel or perpendicular to the sample tubes. **c)** Same cross-polarizing configuration as the first picture, but the sample is rotated 45 degrees. No birefringent boundary line appears. **d)** The birefringent line appears when both the sample and cross-polarizers are rotated 45 degrees, meaning that the particles at the boundary are lying face down. We thank Nils Ivar Ringdal for permission to use the image.

7.3.2 Orientation in the nematic layer revisited

We now return to Figure 7.5 and the mean orientation of the particles in the nematic layer. Since the NaFh particles are assumed to be symmetrical about their director, and the sample holder is a circular capillary, there ought to be no reason why the particles are tilted to the left instead of right in the centre of the capillary. A mean orientation 26° away from the vertical combined with a mean Φ_0-value of $-13°$ can on the other hand be explained as an effect of alignment. Previous MRI studies of similar NaFh samples has shown that with polar walls around the sample (e.g. glass), the platelets are anchored face-to-wall in a region close to the walls [94]. This effect is stronger than the one previously predicted by Harnau et al. [95] for purely hard wall interactions. If we assume the particles are lying completely horizontal in the centre of the capillary, a transition from vertical to horizontal alignment must therefore take place as we move from the wall to the centre. A schematic representation of this is shown in Figure 7.10. The illustration must in no way be misinterpreted as a real representation of the uniaxial nematic

layer. It is merely an attempt to qualitatively explain the results.

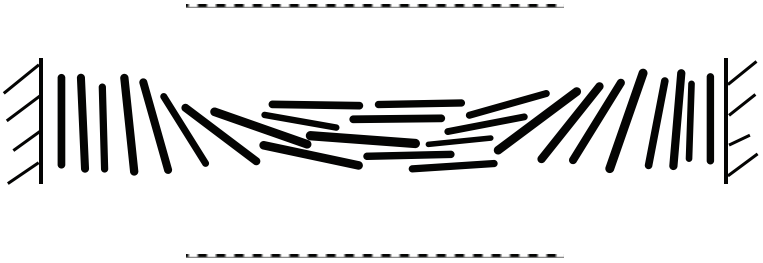

FIGURE 7.10: Schematic representation of the alignment in the uniaxial nematic layer. A transition from vertical to horizontal to vertical is assumed as we move radially from one wall to another.

Remember that our capillary has a 2 mm diameter, and that the size of the X-ray beam is 0.3×0.3 mm. Assuming then that Figure 7.10 has some truth in it, an off-centre alignment of the capillary with respect to the incoming beam could explain why the mean orientation of the platelets in the uniaxial nematic layer is not completely horizontal.

On closer inspection, the assumption of a vertical to horizontal transition is actually supported in the MRI images in Figure 7.8. The face to wall anchoring in the top uniaxial nematic layer is clearly visible both in the centre and right images. In the centre image it is seen as a higher signal amplitude close to the edges, while in the right one it is visible in the middle. The difference between the two images is a result of the gradient direction. In the centre it is the platelets anchored at the left and right edges that are perpendicular to the diffusion gradient, while in the right it is the platelets closest to- and farthest from the observer. The diameter of the sample holder in Figure 7.8 is 10 mm, so with respect to the diameter we would expect the face-to-wall region to make up a larger part of our 2 mm diameter sample.

Chapter 8

Concluding remarks

In this experiment we performed wide angle synchrotron X-ray scattering studies of NaFh dispersed in water containing 1×10^{-3} M NaCl. The dispersion was contained in a 2 mm diameter glass capillary that was scanned vertically in steps of one millimeter. Integrating the two-dimensional WAXS images radially and extracting azimuthal profiles of the (001) peak revealed an anisotropic region approximately 14 mm high. The spontaneous formation of this *nematic gel* region is in agreement with previous studies of the same sample type [27].

By assuming that the orientational distribution of the particles only depends on one orientational angle, and that the shape of its dependence on that angle is well described by a classical Maier-Saupe form, we were able to determine the mean orientation the particles in the nematic gel, as well as the degree of ordering. To fit the azimuthal profiles we used a model developed by Méheust et al. [33]. In agreement with previous WAXS studies [30], the orientational order in the nematic phase was found to be remarkably uniform. An arithmetic mean of 10 of the measurements in the centre of the nematic region gave 0.66 ± 0.03 as the value of the nematic order parameter.

At the bottom of the nematic-gel region we observed a layer where the NaFh particles have the mean preferred orientation of the particle director close to the vertical. This layer has a completely different geometry from the rest of the nematic phase. In what we have called the anti-nematic or biaxial nematic region (the nomenclature in the literature is confusing here) the particle directors have their preferred orientation close to the horizontal, but the directors are in general not parallel to each other. The ordering in the bottom uniaxial nematic layer is therefore higher than in the rest of the nematic gel.

A layer of horizontally oriented particles either below or above the anti-nematic region has previously been observed both in MRI experiments and by visual inspection of birefringence. To our knowledge though, the order and mean orientation of

the particles in these layers have never been investigated. We found the nematic order parameter to be 0.51 ± 0.05 and that the mean orientation of the particle directors were 26° off the vertical.

A suggestion for future synchrotron experiments is to perform lateral scans of the uniaxial nematic layer. This would reveal the radial transition from a face-to-wall orientation to a horizontal alignment. Such an experiment could therefore confirm that the deviation from a purely horizontal orientation found in our experiment is in fact due to an off-centre alignment of the sample capillary. Also, a more detailed vertical scan around the isotropic/nematic transition should give additional information both on the thickness of the nematic layer and the transition from nematic to anti-nematic geometry.

The WAXS results presented here, combined with MRI imaging and visual inspection of birefringence, has been compiled by the current author into an article intended for submission to Langmuir. Although not yet completely finished, the article is included in Appendix B. In the introductory chapter there, the interested reader can find references to articles attempting to explain the occurrence of the exact phenomenon discussed above: the formation of layer of horizontally aligned particles in the isotropic-nematic transition. As we only became aware of these papers when the deadline of this thesis neared, the references were included in the preparation of the article, but the topic was not properly discussed in the previous chapter.

Appendix

Appendix A

MATLAB code

In this chapter we have included the MABLAB code used for profile extraction from the MRI images. The usage of the code was discussed in detail in Section 3.1.2.

A.1 Profile extraction

```
%-----------------------------------
%CLEARING AND DEFINING VARIABLES
%-----------------------------------
clear
%imagedimensions
xdim=256;
ydim=256;
%input configuration
numberoffiles=1;
startfile=13;
directory= 'C:\Master\Data\Velocidade 90 6x3cm\veloc90_axial\';
batchname= 'image';
fileending= '.txt';
%threshold for profile extraction; a point larger than
%   (signal-noise)*treshold is chosen as a profile point
threshold=0.5;
whatisone=10;
%the points defining the profile (to remove edge points)
startprofile=22;
endprofile=215;
%other variables
imagemat=zeros(xdim,ydim);
colmax=zeros(xdim,1);
```

```
%-------------------------
%STARTING BATCH ITERATION
%-------------------------
for batchvar=startfile:numberoffiles+startfile-1

    %IMPORTING FILE
    filename = [directory, batchname, int2str(batchvar), fileending];
    file=load(filename);

    %PLACING IMAGE IN THE MATRIX IMAGEMAT
    %the indeces of imagemat is like the image viewed in a x-y-plane
    %i.e. x(=first index) growing from left to right, and
    % y(=second index) from bottom to top

    for fileit=1:ydim*xdim-1
        imagemat(file(fileit,1)+1,file(fileit,2)+1)=file(fileit,3);
    end
    imagemat(1,ydim)=imagemat(2,ydim);


    %NORMALIZING THE DATA
    %Setting the smallest value to be zero
    smallestvalue=min(min(imagemat));
    imagemat=imagemat-smallestvalue;
    %setting the median whatisone-th largest column value to be one
    for j=1:xdim
        tempcolsort=sort(imagemat(j,:));
        colmax(j)=tempcolsort(ydim-whatisone);
    end
    largestvalueinv=1/(median(colmax));
    imagemat=imagemat.*largestvalueinv;

    %finding average backgroundnoiselevel from the top five rows
    avnoise=0;
    for i=1:xdim
        for j=1:5
            avnoise=avnoise+imagemat(i,ydim-j);
        end
    end
    avnoise=avnoise/(5*xdim);
    limit=threshold*(1-avnoise)+avnoise;

    profile=zeros(xdim,1); %introducing profile vector
    %FINDING PROFILE
    for i=1:xdim
        found=false;
         for j=ydim:-1:18 %moving down from y=ydim
            if imagemat(i,j)>limit %i.e. if we are at a point > limit
                temp=0;
```

```
                %check if the next two > limit
                if (imagemat(i,j-1)>limit) && (imagemat(i,j-2)>limit)
                    %checking the next 15
                    for k=1:15
                        if imagemat(i,j-k)<limit
                            temp=temp+1;
                        end
                    end
                    %if no more than 2 of the next 15 < limit, found
                    if temp<3
                        found=true;
                        break
                    end
                end
            end
        end
        if found==true
            profile(i)=j;
        end
    end
%%
    %SAVING PROFILE TO FILE
    savefilename= [directory, batchname ,int2str(batchvar), '.mat'];
    profilepart=profile(startprofile:endprofile);
    %save(savefilename, 'profilepart')

    %PLOTTING PROFILE AND IMAGE
    figure(batchvar)
    subplot(2,1,1)
    plot(profile)
    title('Profile')
    xlabel('\thispagestyle{empty}x [pixels]','interpreter','latex')
    ylabel('height [pixels]','interpreter','latex')
    axis([1 xdim 80 200])

    subplot(2,1,2)
    image(imagemat(:,200:-1:80)'.*50)
    title('Recorded image')
    xlabel('x-pixels','interpreter','latex')
    ylabel('y-pixels (inverted)','interpreter','latex')

%%
end%END OF BATCH ITERATION

%-------------
%END OF FILE
%-------------
```

Appendix B

Journal article

In this appendix we include an article based on the results in Part II. The article is currently being finalized and includes some theory and results that were not discussed in the main part of the thesis. In addition to the people previously mentioned, Elisabeth Hansen and Kenneth D. Knudsen has contributed. Elisabeth is currently writing her Master's thesis at NTNU, whereas Kenneth is a senior scientist at IFE, Kjeller, who took part in the synchrotron experiment in Grenoble.

The article is included in the state it was in at the time this thesis was submitted, and is styled in the submission template of Langmuir.

Experimental studies of the isotropic-nematic interface in suspensions of Na-fluorohectorite synthetic clay.

H. Hemmen(a), N. I. Ringdal(a), E. N. De Azevedo(b), E. L. Hansen(a), J.O. Fossum(a), M. Engelsberg(b), Y. Mehéust(c) and K. D. Knudsen(d).*

(a) Department of Physics, The Norwegian University of Science and Technology, Hoegskoleringen 5, N-7491, Trondheim, Norway, **(b)**Programa de Pós-Graduação em Ciência de Materiais and Departamento de Física, Universidade Federal de Pernambuco, 50670-901 Recife, Pernambuco, Brazil. **(c)**Geosciences Rennes, UMR CNRS 6118, Université de Rennes 1, Rennes, France. **(d)**Physics Department, Institute for Energy Technology (IFE), Kjeller, Norway

*jon.fossum@ntnu.no

RECEIVED DATE (xx.xxx 2008)

TITLE RUNNING HEAD: Interface regions in NaFh suspensions.

ABSTRACT: *Colloidal dispersion of the synthetic clay Na-fluorohectorite in saline water exhibits coexisting isotropic and nematic phases, due to gravitational separation of the polydisperse particles. We study the ordering of the NaFh platelets in the isotropic-nematic interface, where a sharp horizontal layer appears. We utilize three completely different experimental techniques: Visual observation of birefringence, Magnetic Resonance Imaging and synchrotron Wide Angle X-ray Scattering. In agreement with theory and earlier studies of similar systems, we find that the particles are lying horizontally, i.e. with the mean particle director along the vertical.*

APPENDIX B JOURNAL ARTICLE

KEYWORDS: Nematics, Clays, Interface, Birefringence, MR Imaging, WAXS, Synchrotron, I-N transition.

BRIEFS: Experimental observations of ordering in the isotropic-nematic interface in aqueous NaFh suspensions.

1. Introduction

Clays are fascinating materials that are readily available and present almost everywhere on earth. Even without other knowledge about clay than having played with it as a child, it is obvious that clay has some amazing properties. Wet clay is soft and easily shaped by hand, but retains the form you give it if it is left alone. If clay is baked, it becomes hard as rock, showing completely other properties than it did before. Although clays have been studied for centuries by geologist, geo-chemists and others, the fundamental studies of complex physical phenomena in clays is a relatively new field [1]. In recent years, the presence of orientational order in clay suspensions have been documented by optical measurements [2][3] showing visual nematic textures. Neutron- [4] [5] [6] and X-ray - scattering [7] [8] [9] [10] as well as Magnetic Resonance Imaging (MRI) experiments [11][12][13][14][15][16] have all revealed structural correlations with nematic order.

A spontaneous transition from an isotropic (I) phase to a nematic (N) phase was found in early investigations of other systems such as vanadium pentoxide (V_2O_5) [17] and tobacco mosaic virus (TMV) [18][19], as well as suspensions of various rod-like nanoparticles [20]. An explanation of this behavior, considering purely repulsive short range interactions, was first made by Onsager in the 1940s [21]. Onsager modeled the phase transition considering the competition between the orientational and the packing entropies of the colloidal system, thus concluding that at a sufficiently high particle concentration, the packing entropy dominates and it becomes favorable for the particles to order in

nematic alignment. As Onsager proposed and later confirmed by computer simulations [22] [23], nematic ordering can occur for plate-like particles that are fairly anisometric.

Although there is still no complete theory for the process of orientational ordering in the gel structure, an I-N phase transition in sols of clay particles was observed by Langmuir already in 1938 [24], and this has been the focus of much recent work[25][20] [26][8]. An entropy-driven I-N transition has also been studied experimentally and theoretically in suspensions of both sterically stabilized [27] and charge stabilized colloidal platelets [28]. Recently, van der Beek et al. [29] have studied interfacial phenomena in a colloidal dispersion of sterically stabilized gibbsite platelets. These dispersions exhibit coexisting isotropic and nematic phases, as has also been observed in clay suspensions [8]. Furthermore, the authors found that nematic and isotropic phases were separated by a sharp horizontal interface, which has previously been predicted theoretically by applying the Zwansig model [30]. By comparing the nematic order of long and short thin rods in the isotropic-anisotropic coexistence phase with the nematic order parameter of freely rotating platelets near a hard wall, the authors conclude that the nematic phase can be considered as a wall, creating a corresponding depletion zone in the adjacent isotropic phase. Density functional theory calculations by Harnau et al [31] on fluids consisting of thin-hard platelets and rods in contact with a hard wall, have shown that particles lying very close to the wall must adopt a near fully parallel alignment due to interactions with the wall. Hence, for anisotropic clay nanoparticles at correct densities, we expect interface regions at the isotropic-nematic transitions where the particles align with their faces parallel to the nematic phase boundary.

In the present manuscript, we present experimental evidence of such a layer in suspensions of synthetic 2:1-layered smectite clay Na-fluorohectorite (NaFh) in aqueous NaCl solution with varying concentrations. In the gravitational field, a suspension of NaFh may be effectively separated into different strata of gels, sols and sediments[7][8]. In the interface regions between the nematic and isotropic phases, a nematic transition layer where the particles are lying face down is found, both between the isotropic gel and nematic phase, and between the nematic phase and isotropic sol. The

observations were done using three experimental techniques: Magnetic Resonance Imaging, synchrotron wide angle X-ray scattering, and visual inspection of birefringence.

2. Experimental details

2.1 Materials

Synthetic fluorohectorite clay was purchased in powder from Corning Inc., New York. Hectorite, a 2:1-layered clay, is composed of a layer of octahedra, sandwiched between two layers of silicon tetrahedra. What separates fluorohectorite from regular hectorite is that the hydroxyl groups have been substituted with fluorine ions (F^-). The purchased fluorohectorite powder was ion exchanged through dialysis to produce NaFh having the nominal chemical formula $Na_{0.6}Mg_{2.4}Li_{0.6}Si_4O_{10}F_2$.[32] A more thorough description of this process can be found in Ringdal et al. [33] and Méheust et al.[34].

As shown in **Figure 1**, the individual NaFh particles are composed of around 20-100 silicate lamellae [8] that stack by sharing Na+ ions between their basal plane. NaFh represents an extreme in particle size and layer charge within the smectite group. It has a particle size of up to 20 000 Å with a layer charge of $1.2e^-$ per unit cell[35]. The large layer charge originates from the substitution of Li^+ for Mg^{2+} in the octahedral layer, and cause the platelets to remain stacked when suspended in water, as opposed to laponite and montmorillonite that exfoliate into single layers in aqueous solutions[36] [37]. From AFM imaging (**Figure 1**), we know the polydisperity in particle size is quite large with highly variable particle morphology. Hence, in a suspension in water, gravitational forces effectively sort the particles by size, stabilizing in some cases several strata of gels, sols and/or sediments within a single sample tube[7].

2.2 Experimental Methods

Sample holders

We used both rectangular and cylindrically shaped tubes as sample holders. The geometry of the sample holder has been shown to be important due to the coupling between the clay molecules and polar walls [16][31]. For the birefringence studies we used the 10 cm long, 1 cm wide and 1 mm thick rectangular

Vitrotube 4410-100 from VitroCom. A cylindrically shaped thin walled capillary tube from Hilgenberg was used for the WAXS study. This tube had 2mm diameter, and 1μm wall thickness. For the MRI experiments, we used a 10 mm-diameter common glass tube with 0.2 to 0.3 mm walls. The sample cells are shown in **Figure 2.**

Experimental setup Birefringence

The visual Birefringence studies were done at the Norwegian University of Science and Technology (NTNU), Norway, and the experimental setup is shown in **Figure 3**. The sample was placed between crossed polarizers and the image recorded with a PC-controlled CCD-camera. If the sample is isotropic, no light will pass the analyzer and the image is black. On the other hand, if the sample is anisotropic, the polarization is changed by the sample, and light will come through. By altering the alignment of either the crossed polarizers or the sample, the orientation of the clay particles can be determined. We have recently submitted a paper where a thorough study of birefringent patterns in the nematic phase of Na-fluorhectorite is performed using this method [33].

Experimental setup MRI

The MRI experiments were performed at the Federal University of Pernambuco, Brazil. To record MR Images, an MRI system (Varian Inova), including a 2.0 T magnet with a 30 cm bore, was employed. We used the MRI-setup to record diffusion-weighted images. In diffusion MRI, an area with larger signal amplitude indicates an area with less diffusion along the gradient direction, and the diffusion-weighted contrast was achieved using a Stejskal-Tanner [38] pulse sequence in conjunction with a standard spin-echo imaging sequence. We used gradients with amplitude of G= 0.15 T/m and the imaging parameters were 50 mm × 50 mm field of view, 64 × 64 imaging matrix and 4 mm slice width.

Experimental setup Synchrotron WAXS

The X-ray scattering experiment was done at the Swiss-Norwegian Beamline (BM1A) at the European Synchrotron Radiation Facility (ESRF) in Grenoble, France. The 2 mm capillary was mounted on a custom made sample holder, and was translated vertically in steps on 1 mm. At each step the scattered

intensity was recorded with a two-dimensional mar345 detector. The monochromatic beam at a wavelength of lambda=0.8089 Å was slit collimated down to 0.3 mm × 0.3 mm, and the sample-to-detector distance and parameters of the detector were calibrated using a standard LaB_6 sample.

3. Results

3.1 Results: Birefringence observations

In a recent work [33] we have studied the effect of different salt concentrations on the phase behavior of Na-fluorhectorite, and the birefringent nature of the nematic ordering. In many of the samples considered, there have been observations of separate interface regions with different particle orientation at the phase boundaries, see **Figure 4**. In particular, visual observations of the boundary between the lower isotropic phase and middle nematic phase indicate an interface region where the particles are laying face down, as shown in **Figure 5.** In addition to this, some samples have shown several interfaces between individual nematic phases and between the upper nematic and isotropic phase. **Figure 6** shows the changes in birefringence that occur in the upper nematic phase during rotation of the sample and polarizers. When the sample is viewed from the front, most of the upper nematic phase appears black in any angle of the cross-polarizers. When the sample is turned around 45 degrees with the axes of the polarizers rotated 45 degrees, the whole phase becomes birefringent. This means the particles in the black region are oriented with their faces against the walls, i.e. homeotropic alignment. As seen in pictures **b)** and **c)** of **Figure 6,** a birefringent line appears at the transition to the upper isotropic phase when the polarizers make an angle to the axis of the sample tube. The line is brightest when the angle is 45 degrees, which means the particles at the nematic-isotropic boundary are either standing or lying with their edges towards the walls. However, due to the low contrast between the nematic phase and the interface region in **Figure 6**, an unambiguous conclusion with regards to particle orientation (flat or vertical) cannot be reached on the basis of optical observations alone.

3.1 Results: Particle orientation and order determined by WAXS.

In order to further investigate the orientation in the interface regions we therefore performed a wide angle X-ray scattering experiment. In **Figure 7 a)**, the azimuthally integrated and normalized (001) rings recorded with WAXS are shown, translated vertically according to the sample-height they were recorded at. On a whole, the anisotropy of the profiles are consistent with earlier studies of the same system, where tree distinct phases are identified [8]: sediment, nematic gel, and isotropic liquid. The peak position of the profiles in the nematic gel is proof that the particles are standing up, i.e. the mean orientation of the particle director lies in the horizontal plane. Unfortunately, the particular sample considered in **Figure 7 a)** was lost, but an image of a similar sample can be found in **Figure 7 b**).

In addition to the three phases mentioned above, an interface region between the sediment and nematic gel is also found, clearly visible in the figure at y~1700. To determine the orientation and order of the particles in this layer, we applied a model recently developed by Méheust *et al.*[37]. By assuming that the orientational distribution of the particles only depends on one orientational angle, and that the shape of its dependence on that angle is well described by a classical Maier-Saupe form, both orientation and order can be inferred from only a single recorded diffractogram. The order and orientation of the entire nematic phase are shown in **Figures 8 and 9** respectively. The uncertainties in these figures were found by varying the fitting window around the peaks between 30 and 95 points (half width) in steps of 5. This provides a nice way to estimate the uncertainties because the obtained parameters will depend on the range chosen for the fit if the assumed ODP's functional form does not agree with the data. In agreement with previous WAXS studies [7], the orientational order in the nematic phase was found to be remarkably uniform. An arithmetic mean of 10 of the measurements in the center of the nematic region gave 0.66 +- 0.03 as the value of the nematic order parameter.

3.2 Results: Confirmations from Diffusion Magnetic Resonance Imaging.

Further confirmations of the particle orientation in the interfaces between the nematic and isotropic phases have been found by MRI-experiments. A diffusion-weighted MRI image of a sample containing

3% w/w NaFh and 1×10^{4} M NaCl in water suspension is shown in **Figure 10**. An interface region with horizontally aligned particles both at the top and bottom of the nematic phase is clearly visible in the leftmost image. In diffusion MRI, an area with larger signal amplitude indicates an area with less diffusion along the gradient direction. Disregarding for the moment the additional transition layer at the top of the nematic phase, the images in **Figure 10** are therefore a nice confirmation of our WAXS analysis. In the leftmost image, the diffusion gradient is along the vertical, and the two bright areas are areas where water diffusion is slow. Obviously, with a vertical gradient, the diffusion paths through a layer of particles laying down should be considerably more tortuous than in areas where diffusion is parallel to the platelet faces [16]. The situation in the middle and right images are opposite. Here, the diffusion gradients are horizontal and the water can diffuse parallel to the NaFh disks in the interface regions. In the nematic gel though, the standing particles are in the way of the water, and the signal is high.

4. Discussion

4.1 Discussion: Particle orientation in the interface regions

The results presented in Section 3.1 indicate that the orientation in the interface region between the isotropic gel and nematic phase is not completely horizontal. Since the NaFh-particles are assumed to be symmetrical about their director, and the sample holder is a circular capillary, there ought to be no reason why the particles are tilted to the left instead of right in the center of the capillary. It can on the other hand be explained as an effect of sample alignment. Previous MRI studies of similar NaFh-samples have shown that with polar walls around the sample (e.g. glass), the platelets are anchored face-to-wall in a region close to the walls [16]. If we assume the particles are completely horizontal in the center of the capillary, a transition from vertical to horizontal alignment must therefore take place as we move from the wall to the center. A schematic representation of this is shown in **Figure 11**. The illustration must in no way be misinterpreted as a real representation of the nematic transition layer. It is

just an attempt to qualitatively explain the results. A synchrotron experiment to verify this assumption is already planned.

Remember that our capillary in the WAXS experiment had a 2 mm diameter, and that the size of the X-ray beam is 0.3 × 0.3 mm. Assuming then that **Figure 11** has some truth in it, an off-center alignment of the capillary with respect to the incoming beam could explain why the mean orientation of the platelets in the transition layer is not completely horizontal. On closer inspection, the assumption of a vertical to horizontal transition is actually supported in the MRI images in **Figure 10**. The face to wall anchoring in the top transition layer is clearly visible both in the center and right images. In the center it is seen as a higher signal amplitude close to the edges, while in the right is visible in the middle. The difference between the two images is a result of the gradient direction. In the center it is the platelets anchored at the left and right edges that are perpendicular to the diffusion gradient, while in the right it is the platelets closest to- and farthest from the observer. Recall that the diameter of the sample holder in **Figure 10** is 10 mm, so with respect to the diameter we would expect the face-to-wall region to make up a larger part of the 2 mm diameter sample holder used in the WAXS experiment.

4.1 Discussion: Origin of the interface region

The previous study done by Ringdal et al [33] has shown that the formation of the interface regions is dependent on the grain size of the clay particles, which again depends on the preparation of NaFh, i.e. the ion exchange, mortaring, milling etc. In many of our samples, a second nematic phase is formed above the first [33], and sometimes several interface layers can be observed between nematic regions showing slightly different orderings.

5. Conclusion

To summarize…

ACKNOWLEDGEMENT: JOF and KK acknowledge the Research Council of Norway for funding through the Nanaomat and Frinat Programs. ME and ENdA acknowledge the Conselho Nacional de

Desenvolvimento Científico e Tecnológico CNPQ. We also acknowledge the staff at SNBL, the creator of Fit2D: Andy Hammersley, Ahmed Gmira for AFM-images, Daví de Miranda Fonsêca for sample holder design and Ole-Tore Buset for technical assistance.

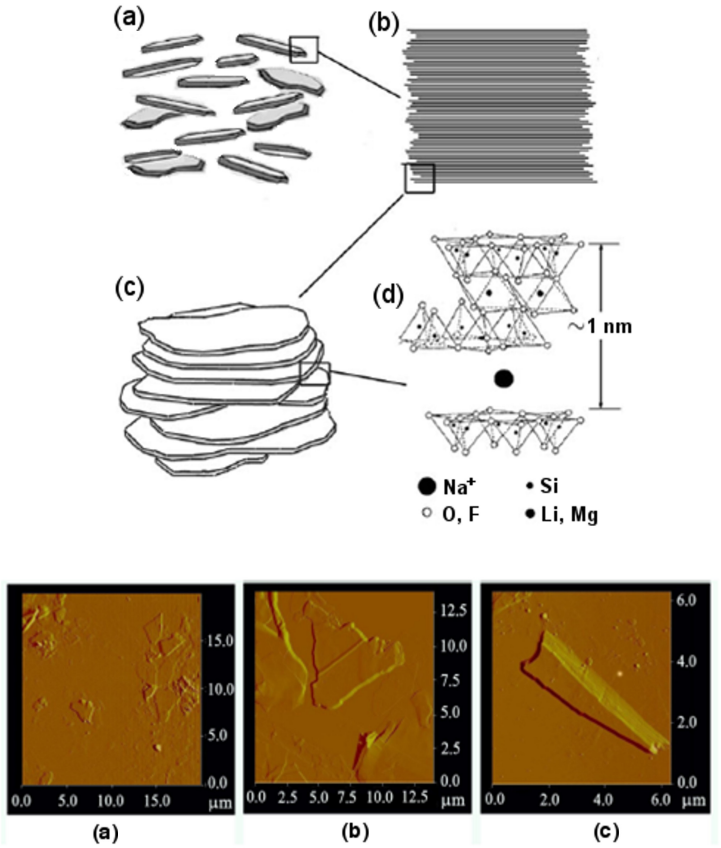

Figure 1. a) Representation of Na-fluorohectorite particles in nematic order. In this illustration the platelets are lying and the director is oriented along the vertical. **b)** Cross-section of a single clay particle, which consists of about 100 crystallized stacked lamellae. **c)** The micron scale lamellae are layered with a thickness of around 1 nm. **d)** Atomic configuration of fluorohectorite, where the intercalated cation is Na+ for NaFh. **e)**, **f)**, **g)** Atomic Force Microscopy images of Na-fluorohecorite particles.

Figure in preparation

Figure 2. The different sample tubes used in the experiments. **a)** Vitrotube 4410-100 from VitroCom **b)** Common glass tube 10 mm diameter **c)** Hilgenberg Mark-tubes, 2 mm diameter.

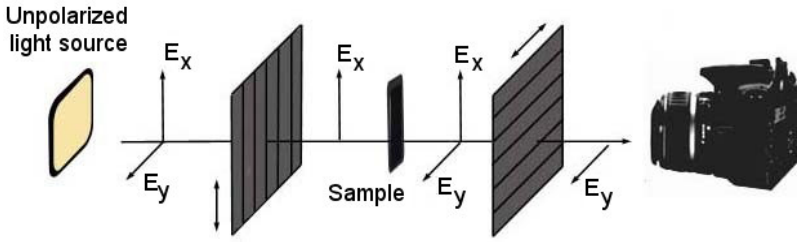

Figure 3. Our simple experimental setup for studiyng the long time sedimentation and phase behavior of the samples, carefully measured by crossed polarizers and a PC-controlled CCD camera.

Figure in preparation

Figure 4. Samples of different salt concentrations are shown, indicating that the interface region occurs for several conditions.

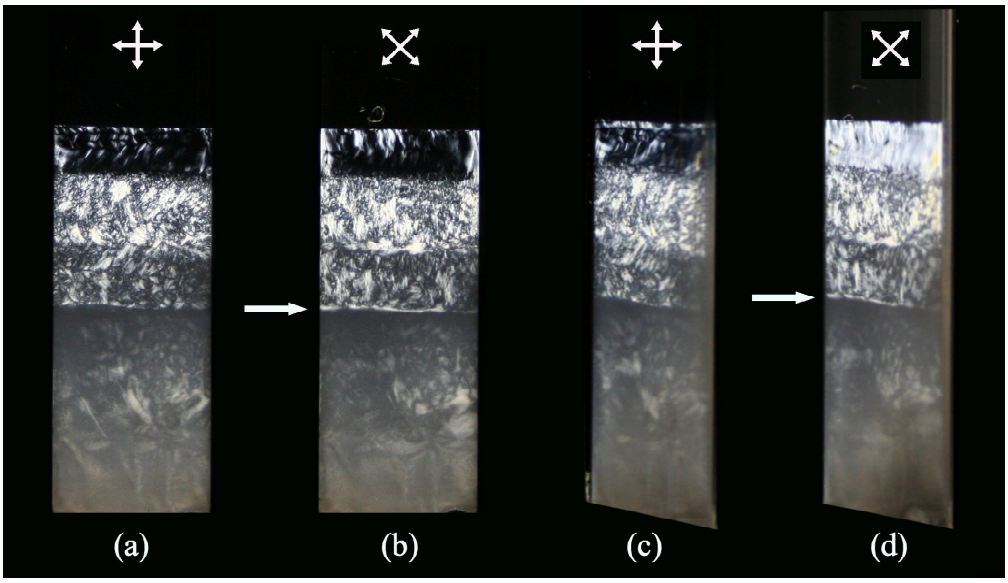

Figure 5: Detection of lying particles at the boundary between the isotropic and nematic phase in a suspension of 2 w/w% NaFh, 1×10^{4} M NaCl. **a)** The axes of the crossed polarizers are oriented parallel and perpendicular to the edges of the sample tube. **b)** A birefringent line at the isotropic-nematic boundary appears brightest when the axes of the crossed polarizers are oriented at 45 degrees to the vertical. Hence, the particles in this layer are oriented with their director either parallel or perpendicular to the sample tubes. **c)** Same crosspolarizing configuration as the first picture, but the sample is rotated 45 degrees. No birefringent boundary line appears. **d)** The birefringent line appears when both the sample and cross-polarizers are rotated 45 degrees, meaning that the particles at the boundary are lying face down.

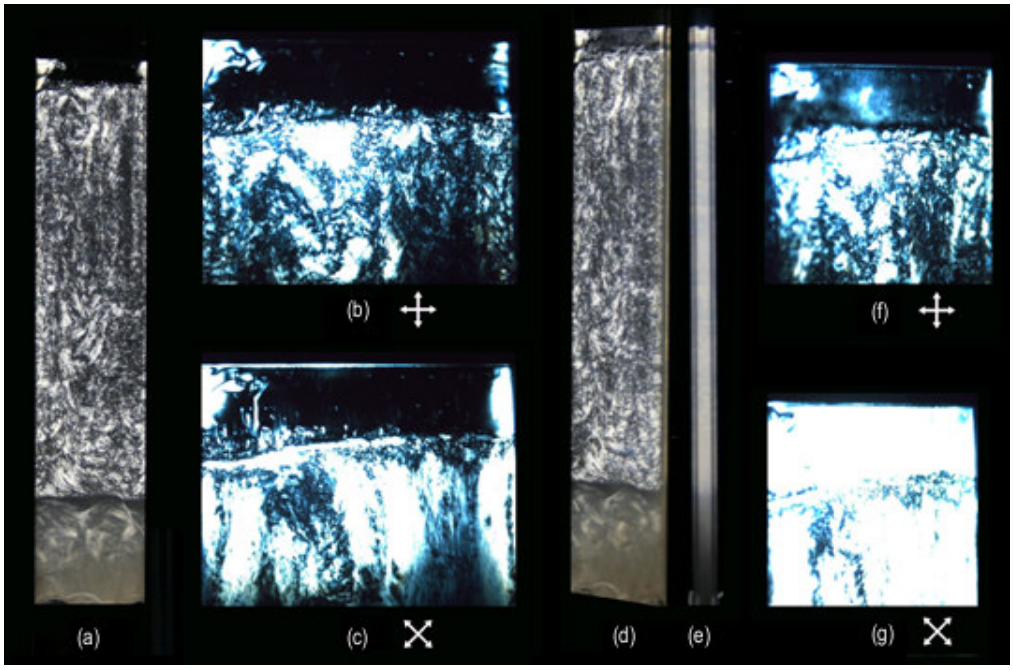

Figure 6: Particle alignment in the nematic sol phase of a 3 w/w% NaFh suspension with salt concentration 10^3 M NaCl. The sample is initially half-filled and the pictures are taken 5 months after sample preparation. **a)** The entire sample. **b)** A close-up microscope picture of the nematic sol, viewed between crossed polarizers with axes parallel to the edge of the sample tube. **c)** With the polarizers rotated 45 degrees, the appearance of a thin birefringent layer above the homeotropic region indicates that the particles in this layer are edge-wall oriented. Moreover, because the birefringence of the layer is most intense at this rotation, the orientation of the particle director is either parallel or perpendicular. **d)-g)** Same as above, but the sample is rotated 45 degrees. **e)** Sample viewed edge on.

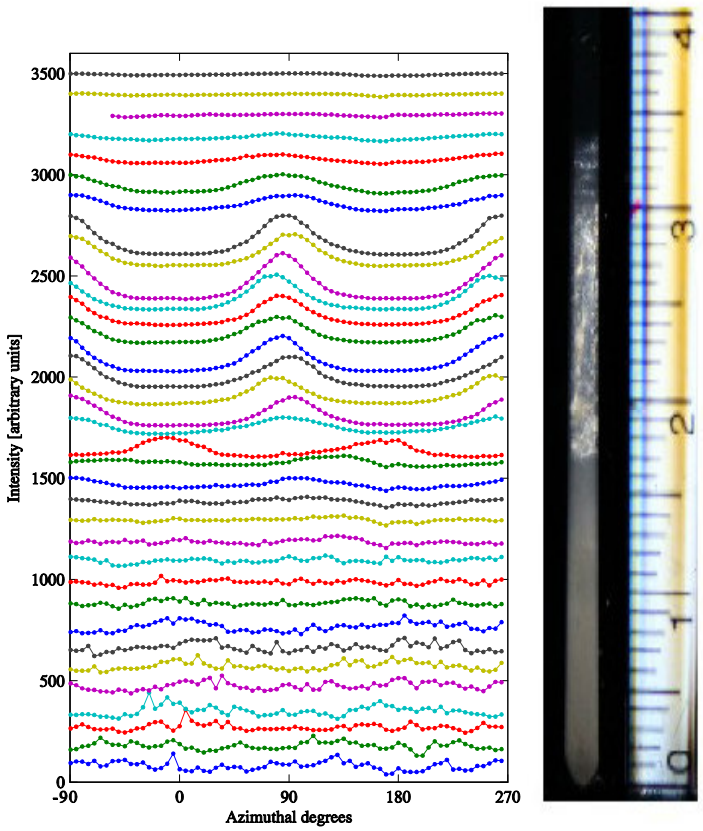

a) **b)**

Figure 7. a) The figure shows the azimuthal profiles for the (001) ring translated vertically according to the height they were recorded at. The distance between each profile is 1 mm, excluding the topmost, which were recorded at the top of the capillary (as a reference). The lowermost profile is the taken 1 mm from the bottom of the capillary. 0º azimuth is along the vertical. **b)** A sample similar to that which the profiles in **a)** were recorded from (same diameter, clay- and salt concentration). The sample is imaged between crossed polarizers, and the identifiable phases in the capillary correspond well to the profiles in the left figure**.**

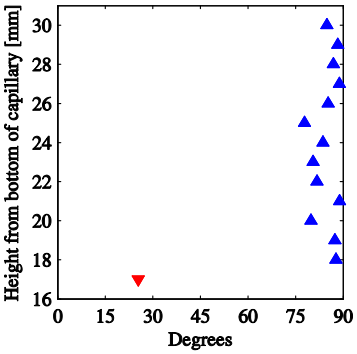

Figure 8: Mean orientation of the particle director in the nematic phase, in degrees from the vertical. ▲ means the ODP function used to fit the data assumes the mean particle director perpendicular to the reference direction. ▼ means an ODP function with parallel mean particle director and reference direction is assumed. The uncertainty is shown only where it is larger than the symbol.

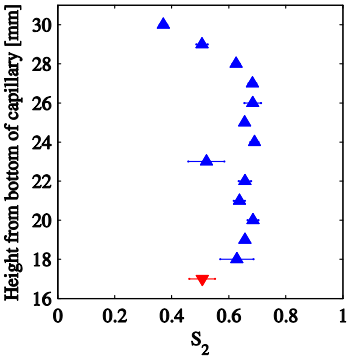

Figure 9: The calculated nematic order parameter in the nematic phase. ▲ and ▼ has the same meaning as in **Figure 8**. The uncertainty is shown only where it is larger than the symbol.

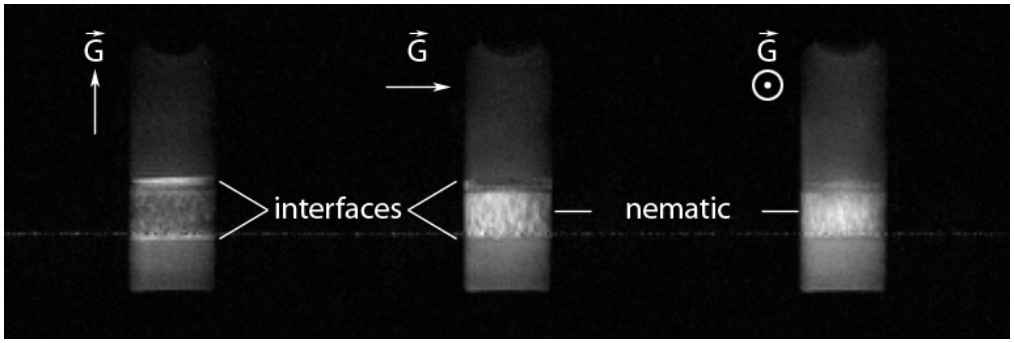

Figure 10: Diffusion-weighted MRI images of the nematic phase in a NaFh-sample. The gradient direction is indicated on each image.

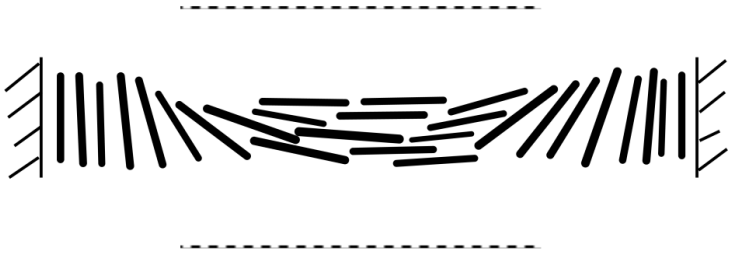

Figure 11: Schematic representation of the alignment in the nematic transition layer. A transition from vertical to horizontal to vertical is assumed as we move radially from one wall to another.

References

[1]. **Fossum, Jon Otto.** *Complex Physical Phenomena in Clays.* [ed.] A T Skjeltorp and S F Edwards. s.l. : Kluwer Academic Publishers, 2000. pp. 269-279.

[2]. *Observation of Nematic Liquid-Crystal Textures in Aqueous Gels of Smectite Clays.* **Gabriel, J C, Sanchez, C and Davidson, P.** 1996, J. Phys. Chem., Vol. 100, p. 11139.

[3]. *Phase-diagram of colloidal dispersions of anisotropic charged-particles – equilibrium properties, structure, and rheology of laponite suspensions.* **Mourchid, A, et al.** 6, 1995, Langmuir, Vol. 11, pp. 1942-1950.

[4]. *Small-angle neutron scattering investigations of the structure of thixotropic dispersions of smectite clay colloids.* **Ramsay, J D and Lindner, P.** 1993, J. Chem. Soc., Faraday Trans., Vol. 89, p. 4207.

[5]. *Swelling and Dispersion of Smectite Clay Colloids: Determination of Structure by Neutron Diffraction and Small-angle Neutron Scattering.* **Ramsay, J D, Swanton, S W and Bunce, J.** 1990, J. Chem. Soc. Faraday Trans., Vol. 86, p. 3919.

[6]. *Osmotic Compression and Expansion of Highly Ordered Clay Dispersions.* **Martin, C, et al.** 2006, Langmuir, Vol. 22, p. 4065.

[7]. *Orientational order in gravity dispersed clay colloids: A synchrotron x-ray scattering study of Na fluorohectorite suspensions.* **DiMasi, E, et al.** 6, 2001, Phys. Rev. E, Vol. 6406.

[8]. *Observations of orientational ordering in aqueous suspensions of a nano-layered silicate.* **Fossum, J O, et al.** 6, 2004, Energy, Vol. 30, pp. 873-883.

[9]. *The measurement by SAXS of the nematic order parameter of laponite gels.* **Lemaire, B J, et al.** 2002, Europhys. Lett., Vol. 59, p. 55.

[10]. *A Small-Angle X-ray Scattering Study of the Structure of Aqueous Laponite Dispersions.* **Saunders, J M, et al.** 1999, J. Phys. Chem. B, Vol. 103, p. 9211.

[11]. *^23Na Nuclear Magnetic Resonance and ^1H Pulsed Gradient Spin-Echo Detection of the Critical Concentration Corresponding to the Isotrope/Nematic Transition within Aqueous Dispersions of Charged Anisotropic Nanoparticles.* **Porion, P, et al.** 2004, J. Phys. Chem. B, Vol. 108, p. 10825.

[12]. *Analysis of the Degree of Nematic Ordering within Dense Aqueous Dispersions of Charged Anisotropic Colloids by ^23Na NMR Spectroscopy.* **Porion, P, Faugre, A M and Delville, A.** 2005, J. Phys. Chem. B, Vol. 109, p. 20145.

[13]. *Water Self-Diffusion within Nematic Dispersions of Nanocomposites: A Multiscale Analysis of ^1H Pulsed Gradient Spin-Echo NMR Measurements.* **Porion, P, et al.** 2003, J. Phys. Chem. B, Vol. 107, p. 4012.

[14]. *Nematic Ordering of Suspensions of Charged Anisotropic Colloids Detected by ^{23}Na Nuclear Magnetic Resonance.* **Porion, P, et al.** 2001, J. Phys. Chem. B, Vol. 105, p. 10505.

[15]. *Anisotropy of the Solvent Self-Diffusion Tensor as a Probe of Nematic Ordering within Dispersions of Nanocomposites.* **Porion, P, et al.** 2001, Phys. Rev. Lett., Vol. 87, p. 208302.

[16]. *Anisotropic water diffusion in nematic self-assemblies of clay nanoplatelets suspended in water.* **Azevedo, E N, et al.** 9, 2007, Langmuir, Vol. 23, pp. 5100-5105.

[17]. *Über freiwillige Strukturbildung in Solen. (Eine neue Art anisotrop flussiger Medien.).* **Zocher, H.** 1925, Z. Anorg. Allg. Chem, Vol. 147, p. 91.

[18]. *Liquid Crystalline Substances from Virus-infected Plants.* **Bawden, F C, et al.** 1936, Nature, Vol. 138, p. 1051.

[19]. *X-ray and crystallographic studies of plant virus preparations.* **Bernal, J D and Fankuchen, I.** 1941, J. Gen. Physiol., Vol. 25, p. 111.

[20]. *Isotropic-nematic phase transition of nonaqueous suspensions of natural clay rods.* **Zhang, Z. X. and Duijneveldt, J. S.** 2006, J. Chem. Phys., Vol. 124, p. 154910.

[21]. *The effects of shape on the interaction of colloidal particles.* **Onsager, L.** 1949, Ann. N. Y. Acad. Sci., Vol. 51, p. 627.

[22]. *Monte Carlo study of the isotropic and nematic phases of infinitely thin hard platelets.* **Eppenga, R and Frenkel, D.** 1984, Mol. Phys., Vol. 52, p. 1303.

[23]. *Phase behavior of disklike hard-core mesogens.* **Veerman, J A and Frenkel, D.** 1992, Phys. Rev. A, Vol. 45, p. 5632.

[24]. *The Role of Attractive and Repulsive Forces in the Formation of Tactoids, Thixotropic Gels, Protein Crystals and Coacervates.* **Langmuir, I.** 1938, J. Chem. Phys, Vol. 6, p. 873.

[25]. *Sol/Gel and Isotropic/Nematic Transitions in Aqueous Suspensions of Natural Nontronite Clay. Influence of Particle Anisotropy. 1. Features of the I/N Transition.* **Michot, L. J., et al.** 7, 2008, Vol. 24, pp. 3127-3139.

[26]. *Liquid-crystalline aqueous clay suspensions.* **Michot, L J, et al.** 2006, PNAS, Vol. 103, p. 16101.

[27]. *Formation of Nematic Liquid Crystals in Suspensions of Hard Colloidal Platelets.* **Kooij, F M and Lekkerkerker, H N.** 1998, J. Phys. Chem. B, Vol. 102, p. 7829.

[28]. *Nematic ordering vs. gelation in suspensions of charged platelets.* **Beek, D van and Lekkerkerker, H N.** 2003, Europhys. Lett., Vol. 61, p. 702.

[29]. *Isotropic-nematic interface and wetting in suspensions of colloidar platelets.* **van der Beek, D., et al.** 8, 2006, Phys Rev Lett, Vol. 97.

[30]. *Bulk and interfacial properties of binary hard-platelet fluids.* **Bier, M., Harnau, L. and S, Dietrich.** 2, 2004, Phys rev E, Vol. 69.

[31]. *Fluids of platelike particles near a hard wall.* **Harnau, L and Dietrich, S.** 2002, Physical Eeview E, Vol. 65.

[32]. **Brigatti, M F, Galan, E and Theng, B K.** *Structures and mineralogy of clay minerals.* [ed.] F Bergaya, B K Theng and G Lagaly. s.l. : Elsevier, 2006.

[33]. *Birefringent Patterns in the Nemtaic Phase of Na-Fluorhectorite Synthetic Clay.* **Ringdal, N. and J.O., Fossum.** (unpublished).

[34]. *Using synchrotron X-ray scattering to study the diffusion of water in a weakly-hydrated clay sample.* **Méheust, Y, et al.** 2006, Clay Science, Vol. 74, pp. 66-70.

[35]. *Dielectric properties of smectite clays.* **Kaviratna, P D, Pinnavaia, T J and Schroeder, P A.** 12, 1996, J. Phys. Chem. Solids, Vol. 57, pp. 1897-1906.

[36]. *Intercalation-enhanced electric polarization and chain formation of nano-layered particles.* **Fossum, J O, et al.** 2006, Europhys. Lett., Vol. 74, p. 438.

[37]. *Inferring orientation distributions in anisotropic powders of nano-layered crystallites from a single two-dimensional WAXS image.* **Méheust, Y, Knudsen, K D and Fossum, J O.** 2006, J. Appl. Crystallography, Vol. 39, pp. 661-670.

[38]. *Spin diffusion measurements - Spin echoes in presence of a time-dependent field gradient.* **Stejskal, E. O and Tanner, J.E.** 1, 1965, Journal of Chemical Physics, Vol. 42, p. 288.

Appendix C

Additional WAXS data

In this appendix we present the analyzed data from an experimental session at ESRF in 2004. The experiment was performed by Daví Fonsêca, Kenneth Knudsen, Jon Otto Fossum and Yves Méheust. Mainly due to limited time, the data were not treated sufficiently thorough to be included as an integral part of this thesis. The results are nevertheless included as an appendix for two reasons: First, it is a study of the same kind of sample as the one studied in Part II, and it was analyzed by the current author using the model presented there. As such the results are directly comparable to the results in Part II, and requires little extra introduction. Second, and perhaps even more important, the analysis shows some promising results. The data have been left untreated for four years, and this is a nice opportunity to make sure they will not go untreated for four more. By presenting the preliminary results here in a structured way, they will serve as a reference for whoever will continue the analysis, that being either the current author in the event of a PhD, or others.

Finally, note that for all the figures presented in this chapter, ▲ means the anti-nematic distribution has been used to fit the data, ▼ means nematic. The uncertainty is shown only where it is larger than the symbol.

C.1 First experiment – Capillaries

This experiment is more or less similar to the experiment presented in Part II. Two 2 mm capillaries filled with 3 w/w % NaFh and 1×10^{-3} M NaCl are scanned vertically in steps of one millimeter. The difference between the capillaries is that one has settled for 30 days only in the gravitational field (Figures C.1 and C.2), while the other was left to settle in a centrifuge for two days (Figures C.3 and C.4).

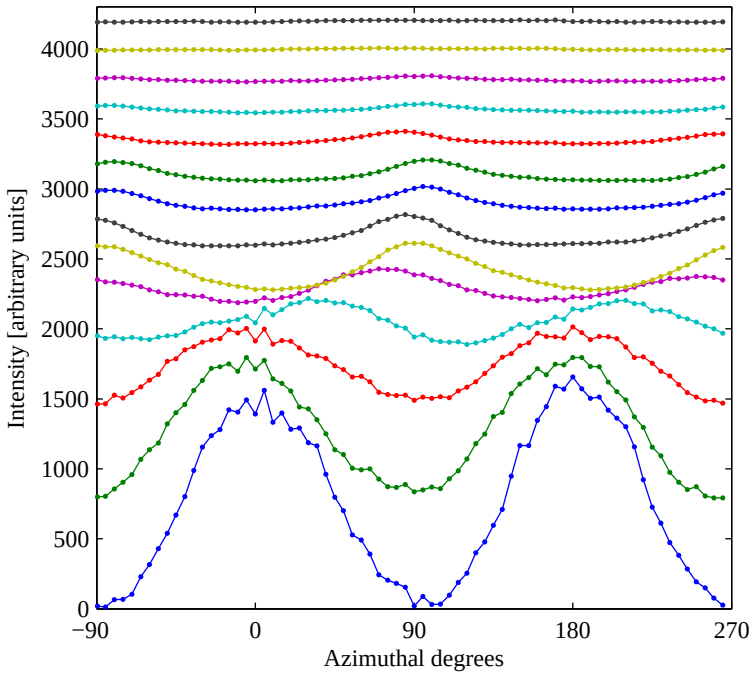

FIGURE C.1: Gravity-settled capillary. Azimuthal profiles for the (001) ring translated vertically according to the height they were recorded at. The distance between each profile is 1 mm, and the lowermost profile was recorded 2 mm from the bottom of the capillary.

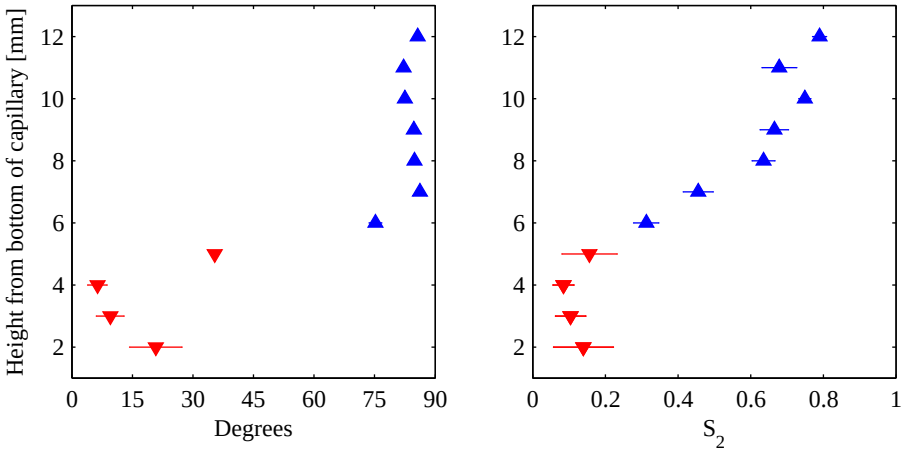

FIGURE C.2: Gravity-settled capillary. **a)** Mean orientation of the particle director, in degrees from vertical. **b)** The calculated nematic order parameter.

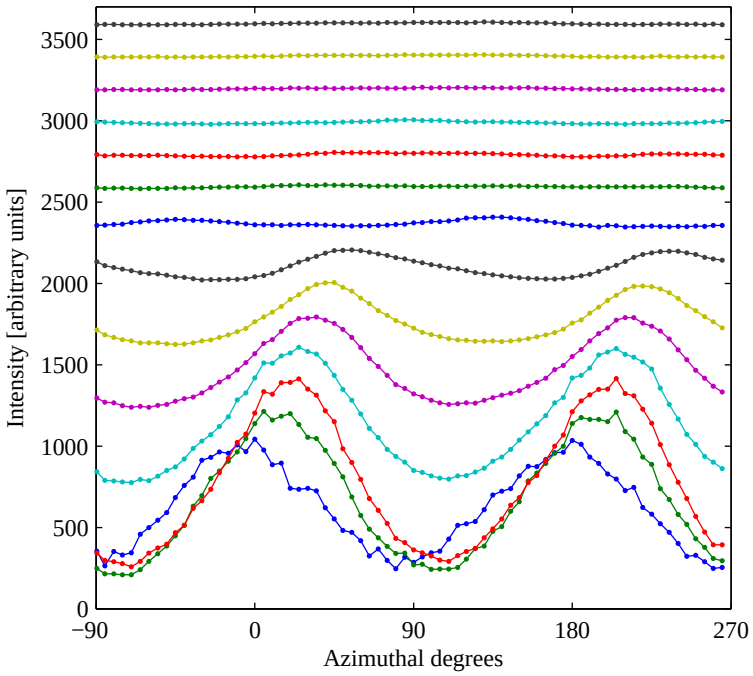

FIGURE C.3: Centrifuge-settled capillary. Azimuthal profiles for the (001) ring translated vertically according to the height they were recorded at. The distance between each profile is 1 mm, and the lowermost profile was recorded 1 mm from the bottom of the capillary.

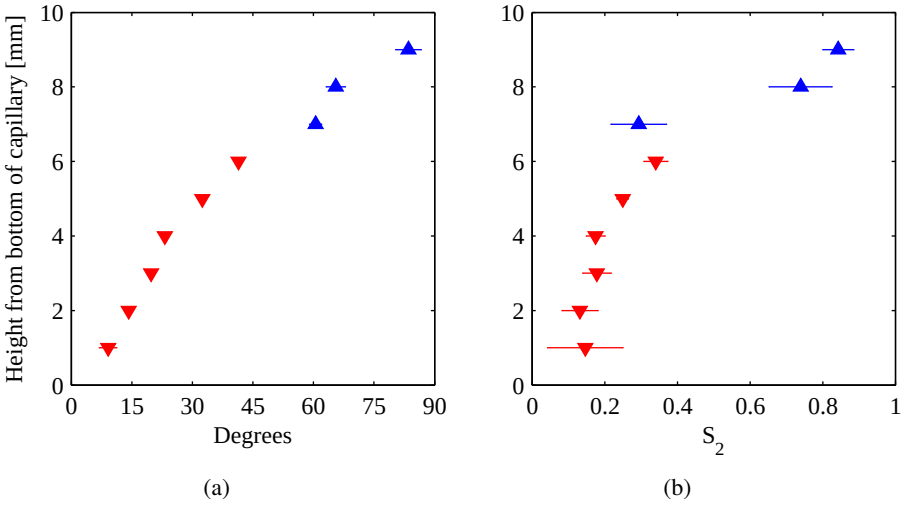

FIGURE C.4: Centrifuge-settled capillary. **a)** Mean orientation of the particle director, in degrees from vertical. **b)** The calculated nematic order parameter.

C.1.1 Short discussion

From Figures C.1 to C.4 we notice a clear difference between the two capillaries. The gravity-settled sample more or less confirms the results already presented in Part II: There is a phase separation between the sediment and a nematic phase, the particle geometry in the nematic phase is anti-nematic, and the order parameter is approximately two thirds. In the centrifuge-settled sample the phase transition is not so abrupt, but rather a continuous transition from horizontal to vertical alignment of the platelets. A jump is observed on the other hand, in the value of the order parameter. With respect to the gravity settled sample, the transition occurs both higher in the capillary and to a higher value of S_2, approximately 0.8.

We do not at the moment have a complete explanation for the phenomenon observed above, but we believe that the centrifuge sample corresponds to the gravity-sample at an earlier time in the sedimentation process. If the NaFh particles had had more time to sediment and separate, the situation in Figure C.2 would have been reached for the centrifuged sample as well.

Notice also that the way our scripts scale the azimuthal profiles could give the wrong impression that the sediment is very anisotropic. It is not the amplitude of the peaks in the azimuthal profile that determines the order, but rather the width of the peaks. As is obvious from both Figure C.2(b) and C.4(b), the sediment is indeed not nematic, but only weakly ordered. We should also note that above the nematic phase the WAXS images indicate isotropic ordering in both cases.

The attentive reader will have noticed that the transition layer with horizontally aligned particles between the sediment and the nematic phase – discussed in Part II and Appendix B – is not observed in either of these samples. As already mentioned in Chapter 7.3, the formation of this layer is not yet fully understood, but is believed to be dependent on factors such as the NaFh grain size, the geometry of the sample holder, the amount of salt used, etc. A more thorough discussion can be found in Ringdal [28], Ringdal et al. [96] and Hemmen et al. [97].

A continuation of this work should perhaps focus on varying the parameters of the centrifuging. The results presented here show that centrifuging can alter the sedimentation process, and by varying the speed one could imagine the sedimentation to be both slowed down and accelerated. Combining SAXS data already obtained using Complex' own in-house X-ray equipment with these and future synchrotron data could give fascinating results.

C.2 Second experiment – Rectangular samples

Additional vertical scans are performed, but this time in sample holders that are rectangular. Again the sample used is 3 w/w % NaFh and 1×10^{-3} M NaCl. The sample holder itself is made of a black plastic called POM (Polyoxymethylene from Goodfellow Ltd.) that contrary to glass is apolar. The sample holder was constructed to allow mounting of exhangable walls perpendicular to the beam, so that we have lateral walls made of POM, and perpendicular walls of another material. The dimensions are 5 mm lateral, 62 mm vertical, and 2 mm depth (pathlength), and an image of the sample holder is shown in Figure C.5.

FIGURE C.5: The rectangular sample holder.

We performed vertical scans on three samples, each with different perpendicular walls. The first sample had walls made of the material Kapton (Kapton HN from Goodfellow Ltd.), and the results are shown in Figures C.6 and C.7. Kapton, like POM, is apolar. Hence, in this sample we should expect substantially less homeotropic alignment. With apolar walls, the NaFh particles experience only the steric effect of a hard wall [95], not the strong electromagnetic coupling with a hydrogen-bond-forming hydrophilic glass [94]. The other two samples had walls made of glass, namely Deckgläser D 263 M #0 from Menzel-Gläser (*type 0*) and Deckgläser D 263 M #1 from Knittel Gläser (*type 1*).

The reason for using two different coverglasses was to test which was best suited for further experiments using this setup, the difference between the glasses being thickness and chemical composition. For the purpose of the results presented here – Figures C.8 and C.9 for type 0 and Figures C.10 and C.11 for type 1 – the glasses are equal and will be treated as such.

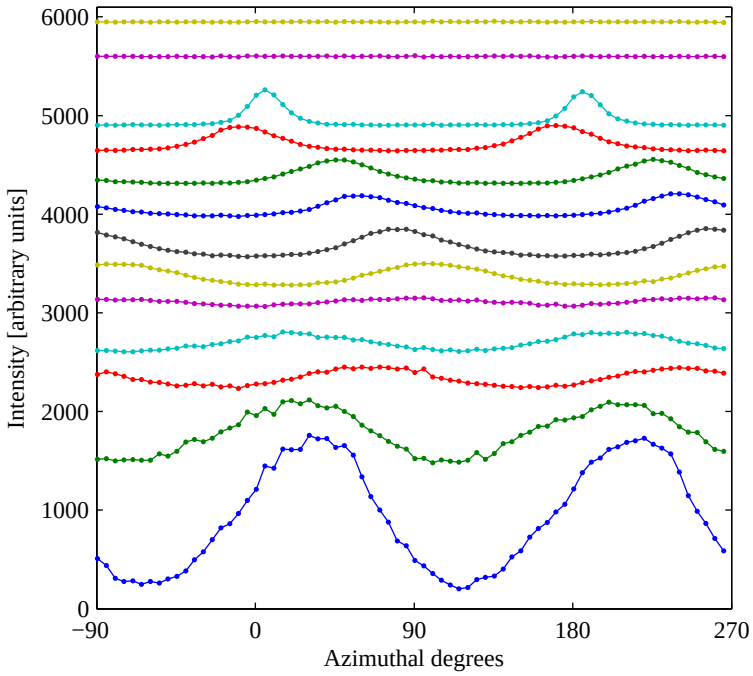

FIGURE C.6: Kapton-walled rectangular sample. Azimuthal profiles for the (001) ring translated vertically according to the height they were recorded at. The distance between each profile is 1 mm, and the lowermost profile was recorded 1 mm from the bottom of the sample.

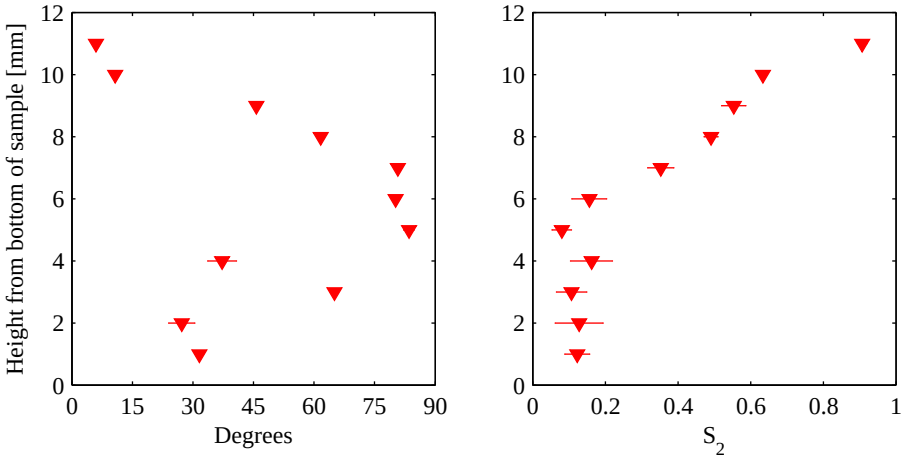

FIGURE C.7: Kapton-walled rectangular sample. **a)** Mean orientation of the particle director, in degrees from vertical. **b)** The calculated nematic order parameter.

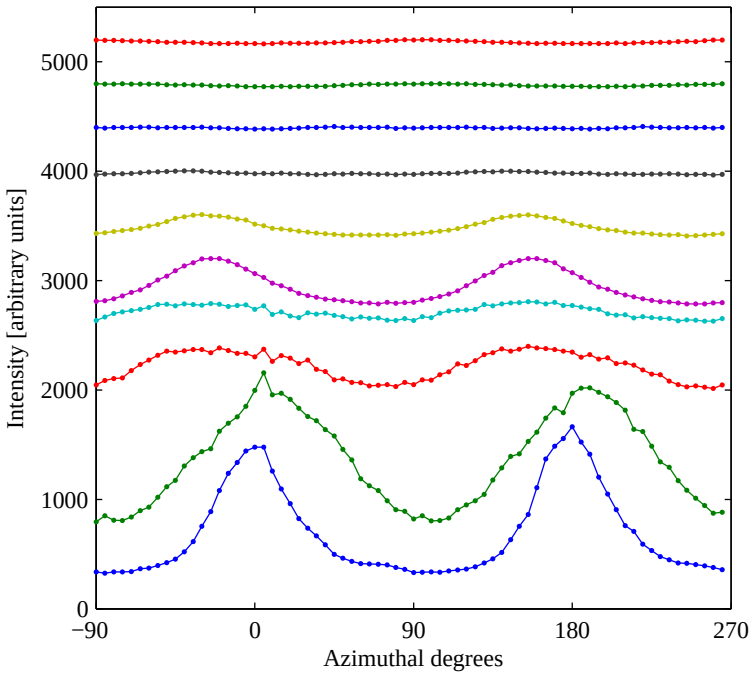

FIGURE C.8: Type 0 glass-walled rectangular sample. Azimuthal profiles for the (001) ring translated vertically according to the height they were recorded at. The distance between each profile is 1 mm, and the lowermost profile was recorded 1 mm from the bottom of the sample.

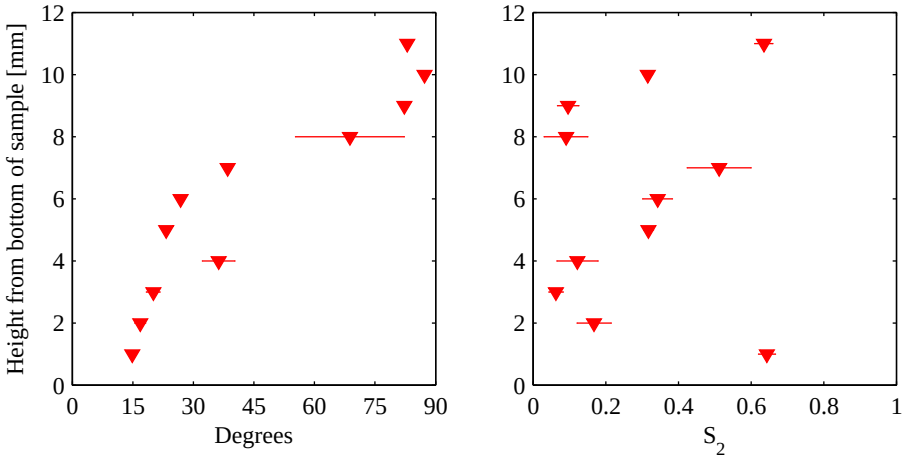

FIGURE C.9: Type 0 glass-walled rectangular sample. **a)** Mean orientation of the particle director, in degrees from vertical. **b)** The calculated nematic order parameter.

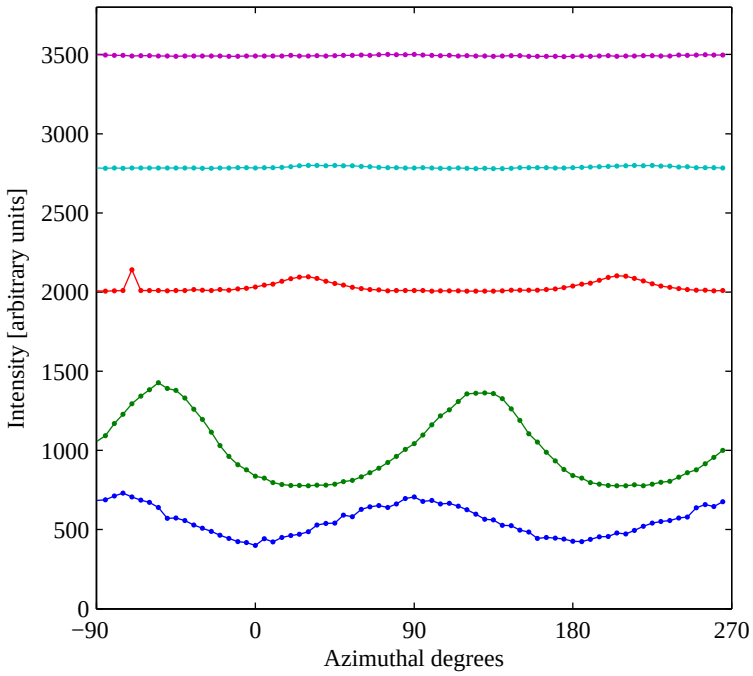

FIGURE C.10: Type 1 glass-walled rectangular sample. Azimuthal profiles for the (001) ring translated vertically according to the height they were recorded at. The distance between each profile is 2.5 mm, and the lowermost profile was recorded 2.5 mm from the bottom of the sample.

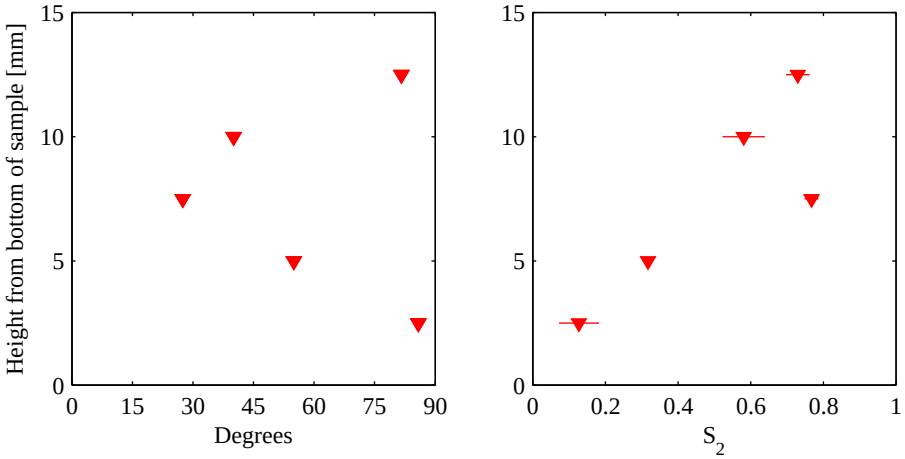

FIGURE C.11: Type 1 glass-walled sample. **a)** Mean orientation of the particle director, in degrees from vertical. **b)** The calculated nematic order parameter.

C.2.1 Short discussion

Kapton-walled sample

The most interesting result of the ones presented above is the orientation and order in the Kapton-walled sample. As was the case for the capillaries, a phase with nematic ordering is formed above the sediment, but in this sample neither the order nor the orientation is constant throughout the phase. We instead observe an almost linear transition from horizontally to vertically aligned particles as we move from the bottom to the top of the nematic phase. At the same time, a linear increase from almost no ordering in the sediment to a nearly completely ordered state at the top of the nematic phase is found.

Further experiments are required before a complete explanation can be found, but a handwaving argument readily presents itself. With polar sample walls and in a certain concentration of particles and particle-sizes, we already know from MRI experiments [94] that the NaFh platelets firmly anchor themselves face to wall in a region close to the walls. This strong ordering completely dominates any other self organizing of the particles, and can be thought of to propagate from the walls into the interiors of the sample. Hence, in what we have called the anti-nematic phase in glass capillaries, both the order and orientation of the particles are more or less constant and determined by the polar wall effects.

In the Kapton-walled sample studied here though, we can assume the effect on the NaFh platelets from the walls to be significantly reduced. This is again confirmed by MRI in the case of apolar Teflon walls [94]. It could therefore be that the NaFh platelets, free from the power of face-to-wall ordering, and left to order themselves, prefer this kind of vertical to horizontal ordering instead of the anti-nematic phase. We have actually previously observed the same kind of phenomenon in glass capillaries where some of the water has been allowed to evaporate [98], as well as equivalent Fr'eedericksz transitions [99] appearing when magnetic fields are applied to the samples [28].

Future studies on this phenomenon should first focus on observing the same effect again, thus proving reproducibility. Furthermore, the role of NaFh concentration, salt concentration, and sample geometry (e.g. using Kapton capillaries) are parameters that can easily be varied. To combine this with SAXS data on the evaporation [98] and attempt a theoretical explanation should also be prioritized.

Glass-walled samples

The results from the glass-walled samples might at first glance seem difficult to interpret. The first thing to notice is that while the area studied is more or less the same, the type 0 sample is scanned in steps of 1 mm, and the type 1 in steps of

2.5 mm. With this in mind, it seems that the results in Figures C.9 and C.11 do not agree with the other vertical scans we have looked at. From the order parameter in the type 0 sample (Figure C.9(b)), it is particularly difficult to identify any clear phase transition between sediment and nematic.

To understand this, we need to consider both the sample- and scattering geometry. As the reader might have already noticed, we have used only the nematic distribution to fit the data in this section. This is based on geometrical considerations. In circular or rectangular glass capillaries, the homeotropic face-to-wall bonding makes the particles stand up, but it also distributes the particle director in the horizontal plane. This is what we have denoted anti-nematicity [33], and what others have called biaxial nematicity [94]. With homeotropic bonding only to the perpendicular glass walls, we expect a nematic [33] (or uniaxial nematic [94]) phase to form where we normally observe the anti-nematic phase. The fact that the data-fits in most cases are good, i.e. small uncertainties when varying the fitting window, is a partial confirmation of this assumption. Regarding the Kapton walled-case, it is not the perpendicular glass walls that causes nematicity, but rather the absence of polar walls whatsoever.

To continue the explanation, recall from the theory section on X-ray diffraction the scattering condition: $2d \sin\theta = n\lambda$. In order for the NaFh platelets to contribute to the scattered intensity, they must make an angle θ with the incoming beam that fulfills Braggs's law for a given d. Inserting the mean d-spacing of NaFh with two intercalated water layers: $d_{mean} = 15.1$ Å [12], and the X-ray wavelength used in this experiment: $\lambda = 0.71$ Å, the resulting scattering angle is $\theta = 1.35°$. Assuming the mean particle orientation to be face-to-wall, i.e. $\theta = 90°$ only the very few platelets that are almost perpendicular to the mean preferred orientation will contribute to the scattering. Hence, we can have a very ordered nematic phase, without really being able to observe it with WAXS.

To support this assumption, we have included in Figure C.12 the central diffractogram areas of a selection of heights in the type 0 glass-walled sample. Notice the dramatic change from $h = 6$ mm (sediment) to $h = 7$ mm (nematic phase). The rather intense small angle scattering visible outside the beamstop actually increases, while the (001) ring shows a marked intensity drop. We take this as a confirmation of our particle orientation assumptions above. For heights above 13 mm, neither (001) ring nor small angle scattering is visible, which is consistent with the Kapton-walled sample. The poorly adjusted beamstop revealed by the diffractograms has been corrected for by subtracting a background scan before analysis.

In order to study this phenomenon further, a different sample holder must be used. As the X-ray absorption in POM is rather low, a sample holder with thinner lateral walls could cast more light on the particle orientation. With this kind of sample holder we could rotate the sample and image the platelets from the side

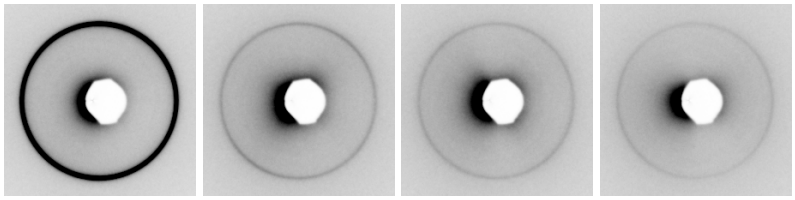

(a) $h = 6\,\text{mm}$ (b) $h = 7\,\text{mm}$ (c) $h = 8\,\text{mm}$ (d) $h = 9\,\text{mm}$

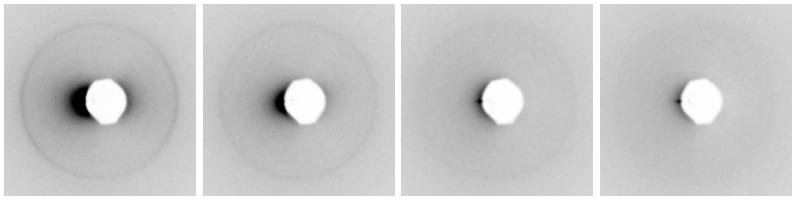

(e) $h = 10\,\text{mm}$ (f) $h = 11\,\text{mm}$ (g) $h = 12\,\text{mm}$ (h) $h = 13\,\text{mm}$

FIGURE C.12: Diffractograms for the type 0 glass-walled sample.

as well as face on, i.e. incoming X-ray beam parallel to the NaFh platelets. By recording the scattered intensity at different sample rotations we should be more suited to make conclusions about the particle orientations.

List of Figures

References

[1] S. Staubach. *Clay. The history and evolution of humankind's relationship with earth's most primal element.* Penguin Books, 2005.

[2] B. Velde. *Introduction to clay minerals*. Chapman & Hall, 1992.

[3] A. Meunier. *Clays*. Springer, electronic edition, 2005.

[4] F. Bergaya and G. Lagaly. General introduction: Clays, clay minerals and clay science. In F. Bergaya, B. K. G. Theng, and G. Lagaly, editors, *Handbook of Clay Science*. Elsevier, 2006.

[5] J. O. Fossum. Complex physical phenomena in clays. In A. T. Skjeltorp and S. F. Edwards, editors, *Soft Condensed Matter: Configurations, Dynamics and Functionality*, pages 269–279. Kluwer Academic Publishers, 2000.

[6] S. Guggenheim and R. T. Martin. Definition of clay and clay mineral; joint report of the AIPEA nomenclature and CMS nomenclature committees. *Clay Minerals*, 30(3):257–259, 1995.

[7] D. W. Bruce and D. O'Hare, editors. *Inorganic Materials*. Wiley, 1992.

[8] P. Boulet, H. C. Greenwell, S. Stackhouse, and P. V. Coveney. Recent advances in understanding the structure and reactivity of clays using electronic structure calculations. *J. Mol. Structure-theochem*, 762(1-3):33–48, 2006.

[9] S. A. Solin. Clays and clay intercalation compounds: Properties and physical phenomena. *Ann. Rev. Materials Science*, 27:89–115, 1997.

[10] M. F. Brigatti, E. Galan, and B. K .G. Theng. Structures and mineralogy of clay minerals. In F. Bergaya, B.K.G. Theng, and G. Lagaly, editors, *Handbook of Clay Science*. Elsevier, 2006.

[11] P. Komadel, J. Madejova, and J. Bujdak. Preparation and properties of reduced-charge smectites – A review. *Clays And Clay Minerals*, 53:313–334, 2005.

[12] G. J. da Silva, J. O. Fossum, E. DiMasi, K. J. Måløy, and S. B. Lutnæs. Synchrotron X-ray scattering studies of water intercalation in a layered synthetic silicate. *Phys. Rev. E*, 66(1), 2002.

[13] G. J. da Silva, J. O. Fossum, E. DiMasi, and K. J. Måløy. Hydration transitions in a nanolayered synthetic silicate: A synchrotron X-ray scattering study. *Phys. Rev. B*, 67(9), 2003.

[14] K. D. Knudsen, J. O. Fossum, G. Helgesen, and V. Bergaplass. Pore characteristics and water absorption in a synthetic smectite clay. *J. Appl. Crystallography*, 36:587–591, 2003.

[15] J. O. Fossum. Physical phenomena in clays. *Physica A*, 270(1-2):270–277, 1999.

[16] P. C. Hiemenz and R. Rajagopalan. *Principles of Colloid and Surface Chemistry*. CRC Press, third edition, 1997.

[17] A. Mourchid, E. Lecolier, H. Van Damme, and P. Levitz. On viscoelastic, birefringent, and swelling properties of Laponite clay suspensions: Revisited phase diagram. *Langmuir*, 14(17):4718–4723, 1998.

[18] P. D. Kaviratna, T. J. Pinnavaia, and P. A. Schroeder. Dielectric properties of smectite clays. *J. Phys. Chem. Solids*, 57(12):1897–1906, 1996.

[19] Rockwood Additives Ltd. Laponite – Performance additives. `http://www.scprod.com/pdfs/LaponiteBrochureE.pdf` (2007-10-04).

[20] A. Mourchid, A. Delville, J. Lambard, E. Lecolier, and P. Levitz. Phase-diagram of colloidal dispersions of anisotropic charged-particles – equilibrium properties, structure, and rheology of Laponite suspensions. *Langmuir*, 11(6):1942–1950, 1995.

[21] E. Balnois, S. Durand-Vidal, and P. Levitz. Probing the morphology of Laponite clay colloids by atomic force microscopy. *Langmuir*, 19(17):6633–6637, 2003.

[22] N. Willenbacher. Unusual thixotropic properties of aqueous dispersions of Laponite RD. *J. Colloid Interface Science*, 182(2):501–510, 1996.

[23] M. Dijkstra, J. P. Hansen, and P. A. Madden. Statistical model for the structure and gelation of smectite clay suspensions. *Phys. Rev. E*, 55(3):3044–3053, 1997.

[24] L. J. Michot, I. Bihannic, S. Maddi, S. S. Funari, C. Baravian, P. Levitz, and P. Davidson. Liquid-crystalline aqueous clay suspensions. *Proc. National Acad. Sciences United States Am.*, 103(44):16101–16104, 2006.

[25] J. N. Israelachvili. *Intermolecular & Surface Forces*. Academic Press, second edition, 1991.

[26] A. Bakk, J. O. Fossum, G. J. da Silva, H. M. Adland, A. Mikkelsen, and A. Elgsaeter. Viscosity and transient electric birefringence study of clay colloidal aggregation. *Phys. Rev. E*, 65(2), 2002.

[27] J. O. Fossum, E. Gudding, D. d. M. Fonseca, Y. Méheust, E. DiMasi, T. Gog, and C. Venkataraman. Observations of orientational ordering in aqueous suspensions of a nano-layered silicate. *Energy*, 30(6):873–883, 2004.

[28] N. I. Ringdal. Experimental studies of self-organized liquid crystalline phases from clay nanoplatelets in water: Birefringence and structure. Master's thesis, Norwegian University of Science and Technology, 2008.

[29] G. Strobl. *Condensed Matter Physics – Crystals, liquids, liquid crystals and polymers*. Springer Verlag, 2004.

[30] E. DiMasi, J. O. Fossum, T. Gog, and C. Venkataraman. Orientational order in gravity dispersed clay colloids: A synchrotron X-ray scattering study of Na-fluorohectorite suspensions. *Phys. Rev. E*, 6406(6), 2001.

[31] G. Lovoll, B. Sandnes, Y. Méheust, K. J. Måløy, J. O. Fossum, G. J. Da silva, M. S. P. Mundim, R. Droppa, and D. M. Fonseca. Dynamics of water intercalation fronts in a nano-layered synthetic silicate: A synchrotron X-ray scattering study. *Physica B*, 370:90–98, 2005.

[32] J. O. Fossum, Y. Méheust, K. P. S. Parmar, K. D. Knudsen, K. J. Måløy, and D. M. Fonseca. Intercalation-enhanced electric polarization and chain formation of nano-layered particles. *Europhysics Lett.*, 74(3):438–444, 2006.

[33] Y. Méheust, K. D. Knudsen, and J. O. Fossum. Inferring orientation distributions in anisotropic powders of nano-layered crystallites from a single two-dimensional WAXS image. *J. Appl. Crystallography*, 39:661–670, 2006.

[34] D. M. Fonseca, Y. Méheust, J. O. Fossum, K. D. Knudsen, K. J. Måløy, and K. P. S. Parmar. Phase behavior of platelet-shaped nanosilicate colloids in saline solutions – a small-angle X-ray scattering study. *J. Appl. Crystallography*, 40:S292–S296, 2007.

[35] E. D. Becker, C. L. Fisk, and C. L. Khetrapal. The development of NMR. In D. M. Grant and R. K. Harris, editors, *Encyclopedia of Nuclear Magnetic Resonance*, volume 1. John Wiley & Sons Ltd., 1996.

[36] I. I. Rabi, J. R. Zacharias, S. Millman, and P. Kusch. A new method of measuring nuclear magnetic moment. *Phys. Rev.*, 53(4):318, Feb 1938. doi: 10.1103/PhysRev.53.318.

[37] E. M. Purcell, H. C. Torrey, and R. V. Pound. Resonance absorption by nuclear magnetic moments in a solid. *Phys. Rev.*, 69(1-2):37–38, Jan 1946. doi: 10.1103/PhysRev.69.37.

[38] C. P. Slichter. *Principles of Magnetic Resonance*. Springer-Verlag, second edition, 1980.

[39] Z. P. Liang and P. C. Lauterbur. *Principles of Magnetic Resonance Imaging. A Signal Processing Perspective*. IEEE Press, 2000.

[40] P. C. Hemmer. *Kvantemekanikk*. Tapir akademisk forlag, 2005.

[41] E. M. Haacke, R. W. Brown, M. R. Thompson, and R. Venkatesan. *Magnetic Resonance Imaging. Physical Principles and Sequence Design.* John Wiley & Sons, 1999.

[42] H. Günther. *NMR Spectroscopy. Basic principles, concepts, and applications in chemistry*. John Wiley & Sons Ltd, second edition, 1995.

[43] E. L. Hahn. Spin echoes. *Phys. Rev.*, 80:580–594, 1950.

[44] P. C. Lauterbur. Image formation by induced local interactions – examples employing nuclear magnetic-resonance. *Nature*, 242(5394):190–191, 1973.

[45] P. C. Lauterbur. One path out of many – how MRI actually began. In D. M. Grant and R. K. Harris, editors, *Encyclopedia of Nuclear Magnetic Resonance*, volume 1. John Wiley & Sons Ltd., 1996.

[46] P. Mansfield and A. A. Maudsley. Medical imaging by NMR. *British J. Radiology*, 50(591):188–194, 1977.

[47] R. B. Northrop. *Introduction to instrumentation and measurements*. Taylor & Francis, 2005.

[48] P. Meakin. The growth of rough surfaces and interfaces. *Phys. Reports-review Section Phys. Lett.*, 235(4-5):189–289, 1993.

[49] E. Bouchaud. Scaling properties of cracks. *J. Phys.: Condens. Matter*, 9: 4319–4344, 1997.

[50] D. Broek. *Elemtary engineering fracture mechanics*. Martinus Nijhoff, third revised edition, 1982.

[51] A. T. Zehnder. Lecture notes on fracture mechanics. `http://dspace.library.cornell.edu/handle/1813/3075` (2008-01-23), 2007.

[52] B. B. Mandelbrot, D. E. Passoja, and A. J. Paullay. Fractal character of fracture surfaces of metals. *Nature*, 308(5961):721–722, 1984.

[53] B. B. Mandelbrot. *The fractal geometry of nature*. W. H. Freeman and company, updated and augmented edition, 1982.

[54] K. J. Måløy, A. Hansen, E. L. Hinrichsen, and S. Roux. Experimental measurements of the roughness of brittle cracks. *Phys. Rev. Lett.*, 68:213–215, 1992.

[55] R. Voss. Fractals in nature. In Heinz-Otto Peitgen and Dietmar Saupe, editors, *The science of fractal images*, pages 21–69. Springer, 1988.

[56] J. Schmittbuhl, J. P. Vilotte, and S. Roux. Reliability of self-affine measurements. *Phys. Rev. E*, 51(1), 1995.

[57] J. Ø. H. Bakke and A. Hansen. Accuracy of roughness exponent measurement methods. *Phys. Rev. E*, 76(1), 2007.

[58] J. Feder. *Fractals*. Plenum press, 1988.

[59] L. Ponson, D. Bonamy, H. Auradou, G. Mourot, S. Morel, E. Bouchaud, C. Guillot, and J. P. Hulin. Anisotropic self-affine properties of experimental fracture surfaces. *Int. J. Fracture*, 140(1-4):27–37, 2006.

[60] L. Ponson, D. Bonamy, and E. Bouchaud. Method and system to determine the path followed by at least one crack from one or several fracture surfaces created by the said crack(s). American patent application No. 11/311, 280, 2005.

[61] A. Livne, G. Cohen, and J. Fineberg. Universality and hysteretic dynamics in rapid fracture. *Phys. Rev. Lett.*, 94(22), 2005.

[62] Y. Tanaka, K. Fukao, Y. Miyamoto, H. Nakazawa, and K. Sekimoto. Regular patterns on fracture surfaces of polymer gels. *J. Phys. Soc. Japan*, 65(8): 2349–2352, 1996.

[63] K. R. Shull. Fracture and adhesion of elastomers and gels: Large strains at small length scales. *J. Polymer Science Part B-polymer Phys.*, 44(24):3436–3439, 2006.

[64] T. van Vliet and P. Walstra. Large deformation and fracture behaviour of gels. *Faraday Discussions*, pages 359–370, 1995.

[65] E. N. de Azevedo. Difusão anômala em meios porosos. Master's thesis, Universidade Federal de Pernambuco, 2005.

[66] C. A. Nielsen. An experimental study of fractures in gels. Master's thesis, Norwegian University of Science and Technology, 2007.

[67] Y. Tanaka, K. Fukao, and Y. Miyamoto. Fracture energy of gels. *European Phys. J. E*, 3(4):395–401, 2000.

[68] K. Magnus. Experimental research on fractures in gels. Master's thesis, Norwegian Universtiy of Science and Technology, 2008. In preparation.

[69] W. H. Press, S. A. Teukolsky, W. T. Vetterling, and B. P. Flannery. *Numerical Recipes in Fortran 77*. Cambridge University Press, second edition, 1997.

[70] A. Delaplace, J. Schmittbuhl, and K. J. Måløy. High resolution description of a crack front in a heterogeneous Plexiglas block. *Phys. Rev. E*, 60(2): 1337–1343, 1999.

[71] Electronic correspondence with Professor Jean Schmittbuhl at Ecole et Observatoire des Science de la Terre, Strasbourg, 2008.

[72] K. Magnus. Preparation for experimental research on fractures in gels. Unpublished project report. Norwegian University of Science and Technology, 2007.

[73] C. W. Lung, J. Jiang, E. K. Tian, and C. H. Zhang. Relation between fractal dimension and roughness index for fractal surfaces. *Phys. Rev. E*, 60(5):5121–5125, 1999.

[74] J. F. Goyet. *Physics and Fractal Structures*. Springer-Verlag, 1996.

[75] B. Abou, D. Bonn, and J. Meunier. Nonlinear rheology of Laponite suspensions under an external drive. *J. Rheology*, 47(4):979–988, 2003.

[76] C. Y. Wen and R. Acharya. Self-similar texture characterization using a Fourier-domain maximum likelihood estimation method. *Pattern Recognition Lett.*, 19(8):735–739, 1998.

[77] A. S. Schlachter and F. J. Wuilleumier, editors. *New directions in research with third-generation soft X-ray synchrotron radiation sources.* NATO ASI Series. Kluwer Academic, 1994.

[78] K. Balewski, W. Brefeld, W. Decking, H. Franz, and E. Weckert R. Röhlsberger. PETRA III: A low emittance synchrotron radiation source. Technical report, Deutsches Elektronen-Synchrotron, 2004.

[79] J. R. Heliwell. *Macromolecular crystallography with synchrotron radiation*. Cambridge University Press, 1992.

[80] D. Einfeld. Synchrotron light sources, status and new projects. In Vasili Tsakanov and Helmut Wiedemann, editors, *Brilliant Light in Life and Material Sciences*. Springer, 2007.

[81] J Baruchel, J. L. Hodeau, M. S. Lehmann, J. R. Regnard, and C. Schlenker, editors. *Neutron and synchrotron radiation for condensed matter studies*, volume 1. Springer, 1993.

[82] H. Winick, editor. *Synchrotron radiation sources – A primer*. World Scientific, 1994.

[83] G. H. Stout and L. H. Jensen. *X-ray structure determination – A practical guide*. John Wiley & Sons, second edition, 1989.

[84] J. Als-Nielsen and D. McMorrow. *Elements of modern X-ray physics*. John Wiley & Sons, 2001.

[85] European Synchrotron Radiation Facility. *Highlights 2006*. ESRF, 2007.

[86] D. M. Moore and R. C. Reynolds, Jr. *X-ray diffraction and the identification and analysis of clay minerals*. Oxford University Press, second edition, 1997.

[87] S. Elliot. *The physics and chemistry of solids*. John Wiley & Sons, 1998.

[88] K. Cummings, P. Laws, E. Redish, and P. Cooney. *Understanding physics*. John Wiley & Sons, 2004.

[89] L. R. Alme. Water transport in selected nanopourous media. Master's thesis, Norwegian University of Science and Technology, 2007.

[90] ESRF. The European Synchrotron Radiation Facility homepage. `http://www.esrf.eu` (2008-01-30), 2008.

[91] C. Hendrich. View from Mount Jalla on the ESRF and Institut Laue-Langevin in Grenoble.
`http://commons.wikimedia.org/wiki/Image:Esrf_grenoble.jpg` (2008-01-30), 2004.

[92] A. Hammersley. *FIT2D Reference Manual*. ESRF, 2004.

[93] Y. Méheust, B. Sandnes, G. Lovoll, K. J. Måløy, J. O. Fossum, G. J. da Silva, M. S. P. Mundim, R. Droppa, and D. d. M. Fonseca. Using synchrotron X-ray scattering to study the diffusion of water in a weakly-hydrated clay sample. *Clay Science*, 74:66–70, 2006.

[94] E. N. de Azevedo, M. Engelsberg, J. O. Fossum, and R. E. de Souza. Anisotropic water diffusion in nematic self-assemblies of clay nanoplatelets suspended in water. *Langmuir*, 23(9):5100–5105, 2007.

[95] L. Harnau and S. Dietrich. Fluids of platelike particles near a hard wall. *Phys. Rev. E*, 65(2), 2002.

[96] N. I. Ringdal, J. O. Fossum, D d.M. Fonseca, and A. Gmira. Birefringent patterns in the nematic phase of Na-fluorhectorite synthetic clay. In preparation, 2008.

[97] H. Hemmen, N.I. Ringdal, E. N. De Azevedo, E. L. Hansen, J.O. Fossum, M. Engelsberg, Y. Mehéust, and K. Knudsen. Experimental studies of the isotropic-nematic interface in suspensions of Na-fluorohectorite synthetic clay. In preparation, 2008.

[98] E. L. Hansen. Experimental studies of colloidal dispersions (working title). Master's thesis, Norwegian University of Science and Technology, 2008. In preparation.

[99] P. Oswald and P. Pieranski. *Nematic and Cholesteric Liquid Crystals*. Taylor & Francis, 2005.